Dissertation

submitted to the
Combined Faculties of the Natural Sciences and Mathematics
of the Ruperto–Carola–University of Heidelberg, Germany
for the degree of
Doctor of Natural Sciences

Put forward by
Maik Weber
born in Merzig, Germany
Oral examination: Dec. 19, 2012

Structure Formation in Growing Neutrino Cosmology

Referees: Prof. Dr. Christof Wetterich
Prof. Dr. Luca Amendola

Kosmologische Strukturbildung bei wachsender Neutrinomasse

Das Rätsel der Dunklen Energie könnte in Verbindung stehen mit der Physik der Neutrinomassen. Es wurde vorgeschlagen, dass eine wachsende Neutrinomasse die beschleunigte Expansion des Universums einleitet, indem sie die Entwicklung eines dynamischen Skalarfeldes stoppt. In diesen Szenarien vermittelt das Skalarfeld eine starke anziehende Kraft zwischen Neutrinos, die die Behandlung von Störungsgrößen erheblich erschwert; Standardmethoden wie lineare Störunsrechnung oder Newtonsche N-Teilchen Simulationen sind nicht angemessen. In dieser Arbeit stellen wir eine Simulationsmethode vor, die es erlaubt, die Bildung nichtlinearer Neutrinostrukturen unter Berücksichtigung von relativistischen Teilchengeschwindigkeiten, lokalen Massenvariationen und Rückkopplungseffekten auf den kosmologischen Hintergrund zu behandeln. Wir untersuchen die kosmologische Entwicklung des Modells für exemplarische Parameterwerte bis zur Rotverschiebung $z = 1$ und identifizieren dabei charakteristische Merkmale. Insbesondere beschäftigen wir uns mit der Entstehung und den Eigenschaften kompakter Neutrinostrukturen. In einem allgemeineren Zusammenhang befassen wir uns auch mit "3D Weak Lensing", einer vielversprechenden Methode zur Beobachtung großskaliger Strukturbildung. Ohne ein bestimmtes Modell anzunehmen, entwickeln wir numerische Methoden, die die notwendigen Berechnungen erleichtern. Als Anwendung untersuchen wir eine einfache Parametrisierung inhomogener Dunkler Energie und schätzen die zu erwartenden Einschränkungen durch zukünftige Daten.

Structure Formation in Growing Neutrino Cosmology

The mystery of dark energy may be related to the physics of neutrino mass. It has been proposed that a growing neutrino mass triggers the onset of the accelerated expansion of the Universe by stopping the evolution of a dynamical dark energy scalar field. In these scenarios, the scalar field mediates a strong attractive force between neutrinos, which considerably complicates the treatment of perturbations; standard methods such as linear perturbation theory and Newtonian N–body simulations are not appropriate. In this work, we present a simulation method that allows to incorporate nonlinear neutrino clustering, relativistic velocities, spatial neutrino mass variations, and backreaction effects in growing neutrino cosmologies. For an exemplary parameter set, we study the cosmological evolution until redshift $z = 1$ and identify characteristic signatures of the model. In particular, the formation and properties of nonlinear neutrino structures are investigated. In a more general context, we ask for promising methods to constrain models with enhanced structure formation on large scales and attend to 3D weak lensing. Without adopting a specific model, we present adequate numerical tools for the computation of 3D weak lensing spectra. As an application, we consider a simple parameterization of clustering dark energy and forecast constraints on the properties of dark energy by future data.

Contents

1 Introduction

The Nobel Prize in Physics 2011 was awarded "for the discovery of the accelerating expansion of the Universe through observations of distant supernovae."[1] This groundbreaking discovery (Riess et al., 1998; Perlmutter et al., 1999) confronted cosmologists with a great mystery: What causes the acceleration of the expansion rate? In the framework of Einstein's theory of General Relativity (GR), the dynamics of the cosmic expansion are intimately connected with the properties of matter fields in the Universe. The surprising results from observations of distant supernovae of Type Ia (SN Ia) that were honored by the Nobel Prize are incompatible with a universe essentially made up of ordinary matter and radiation. Rather, they imply that we live in a cosmic epoch in which the energy budget of the Universe is dominated by a so far unknown component with exotic properties. This puzzling new component is called the *dark energy*. It plays a central role in the context of this thesis.

The paradigm of an expanding Universe has become well established over the last century. Soon after the proposal of GR, Friedman (1922) studied the class of homogeneous and isotropic spacetimes and derived the laws governing the uniform expansion of space that are believed to describe our Universe on average. A few years later, Hubble (1929) provided the first observational evidence for an expanding Universe when he discovered that the apparent recessional velocities of distant galaxies increase with distance. During the subsequent decades, a comprehensive picture of our Universe and its history emerged and became broadly accepted due to theoretical, experimental and observational progress. One of the milestones of this development was the discovery of the Cosmic Microwave Background (CMB) by Penzias and Wilson (1965). This relic black–body radiation is one of the key predictions of *Big Bang Cosmology* (e. g. Gamow, 1946; Alpher et al., 1948). Precision measurements of the tiny CMB temperature fluctuations still provide a major source of information on the properties and evolution of the Universe (e. g. Komatsu et al., 2011). They allowed to pin down the geometry of the Universe (e. g. de Bernardis et al., 2000) and thereby revealed the missing energy problem: The contributions from cold dark matter (CDM), baryons, and the (today negligible) radiation component can only explain about a quarter of the required total energy density to explain the inferred shape of the Universe. This strengthens the case for dark energy; or something that imitates its effect.

The issue of dark energy has led to a revival of the cosmological constant Λ. Originally, Einstein proposed it as a modification to his field equations in order to construct a static Universe but he abandoned it again after Hubble's discovery. It has the same effect as a homogeneous fluid with constant energy density ρ_Λ and

[1] "The Nobel Prize in Physics 2011". Nobelprize.org. 15 Sep 2012. http://www.nobelprize.org/nobel_prizes/physics/laureates/2011/

negative pressure $P_\Lambda = -\rho_\Lambda$. Despite its simplicity, the cosmological constant is impressively consistent with major cosmological observations (Komatsu et al., 2011; Reid et al., 2010). The corresponding model, ΛCDM, has become the concordance model of cosmology. The price for its success is an extremely fine–tuned value of Λ; in Planck units, it is of order 10^{-122}. As a curious fact, the dark energy and matter densities in the Universe are presently of the same order, although the latter has been diluted by the cosmic expansion over billions of years and will continue to decrease in the future. The crossover of matter and dark energy in form of a cosmological constant obviously singles out a very special cosmological era, in which we happen to live. This is often referred to as the coincidence or "why now" problem.

The conceptual problems associated with the cosmological constant can be considerably alleviated by assuming a dynamical form of dark energy. The effect of a cosmological constant can be imitated by a slowly evolving scalar field φ. This is realized in models of *Quintessence* (Wetterich, 1988; Ratra and Peebles, 1988). The late–time behavior of these models can be understood from so–called tracker solutions which are independent of the precise initial conditions. Of particular interest is the scaling solution associated with an exponential potential: The energy density of the scalar field decays proportional to the energy density of radiation or matter. Consequently, the huge age of the Universe may provide a natural explanation for the tiny overall scale of the present dark energy density (cf., e. g., Doran and Wetterich, 2003). However, without a mechanism to exit the scaling regime, the scenario lacks an explanation for the onset of dark energy domination and accelerated expansion; the "why now" problem persists. More sophisticated models include the possibility of interactions between the scalar field and other species in the Universe (e. g. Wetterich, 1995; Amendola, 2000). In the framework of coupled quintessence, it has been proposed that cosmic neutrinos may play a key role in explaining the onset of the accelerated expansion (Amendola et al., 2008; Wetterich, 2008). The resultant cosmological model, Growing Neutrino Quintessence (GNQ), forms the basis of this work.

From a particle physics perspective, neutrinos are singled out due to their tiny mass scale m_ν. Indeed, within the standard model of particle physics, only massless neutrinos exist. Nonzero neutrino masses are required to explain the phenomenon of neutrino flavor oscillations (Fukuda et al., 1998). As a lower bound, the data yields $m_\nu \gtrsim 0.05$ eV for at least one neutrino mass eigenstate (e. g. Ahn et al., 2006; Adamson et al., 2012). In fact, m_ν constitutes the only known particle physics scale in the vicinity of the observed dark energy density $\rho_{\mathrm{DE}} \approx (2 \times 10^{-3}\mathrm{eV})^4$. As a key feature, GNQ establishes a fundamental relationship between the physics of neutrino mass and the properties of dark energy (Wetterich, 2008). The model assumes a dependence of the neutrino mass on the quintessence field, $m_\nu = m_\nu(\varphi)$, that leads to a growth of m_ν over time. This mechanism implies an energy–momentum exchange between quintessence and neutrinos that effectively slows down the scalar field once neutrinos have become non–relativistic. The transition from relativistic to non–relativistic neutrinos thus acts as a trigger event that terminates the scaling regime of quintessence. In the subsequent evolution, the scalar field mimics a cosmological constant. Eventually, the dark matter energy density will drop below

the almost constant dark energy density and accelerated expansion will set in. Since, in the early Universe, neutrinos are very light and their temperature is high, the transition naturally happens at late times. In this way, the model addresses the "why now" problem of dark energy. Studying the model at the background level, i. e., under the assumption of a perfectly homogeneous and isotropic universe, gives rise to expansion histories similar to ΛCDM.

In this work, we investigate the implications of GNQ including perturbations to the idealized background. This is, on the one hand, crucial for confronting the model with observational probes such as large–scale matter clustering, weak lensing (WL), or CMB fluctuation spectra. On the other hand, large perturbations may in principle modify the evolution of the cosmological background, a phenomenon known as *backreaction*. While this effect is found to be small within the standard ΛCDM case (e. g. Wetterich, 2003), it is expected to be more important in the model under consideration (Pettorino et al., 2010).

Understanding the evolution of perturbations in GNQ is challenging due to the following fact. In consideration of the small neutrino density in the Universe, the coupling between neutrinos and quintessence needs to be rather strong to have a significant impact on the dark energy evolution. In consequence, the scalar field mediates an attractive force between neutrinos substantially stronger than gravity. Under the influence of this so–called *fifth force*, neutrino perturbations grow rapidly and enter the nonlinear regime soon after neutrinos have turned non–relativistic. Linear perturbation theory breaks down even on large scales (Mota et al., 2008). Though a broad understanding of the nonlinear evolution is still lacking, specific aspects have already been studied and it was possible to identify significant effects (e. g. Wintergerst et al., 2010; Pettorino et al., 2010; Brouzakis et al., 2011; Nunes et al., 2011; Baldi et al., 2011).

The simulation method presented in this work has been developed with the intention to provide the first comprehensive approach towards the full cosmological evolution of GNQ at the nonlinear level. It is our aim to shed some light on its complex dynamics and to point out possibly observable signatures. Growing Neutrino Quintessence provides a compelling mechanism to solve the "why now" problem of dark energy. We will show that it furthermore exhibits a rich phenomenology at the level of perturbations.

Our main references are the already published works Ayaita, Weber, and Wetterich (2012) and Ayaita, Schäfer, and Weber (2012). Within this collaboration, my work focusses particularly on modelling of neutrino physics, constraining the large–scale gravitational potentials, and properties of neutrino lumps.

Outline

We start with a brief review of the basics of cosmology in Chapter 2. After presenting the geometry of the homogeneous and isotropic Universe and the Friedmann equations, we will characterize the constituents of the Universe. Dark energy in form of a cosmological constant and quintessence will be introduced.

Chapter 3 is dedicated to the Growing Neutrino Quintessence model. We collect fundamental equations and explain the mechanism that leads to dark energy domination and accelerated expansion in recent cosmological times. The breakdown

of linear perturbation theory is summarized based on the findings of Mota et al. (2008). We also insert a brief introduction to the general formalism of linear perturbation theory. At the end of the chapter, we consider particle physics aspects related to the neutrino mass.

In Chapter 4, we are interested in direct observational probes of the large–scale gravitational potential Φ. In particular, we attend to 3D WL, a precision method proposed by Heavens (2003). We develop numerical tools for the computation of three–dimensional weak shear spectra for a given evolution $\Phi(z, k)$. As an application, we forecast constraints on the dark energy sound speed c_s^2 from a combination of Euclid and Planck data by virtue of a Fisher matrix analysis.

Chapter 5 provides a detailed description of our simulation method for GNQ. It starts with motivating the general framework. We then explain at length the treatment of the distinct components (neutrinos, quintessence, matter, and gravity). In this context, we also derive necessary equations for the implemented dynamics such as the fully relativistic equation of motion for neutrinos.

The major simulation results are presented and discussed in Chapter 6. We will follow the evolution of neutrino perturbations until the formation of large nonlinear structures. The growth of neutrino velocities will be examined as well as cosmological implications for the gravitational potentials and dark matter. Moreover, we will have a closer look at individual neutrino structures. We point out promising phenomena with regard to observations.

In Chapter 7, we study spherically symmetric neutrino lumps. We briefly consider the motion of test particles in such configurations and derive the conditions for hydrodynamic equilibrium. Numerically, we will investigate the intrinsic equation of state of stable neutrino–cosmon lumps and find a remarkable cancellation of the total pressure.

We conclude and give an outlook in Chapter 8.

Conventions

If not otherwise stated, we use the following units and conventions:

- Natural units: $c = \hbar = k_B = M_P = 1$, with the reduced Planck mass $M_P = \frac{1}{\sqrt{8\pi G}}$.
- Metric signature $(-, +, +, +)$.
- Latin indices run over $1, 2, 3$ and label spatial coordinates. Greek indices run over all four values $0, 1, 2, 3$. Repeated indices are summed.
- A subscript 0 (if not indicating a tensor or vector component) refers to the present time. The scale–factor is normalized so that $a_0 = 1$.
- We use the cosmic time t and the conformal time η. A dot refers to derivatives with respect to t, a prime to derivatives with respect to η.
- Concerning the gravitational potentials, we adopt the sign convention chosen by Ma and Bertschinger (1995): The perturbed metric in the conformal Newtonian gauge reads $\mathrm{d}s^2 = a^2\left[-(1+2\Psi)\mathrm{d}\eta^2 + (1-2\Phi)\mathrm{d}\boldsymbol{x}^2\right]$; $\Psi = \Phi$ in the absence of anisotropic stress.

2 Fundamentals of Cosmology

This chapter introduces the basic concepts of cosmology. In the framework of General Relativity (GR), we will review characteristics of the homogeneous and isotropic Universe and the dynamics of the cosmic expansion in Sec. 2.1. The properties of the matter species in the Universe will be studied and we will discuss observational evidence of dark energy. As prominent candidates, we shall introduce the cosmological constant and quintessence in Sec. 2.2. In parts of this chapter, we will closely follow Weinberg (2008) and Amendola and Tsujikawa (2010).

2.1 Expansion of the homogeneous and isotropic Universe

The assumption of spatial homogeneity and isotropy in the Universe is known as the Cosmological Principle. It is one of the fundamental guiding principles in modern cosmology and is supported by observations of the large–scale galaxy distribution (e. g. Hogg et al., 2005) or the CMB radiation (e. g. Bennett et al., 2003). The Cosmological Principle leads to a specifically simple form of the metric with a single function $a(t)$ describing the expansion of space. In the following sections, we will discuss the geometry associated with this metric, as well as the consequences of Einstein's equations for the evolution of $a(t)$. Clearly, the perfectly isotropic and homogeneous spacetime can only describe the Universe on average, whereas local perturbations have to be taken into account on smaller scales. This will be crucial in subsequent chapters.

2.1.1 The geometry of spacetime and Hubble's law

General Relativity describes physical events as points on a four–dimensional Riemannian manifold, the *spacetime*. The most fundamental field is a Lorentzian metric tensor $g_{\mu\nu}$ defining the geometry of spacetime. The infinitesimal line element $\mathrm{d}s^2 = g_{\mu\nu}\mathrm{d}x^\mu \mathrm{d}x^\nu$ provides a means to compute the physical length of a curve on the manifold. The field equations can be derived from the action

$$S = \int \mathrm{d}^4x \sqrt{-g} \left(\frac{R}{16\pi G} + \mathcal{L}_m \right), \tag{2.1}$$

where G is Newton's gravitational constant, R is the Ricci scalar (the contraction of the Ricci tensor $R_{\mu\nu}$) and $\mathcal{L}_m$ the Lagrangian density of the matter fields. The volume form contains the determinant of the metric $g = \det(g_{\mu\nu})$. Varying the

action with respect to $g_{\mu\nu}$ yields Einstein's equations,

$$R_{\mu\nu} - \frac{1}{2} R\, g_{\mu\nu} = 8\pi G\, T_{\mu\nu}, \tag{2.2}$$

with the energy–momentum tensor associated with the matter fields defined as

$$T_{\mu\nu} = \frac{-2}{\sqrt{-g}} \frac{\delta(\mathcal{L}_m \sqrt{-g})}{\delta g^{\mu\nu}}. \tag{2.3}$$

Solving the set of coupled differential equations for the metric components, Eq. (2.2), can be considerably simplified by assuming spacetime symmetries. In the case of spatial homogeneity and isotropy, the most general form of the metric is given by the Friedmann–Lemaître–Robertson–Walker (FLRW) metric. The FLRW line element can be written as

$$\mathrm{d}s^2 = -\mathrm{d}t^2 + a^2(t) \left(\frac{\mathrm{d}r^2}{1 - kr^2} + r^2 \mathrm{d}\Omega^2 \right), \tag{2.4}$$

with a function $a(t)$ and a constant k. Here, we have chosen spherical coordinates (θ, φ) on three–dimensional hypersurfaces with $\mathrm{d}\Omega^2 = \mathrm{d}\theta^2 + \sin^2\theta\, \mathrm{d}\varphi^2$ as usual.

The function $a(t)$ describes the time dependence of $g_{\mu\nu}$. It universally stretches or contracts distances on spatial hypersurfaces and therefore is called the scale factor. Its evolution follows from Einstein's equations (cf. Sec. 2.1.2). The constant k characterizes the curvature of three–dimensional space. Depending on its sign, the spatial part of the FLRW metric describes three different types of geometry. Constant positive curvature, $k > 0$, corresponds to spherical geometry, whereas constant negative curvature, $k < 0$, corresponds to hyperbolic geometry. For $k = 0$, spatial hypersurfaces are flat and we recover the standard Euclidean metric in three dimensions. The time coordinate chosen in Eq. (2.4) is called the cosmic time t and we refer to the spatial coordinates as comoving coordinates. An observer staying at rest with respect to comoving coordinates observes a perfectly homogeneous and isotropic space and his proper time coincides with the cosmic time. In the following, we clarify the notion of distances in an FLRW Universe.

Physical and comoving distances

Let us consider two distant comoving objects and ask for their proper distance d at a given time t. Without loss of generality, we may assume that the first object is positioned in the origin of the coordinate system, $r_1 = 0$. By virtue of the metric, Eq. (2.4), the proper distance can then be calculated as

$$d(t) = a(t) \int_0^{r_2} \frac{\mathrm{d}r}{\sqrt{1 - kr^2}}, \tag{2.5}$$

where r_2 denotes the radial coordinate of the second object. The proper or physical distance between the two objects evolves proportional to $a(t)$. This allows us to define the time–independent *comoving distance* χ via $d = a\,\chi$. With the usual normalization $a_0 = 1$, comoving and physical distances are identical at the present

time. Assigning $r = 0$ to our own position in the Universe, we can use Eq. (2.5) for calculating the comoving distance between us and any distant object in the Universe. In particular, in the case of a flat universe ($k = 0$), the comoving distance simply coincides with the radial coordinate r of the object. Regarding observations in an expanding Universe, it is crucial to note that light emitted from distant objects provides valuable distance information. In the case of supernovae studies, for instance, the comoving distance χ to the light source can be determined by observations of luminosity and redshift. Since photons follow null geodesics ($\mathrm{d}s^2 = 0$), χ is related to the evolution of $a(t)$ according to

$$\chi = \int_{t_1}^{t_0} \frac{\mathrm{d}t}{a(t)}, \tag{2.6}$$

where t_1 and t_0 refer to the time of emission and observation, respectively. We will come back to this point when we discuss observational evidence for dark energy (cf. Sec. 2.1.3).

Hubble's law

The time evolution of the physical distance $d(t)$ between two comoving objects is governed by the law

$$\dot{d} = Hd, \tag{2.7}$$

where we have introduced the Hubble parameter $H = \dot{a}/a$. Its present value H_0 is often referred to as the Hubble constant. For small distances, H_0 can be inferred from the redshift z of light coming from distant sources. For this purpose, we consider only objects in the close environment of an observer. This allows us to interpret $v = \dot{d}$ as the relative velocity of an object in the rest–frame of the observer (both assumed comoving). As a consequence of the familiar Doppler effect, light emitted from a distant object experiences a redshift defined as $z = \lambda_0/\lambda_1 - 1$ with λ_1 and λ_0 denoting the wavelengths of light at emission and observation, respectively. As long as the relative velocity is small, $v \ll 1$, the Doppler effect yields $z \approx v$. Assuming that the observation takes place at the present time, Eq. (2.7) yields

$$z \approx H_0\, d. \tag{2.8}$$

In 1929, Hubble observed the linear relation between redshift z and distance d with a positive proportionality constant H_0. It was the first observational evidence for an expanding Universe. Although his measurement was affected by large peculiar velocities of the galaxies (perturbing the uniform flow of Eq. 2.7) and considerable uncertainties in the distance measurements, his conclusion has been supported by many observations until today.

The concept of relative velocity can only be applied to close objects. More generally, the FLRW metric implies (see, e. g., Weinberg, 2008)

$$1 + z = \frac{a(t_0)}{a(t_1)}, \tag{2.9}$$

for light emitted at a time t_1 and observed at t_0. The linear relation, Eq. (2.8), can be recovered by expanding $a(t_1) \approx a(t_0)[1 + (t_1 - t_0)H_0]$ and using $d \approx (t_0 - t_1)c$ for close objects.

2.1.2 The Friedmann equations

We now turn to the implications of Einstein's equations (2.2) for the FLRW metric. The most general energy–momentum tensor respecting the assumptions of homogeneity and isotropy takes the form of a perfect fluid,

$$T^{\mu}{}_{\nu} = (\rho + P)u^{\mu}u_{\nu} + P\delta^{\mu}_{\nu}, \tag{2.10}$$

with the energy–density $\rho(t)$, the pressure $P(t)$, and the four–velocity $u^{\mu} = (-1, 0, 0, 0)$ in comoving coordinates. From Einstein's equations, one can derive the following two differential equations for the scale–factor $a(t)$:

$$\left(\frac{\dot{a}}{a}\right)^2 = \frac{8\pi G}{3}\rho - \frac{k}{a^2}, \tag{2.11}$$

$$\frac{\ddot{a}}{a} = -\frac{4\pi G}{3}(\rho + 3P). \tag{2.12}$$

These are the fundamental Friedmann equations. The meaning of Eq. (2.11) becomes most apparent after introducing the critical density $\rho_{\mathrm{crit}} = 3H^2/8\pi G$ and the density parameter $\Omega = \rho/\rho_{\mathrm{crit}}$. It can now be put in the form

$$\Omega - 1 = \frac{k}{(Ha)^2}. \tag{2.13}$$

This expression intimately connects the energy content of the Universe with its geometry. The cases $k < 0$, $k = 0$, and $k > 0$ are equivalent to the conditions $\rho < \rho_{\mathrm{crit}}$, $\rho = \rho_{\mathrm{crit}}$, and $\rho > \rho_{\mathrm{crit}}$. The combination of major observational probes (see, e. g., Reid et al. 2010; Komatsu et al. 2011) allows to tightly constrain the curvature of the Universe. For instance, Reid et al. (2010) find $\Omega = 1.009 \pm 0.012$.[1] Since all observations are consistent with a flat Universe, we will assume $k = 0$ throughout this thesis. A flat Universe may result from cosmic inflation, an early phase of accelerated expansion (Guth, 1981; Linde, 1982). During this period, $(Ha) = \dot{a}$ grows rapidly and drives the right–hand side of Eq. (2.13) to zero. Inflation is also considered as the most promising solution to other puzzles of Big Bang cosmology. In particular, it explains the origin of structure in the Universe by primordial quantum fluctuations (Mukhanov et al., 1992). For a general introduction to inflation, we refer the reader to Lyth and Liddle (2009).

Next, we consider Eq. (2.12). It relates the cosmic acceleration $\ddot{a}$ to the total energy density ρ and pressure P of the Universe. Assuming the weak energy condition (cf. Carroll, 2004), $\rho \geq 0$, a positive acceleration $\ddot{a} > 0$ is only possible for

[1] Here, they assume a constant dark energy equation of state which not necessarily equals -1.

negative pressure $P < 0$. In terms of the equation of state parameter,

$$w = \frac{P}{\rho}, \tag{2.14}$$

the general condition for accelerated expansion reads $w < -1/3$. If the Universe was made up of ordinary matter and radiation only, this would be impossible (cf. Sec. 2.1.3). Generally, the equation of state w is a function of time. It is nonetheless instructive to consider the case $w = \text{const.}$, which is a good approximation over long periods of the cosmic evolution. Here, we restrict ourselves to the case $w > -1$ (in the context of the cosmological constant, Sec. 2.2.1, we will also discuss the case $w = -1$). The explicit solution of Eqs. (2.11) and (2.12) for $k = 0$ is then given by

$$a(t) \propto (t - t_i)^{\frac{2}{3(1+w)}}, \tag{2.15}$$

with a constant t_i (cf., e. g., Amendola and Tsujikawa, 2010). Such a universe starts to expand from a singularity, $a(t_i) = 0$, and the expansion continues forever. The age of the universe follows as

$$(t_0 - t_i) = \frac{2}{3(1+w)} H_0^{-1}. \tag{2.16}$$

Hence, the Hubble time H_0^{-1} sets the natural scale of the cosmic age. With the common parameterization, $H_0 = 100\,h\ \mathrm{Mpc}^{-1}\ \mathrm{km/s}$, we obtain

$$H_0^{-1} \approx 9.78 \times 10^9 h^{-1} \mathrm{yr}. \tag{2.17}$$

Observations suggest h of the order unity. As we will discuss at the end of the next section, dark energy is also necessary to reconcile lower bounds on the age of the Universe with the theoretical prediction.

2.1.3 The constituents of the Universe

In this section, we will classify the constituents of the Universe and discuss their role for the cosmic expansion. The total energy density ρ and pressure P used in the previous section are recovered as the sum over the individual contributions ρ_i and P_i (with a suitable subscript for each species). We will also use individual density parameters $\Omega_i = \rho_i/\rho_{\mathrm{crit}}$ and equation of state parameters $w_i = P_i/\rho_i$. By virtue of the flatness condition $\sum_i \rho_i = \rho_{\mathrm{crit}}$, the total equation of state parameter w is related to the individual w_i by $w = \sum_i \Omega_i w_i$. Hence, during periods in which a single species dominates the energy budget of the Universe, $\Omega_i \approx 1$ (for a specific label i), this species determines the dynamics of the expansion.

If a component does not interact with others, its individual energy–momentum tensor is conserved,

$$\nabla_\mu T^{\mu\nu}_{(i)} = 0. \tag{2.18}$$

In terms of energy density and pressure, the conservation law reads

$$\dot{\rho}_i = -3H(\rho_i + P_i). \tag{2.19}$$

The corresponding equation for the total energy density ρ and pressure P can also be derived from the Friedmann equations (2.11) and (2.12).

Radiation: photons and neutrinos

The radiation component embraces photons and relativistic particles in the Universe. The equation of state of radiation is $w_r = 1/3$ (for a derivation from the phase–space distribution function, cf., e. g., Amendola and Tsujikawa, 2010). The energy–density of a relativistic species in thermal equilibrium only depends on the temperature T and on the number of internal degrees of freedoms. The photon energy–density ρ_γ is given by

$$\rho_\gamma = \frac{\pi^2}{15} T_\gamma^4. \tag{2.20}$$

After the discovery of the CMB (Penzias and Wilson, 1965), its black–body spectrum and fluctuation pattern had been measured by the satellite missions Cosmic Background Explorer (COBE) and Wilkinson Microwave Anisotropy Probe (WMAP). The present temperature was found to be $T_\gamma^0 = 2.725 \pm 0.002$ K (Mather et al., 1994), yielding

$$\Omega_\gamma^0 = \frac{\rho_\gamma^0}{\rho_{\rm crit}} \approx 2.47 \times 10^{-5} h^{-2}. \tag{2.21}$$

At this point, we note that photons are no longer in thermal equilibrium today.[2] Rather, they are freely propagating through the Universe while the form of their spectrum is kept unchanged. Due to the cosmic expansion, photon frequencies experience a redshift, $\nu \propto a^{-1}$. Consequently, at very early times, photon energies were much higher than today. Likewise, we can follow the evolution of matter back in time and will arrive at an epoch at which the energy densities were too high for the formation of bound atoms. Rapid scattering processes between photons and electrons kept photons in thermal equilibrium at that time. When the temperature had dropped to about $3,000$ K, the last interactions took place and free photon propagation began. Defining a time dependent temperature,

$$T_\gamma(a) = T_\gamma(a_L) \left(\frac{a_L}{a} \right), \tag{2.22}$$

with a subscript L referring to the event of last scattering, the photon distribution at later times can conveniently be written in the equilibrium form,

$$f_\gamma(\nu, a) \propto \frac{1}{\exp\left(\frac{h\nu}{k_B T_\gamma(a)} \right) - 1}, \tag{2.23}$$

with Planck's constant h and Boltzmann's constant k_B.

If the masses of neutrinos are small, they can be treated similar to photons and their energy density ρ_ν is fully described by the neutrino temperature T_ν. Taking into account that neutrinos are fermions and come in different flavors, the energy

[2] A detailed review of the Universe's thermal history can be found in standard textbooks, e. g., Weinberg, 2008. We will only summarize important results.

density is given by

$$\rho_\nu = N_{\text{eff}} \frac{7}{8} \frac{\pi^2}{15} T_\nu^4, \tag{2.24}$$

with $N_{\text{eff}} = 3$ for standard model neutrinos. At very early times, neutrinos were also in thermal equilibrium with the primordial plasma due to weak interactions, e. g. $\mathrm{e}^+ + \mathrm{e}^- \rightleftharpoons \nu + \bar{\nu}$. Following Weinberg (2008), the collision rate associated with these processes can be approximated as $\Gamma_\nu \approx G_F^2\, T^5$ with the Fermi constant G_F. Thermal equilibrium can only be maintained as long as Γ_ν is larger than the expansion rate H. The latter evolves during radiation domination as $H = \sqrt{\rho/3} \propto T^2$. Inserting the numerical factors, one finds

$$\frac{\Gamma_\nu}{H} \approx \left(\frac{T}{10^{10}\mathrm{K}} \right)^3. \tag{2.25}$$

Therefore, at temperatures considerably below 10^{10} K, neutrinos can no longer be kept in equilibrium. After decoupling, they follow geodesics and can be described by a temperature $T_\nu(a) \propto a^{-1}$ analogously to $T_\gamma(a)$. Just as in the case of photons, the form of the distribution function at the time of decoupling is preserved. In the case of neutrinos, it is given by the relativistic Fermi–Dirac distribution

$$f_\nu(p, a) \propto \frac{1}{\exp(\frac{pc}{k_B T_\nu}) + 1}. \tag{2.26}$$

This also applies to massive neutrinos, since at the time of decoupling neutrino masses are negligible compared to the high temperatures. The relativistic energy–momentum relation $\varepsilon \approx pc$ thus remains an excellent approximation.

Assuming that neutrinos decoupled instantaneously once the collision rate Γ_ν has dropped below the expansion rate H, one can derive the following relationship between the neutrino and photon temperatures at late times:

$$T_\nu = \left(\frac{4}{11} \right)^{1/3} T_\gamma. \tag{2.27}$$

A more accurate treatment suggests slight corrections, which are usually taken into account by setting $N_{\text{eff}} = 3.04$ (cf., e. g., Dolgov 2002).

In this thesis, we investigate a model in which neutrinos are coupled to dark energy. As a consequence, the neutrino mass will grow in time and neutrinos feel an additional attractive force once they have become non–relativistic. From this time on, they will no longer follow geodesics. Still, the considerations above remain perfectly valid at the early stages of the Universe. This will be of relevance when we draw initial conditions for our simulations of GNQ (Chapter 5). The parameter T_γ^0 will then be used as in the standard case, although it does no longer describe the distribution of neutrinos at the present time.

From above, we obtain $T_\nu^0 = 1.945$ K. For standard (uncoupled) neutrinos, this implies $\Omega_\nu^0 \approx 0.7\, \Omega_\gamma^0$ (cf. Eq. 2.24). Taken together, the present radiation density parameter only amounts to

$$\Omega_r^0 \approx 8 \times 10^{-5}, \tag{2.28}$$

for $h \approx 0.7$. Neglecting energy–momentum exchange with other species, we may use Eq. (2.19) to extrapolate ρ_r back in time. The solution is $\rho_r(a) = \rho_r^0 a^{-4}$. Although the contribution of radiation is negligible today, it dominated the Universe in former times. During radiation domination, the evolution of the scale factor is approximately described by Eq. (2.15) with $w = 1/3$: $a(t) \propto (t - t_i)^{1/2}$.

Baryons and cold dark matter

Non–relativistic matter is characterized by a negligible pressure, $P_m \ll \rho_m$, corresponding to $w_m \approx 0$. According to Eq. (2.19), the energy density of matter in the Universe scales as

$$\rho_m \propto a^{-3}. \tag{2.29}$$

Baryonic matter (atomic nuclei and electrons) belongs to this class. During the radiation dominated era, it was coupled to photons. The interplay of gravity and photon–baryon pressure gave rise to acoustic waves in the primordial plasma. A snapshot of these oscillations is imprinted in the CMB anisotropies and, on the other hand, in the distribution of galaxies in the Universe. The latter is referred to as baryon acoustic oscillations (BAO) and has been detected in the matter correlation function (Eisenstein et al., 2005). Current constraints from a combination of CMB and BAO data (Komatsu et al., 2011), together with precise measurements of H_0 (Riess et al., 2009), yield

$$\Omega_b^0 = 0.0458 \pm 0.0016. \tag{2.30}$$

This is consistent with the bound inferred from the amount of light elements produced by Big Bang nucleosynthesis (BBN): $\Omega_b^0 h^2 = 0.020 \pm 0.002$, at the 95% confidence level. An increase of the baryon density accelerates the process of helium formation and decreases the abundance of deuterium (see Amendola and Tsujikawa, 2010, for details). We conclude that the baryonic matter component makes up only about 4.6% of the present energy budget of the Universe.

An additional matter component, the so called *dark matter*, has already been proposed in the early 1930s by Fritz Zwicky. Using the virial theorem, he found that the amount of luminous matter in galaxy clusters was not enough to explain the observed velocity dispersion among the galaxies. The same is true for individual galaxies; the rotational speeds of stars in the outer regions of spiral galaxies are almost constant instead of following the law $v \propto r^{-1/2}$, expected if most of the mass were located in the luminous center of the galaxy. For a more detailed discussion of the virial theorem and a comprehensive summary of the most important observational studies of this field, see Weinberg (2008). The missing matter is assumed to be in large spherical halos surrounding the galaxies.

The nature of dark matter is still one of the greatest mysteries of modern physics. Its existence, however, has been supported by many independent observations including data from CMB anisotropies, SN Ia, and WL. Particularly, gravitational lensing can provide direct evidence for the presence of dark matter. A prominent example is the so–called *Bullet Cluster*, a cluster merger for which the center of baryonic mass significantly deviates from the peaks in the total mass distribution (Clowe et al., 2006). Dark matter is also crucial for the formation of galaxies. Assuming baryonic matter only, small–scale inhomogeneities would have been damped

out by radiative diffusion in the early Universe (Silk, 1968). Since dark matter does not interact with photons, it is not affected by this and may provide the necessary seed of perturbations on scales relevant for galaxy formation. On this account, it is also crucial that the major part of dark matter is "cold", i. e., it was non–relativistic at the time of photon decoupling. Otherwise, small scale inhomogeneities would have been canceled by thermal motion.

A characteristic scale below which thermal motion is relevant is given by the "free–streaming" length $\lambda_{\rm fs} \propto v_{\rm th}/H$ comparing the thermal velocity $v_{\rm th}$ to the expansion rate.[3] If one assumes for instance "hot" dark matter in the form of massive neutrinos (cf., e. g., Lesgourgues and Pastor, 2006), the free–streaming length during matter domination is approximately of the order

$$\lambda_{fs}^{(\nu)} \approx \sqrt{a} \left(\frac{1\mathrm{eV}}{m_\nu} \right) 20\,\mathrm{Mpc}, \tag{2.31}$$

for $h \approx 0.7$. In this scenario, inhomogeneities form on large scales first. Observations and numerical simulations of structure formation (e. g. Davis et al., 1985) have made a case for cold dark matter (CDM) with negligible thermal motion on cosmological scales instead. The currently best estimate of the present CDM density parameter quoted by the WMAP team (Komatsu et al., 2011) is

$$\Omega_c^0 = 0.229 \pm 0.015. \tag{2.32}$$

Particle physics has put forward several dark matter candidates. The most prominent ones are axions and Weakly Interacting Massive Particles (WIMPs), e. g. in the form of the lightest supersymmetric particles. A large class of experiments tries to detect dark matter scattering in terrestrial detectors or to find signatures of dark matter annihilation in the galactic halo. Complementary data comes from particle accelerators, especially from the Large Hadron Collider (LHC). It is expected, that these programmes will be able to put several of the proposed dark matter candidates to stringent tests. For a recent review of dark matter research including the experimental and observational status, see Bergstrom (2012).

Dark energy

From the previous considerations, we may already conclude that in addition to matter and radiation another form of energy is needed to fulfill the flatness condition $\Omega = 1$. Convincing observational evidence for dark energy was found in studies of SN Ia (Perlmutter et al., 1999; Riess et al., 1998). This type of supernovae provides a powerful distance measure in the expanding Universe since their absolute luminosity L can be deduced from the shape of their light curves; due to this property one speaks of *standard candles*. Together with the observed light flux F, it is possible to measure the so–called luminosity distance

$$d_L^2 = \frac{L}{4\pi F}. \tag{2.33}$$

[3] The numerical factor is usually chosen in analogy to the Jeans length, $\lambda_{\rm fs} = 2\pi\sqrt{\frac{2}{3}}\frac{v_{\rm th}}{H}$ (Lesgourgues and Pastor, 2006).

The luminosity distance can be related to the redshift z of the supernova and its comoving distance χ via $d_L = a_0\chi(1+z)$ (see, e. g., Weinberg, 2008, for derivation). As we have already anticipated in Sec. 2.1, the comoving distance to a light source is directly related to the expansion history of the Universe. This carries over to the luminosity distance:

$$d_L = (1+z)\int_0^z \frac{\mathrm{d}z'}{H(z')}, \tag{2.34}$$

where we have used the substitution $t \mapsto z$ with $\mathrm{d}z/\mathrm{d}t = -(1+z)H$ in Eq. (2.6). Measuring the luminosity distance over a range of redshifts is thus a sensitive probe of the expansion rate in recent cosmological times. Both of the aforementioned groups found strong evidence for an accelerating expansion, $\ddot{a} > 0$. As we have seen in Sec. 2.1.2, this requires a negative equation of state parameter, $w < -2/3$. The supernovae results are consistent with a dark energy component of constant equation of state $w_{\mathrm{DE}} = -1$. More recent compilations of SN Ia data combined with other cosmological observations yield $w_{\mathrm{DE}} = -0.969^{+0.059}_{-0.063}\ (\mathrm{stat})^{+0.063}_{-0.066}\ (\mathrm{sys})$ (Kowalski et al., 2008). It is important to note, that this constraint mainly applies to the low–redshift regime, $z < 1$, and w_{DE} is not necessarily constant in time.

Taking dark energy into consideration has also an important impact on the estimated age of the Universe. According to Eq. (2.16), the age of a pure matter universe amounts to $2/3\, H_0^{-1} \approx 9.3 \times 10^9\mathrm{yr}$ (assuming $h \approx 0.7$). Including the radiation component slightly reduces the age but has no large effect. This estimate is in conflict with the estimated ages of the oldest stars in the Milky Way, e. g. $(15.8 \pm 2.1) \times 10^9\mathrm{yr}$ (Bolte and Hogan, 1995). Dark energy solves the problem by increasing the age of the Universe. Adopting for instance the cosmological constant Λ (cf. Sec. 2.2.1), one obtains

$$\begin{aligned}(t_0 - t_i) &= H_0^{-1}\int_0^\infty \frac{\mathrm{d}z}{(1+z)\left[\Omega_{m,0}(1+z)^3 + \Omega_{r,0}(1+z)^4 + \Omega_{\Lambda,0}\right]^{1/2}} \\ &\approx 13.73 \times 10^9\ \mathrm{yr}.\end{aligned} \tag{2.35}$$

Observational evidence for dark energy comes from SN Ia, the CMB, BAO, the large–scale structure, and estimates of ages in the Universe (for a comprehensive summary and discussion, we refer to Amendola and Tsujikawa, 2010). In the next section, we will introduce prominent candidates and also discuss their major problems.

2.2 Dark energy candidates

We now have a closer look at the cosmological constant Λ and scalar–field dark energy. The fundamental coincidence problem will be discussed in both frameworks. Here, we restrict ourselves to the simplest quintessence models involving an uncoupled scalar field. Our discussion forms the basis for the introduction of couplings in the next chapter.

We will not consider the field of *modified gravity* in this work. Generally, modifications to the laws of gravity are severely constrained by local gravity tests. Nonetheless, large–scale modifications are in principle possible and may give rise

to accelerated expansion. An introduction to theories of modified gravity can be found in recent reviews (e. g. Clifton et al., 2012; Nojiri and Odintsov, 2006; Carroll et al., 2005) and textbooks (e. g. Amendola and Tsujikawa, 2010).

2.2.1 The cosmological constant

The cosmological constant Λ is the simplest possibility to achieve accelerated expansion. It was already introduced by Einstein himself as a possible modification to the fundamental equations of GR. Since his original intention was to realize a static Universe, he, however, abandoned it again after Hubble's discovery of the cosmic expansion. The field equations including a cosmological constant term read

$$R_{\mu\nu} - \frac{1}{2} R\, g_{\mu\nu} + \Lambda\, g_{\mu\nu} = 8\pi G\, T_{\mu\nu}. \tag{2.36}$$

From a different point of view, the cosmological constant can be considered as part of the energy–momentum tensor on the right–hand side of the Einstein equations. It then appears as

$$T^{\mu\nu}_{(\Lambda)} = -\frac{\Lambda}{8\pi G}\, g^{\mu\nu}, \tag{2.37}$$

corresponding to a perfect fluid with constant energy density $\rho_\Lambda = \Lambda/8\pi G$ and pressure $P_\Lambda = -\rho_\Lambda$. In this way, we may stick to the original field equations (2.2) as well as the standard Friedmann equations (2.11) and (2.12). Since the equation of state parameter associated with a cosmological constant is $w_\Lambda = -1$, it can generate a positive acceleration of the expansion. For a flat universe with $\Omega_\Lambda = 1$, the Friedmann equation (2.11) yields a constant Hubble parameter $H = \sqrt{\Lambda/3}$ implying an exponentially growing scale factor $a(t) \propto \exp(\sqrt{\Lambda/3}\, t)$. If the cosmological constant actually causes the observed accelerated expansion, our Universe is currently undergoing the transition to such a phase of rapid expansion.

The cosmological constant is often related to the concept of vacuum energy arising in quantum field theories. Since local Lorentz invariance requires the vacuum energy–momentum tensor to be proportional to $g_{\mu\nu}$, its contribution is indistinguishable from a cosmological constant. Stated differently, the above introduced Λ can be considered as an effective quantity including the fundamental cosmological constant and the vacuum contributions (cf., e. g., Martin, 2012). This leads to the well–known fine–tuning problem. If Λ shall explain the present cosmic acceleration, its energy density needs to be of the same order as

$$\rho^0_{\mathrm{crit}} = 3H_0^2/(8\pi G) \approx 10^{-123} m_{\mathrm{P}}^4, \tag{2.38}$$

with the Planck mass $m_{\mathrm{P}} = \sqrt{\hbar c/G} \approx 10^{19}$ GeV. The contribution to the vacuum energy of a specific quantum field depends on the cutoff scale $k_{\max}$ of the theory. Assuming that GR is valid up to the Planck scale, we choose $k_{\max}$ identical to the Planck mass. For a field with mass m, the vacuum energy can then be estimated according to

$$\rho_{\mathrm{vac}} = \int_0^{k_{\max}} \frac{\mathrm{d}^3 k}{(2\pi)^3}\, \frac{1}{2} \sqrt{k^2 + m^2} \approx 10^{-2}\, m_{\mathrm{P}}^4. \tag{2.39}$$

Description	*Estimate*
Hubble parameter H_0	(70.2 ± 1.4) (km/s)/Mpc
Baryon density parameter Ω_b^0	0.0458 ± 0.0016
CDM density parameter Ω_c^0	0.229 ± 0.015
Dark energy density parameter Ω_Λ^0	0.725 ± 0.016
Scalar amplitude A_s	$(2.43 \pm 0.091) \times 10^{-9}$
Spectral index n_s	0.968 ± 0.012

Table 2.1: Currently best estimates of the ΛCDM parameters quoted by the WMAP team (Komatsu et al., 2011). The scalar amplitude and the spectral index describe the primordial spectrum of perturbations (cf. Sec. 3.3.1).

Consequently, the observationally preferred value of ρ_Λ is about 121 orders of magnitude below the naive expectation. Though only a crude estimation, the result points towards a miraculous cancellation. This famous discrepancy is often referred to as the cosmological constant problem. For a comprehensive review of the problem including precise calculations of vacuum energy contributions, we refer to Martin (2012).

The second puzzle which cannot be resolved by a cosmological constant is the coincidence or "why now" problem of dark energy: Although the energy density ρ_Λ stays constant in time, observations suggest that it is of the same order of magnitude as the matter energy density just today. Bearing in mind that ρ_m has been diluted over billions of years, this appears as a miraculous coincidence. For $\Omega_\Lambda^0 \approx 0.7$, equality of the two energy densities occurred at

$$a_{\mathrm{eq}} = (\Omega_m^0/\Omega_\Lambda^0)^{1/3} \approx 0.75, \tag{2.40}$$

very close to the present scale factor (in terms of redshift, $z_{\mathrm{eq}} \approx 0.3$). At earlier times, for instance at $z \approx 10$ when the first galaxies formed, the impact of the cosmological constant was completely negligible and would not have been observable at all. On the other hand, the ratio Ω_Λ/Ω_m grows as a^3 and Ω_m would soon become completely unimportant.

Despite of its two fundamental problems, the cosmological constant is consistent with all major cosmological observations (Komatsu et al., 2011; Sullivan et al., 2011; Reid et al., 2010). The ΛCDM model has become the standard picture of cosmology and its parameters are constrained with ever increasing accuracy. In Tab. 2.1, we quote current estimates. In Fig. 2.1, we plot the resulting evolution of the energy densities and density parameters in the ΛCDM universe, highlighting again the coincidence problem.

The theoretical problems associated with the cosmological constant motivate the search for alternative explanations of dark energy in which these problems are absent or at least alleviated. This brings us to the class of dynamical dark energy. In this framework, it is generally assumed that the cosmological constant vanishes exactly due to some fundamental symmetry.

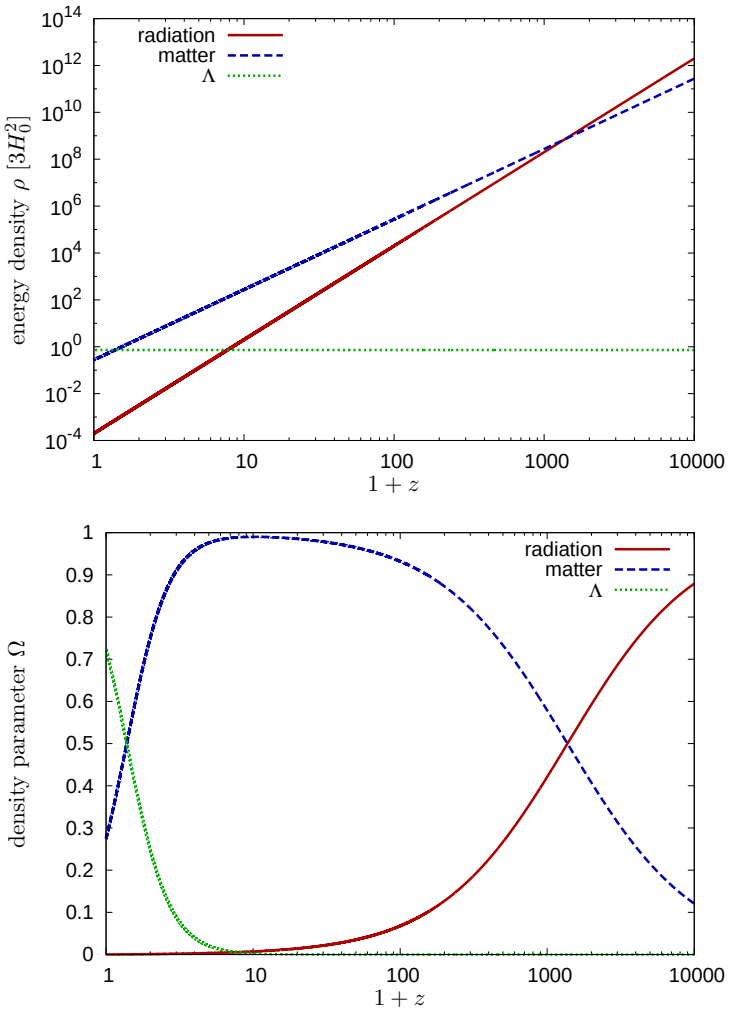

Figure 2.1: Evolution of the energy densities (in units of the present critical density $3H_0^2$) and the corresponding density parameters in a ΛCDM universe with the parameters given in Tab. 2.1.

2.2.2 Quintessence

A dynamical form of dark energy rather than a cosmological constant is, in the simplest case, realized by a scalar field. Dark energy in this form is known as *quintessence*. We will further refer to the scalar field as the *cosmon* φ. Its dynamics follow from the action principle with an appropriate choice of a Lagrangian density $\mathcal{L}_\varphi$. Generally, we have to assume that the total Lagrangian density of the theory also contains couplings between the cosmon and other species of the Universe. This possibility plays a crucial role in the context of this thesis and will be explored in Chapter 3. For now, we follow the first proposals of quintessence (Wetterich, 1988; Ratra and Peebles, 1988) and study the case of an uncoupled scalar field. The dynamics are then governed by gravity and a self–coupling potential $V(\varphi)$.

Assuming a standard kinetic term, the Lagrangian density reads

$$\mathcal{L}_\varphi = -\frac{1}{2}\partial_\mu\varphi\,\partial^\mu\varphi - V(\varphi). \tag{2.41}$$

Many choices of $V(\varphi)$ have been studied in the literature (cf., e. g., Doran and Wetterich, 2003; Brax et al., 2000; Skordis and Albrecht, 2002; Steinhardt et al., 1999; Zlatev et al., 1999). We will discuss two popular examples below, of which the exponential potential $V(\varphi) \propto \exp(-\alpha\varphi)$ will be adopted in subsequent chapters. The Lagrangian density, Eq. (2.41), leads to the Klein–Gordon equation in curved spacetime,

$$-\nabla_\mu\nabla^\mu\varphi + V_{,\varphi}(\varphi) = 0, \tag{2.42}$$

with the common abbreviation $V_{,\varphi} = \mathrm{d}V/\mathrm{d}\varphi$. The energy–momentum tensor follows as

$$T^{\mu\nu}_{(\varphi)} = \partial^\mu\varphi\,\partial^\nu\varphi + g^{\mu\nu}\mathcal{L}_\varphi. \tag{2.43}$$

In contrast to the cosmological constant, quintessence naturally varies in time. Moreover, once we include perturbations to the homogeneous and isotropic background, spatial variations in φ are possible. Indeed, they will play a crucial role in the context of structure formation in Growing Neutrino Quintessence. Yet, at this point, we continue our discussion within the framework of a perfectly homogeneous universe and assume $\varphi = \varphi(t)$. In this case, we recover the energy–momentum tensor of a perfect fluid, cf. Eq. (2.10), with the energy density and pressure given by

$$\rho_\varphi = \frac{1}{2}\dot\varphi^2 + V(\varphi), \tag{2.44}$$

$$P_\varphi = \frac{1}{2}\dot\varphi^2 - V(\varphi), \tag{2.45}$$

implying the equation of state parameter

$$w_\varphi = \frac{\frac{1}{2}\dot\varphi^2 - V(\varphi)}{\frac{1}{2}\dot\varphi^2 + V(\varphi)}. \tag{2.46}$$

This expressions allows for a range of values $-1 \leq w_\varphi \leq 1$. The case of a cosmological constant can be imitated by a slowly varying field: $w_\varphi \approx -1$ for $\dot\varphi^2/2 \ll V(\varphi)$. In contrast to an actual cosmological constant, however, w_φ generally varies in time.

Together with the FLRW metric, Eq. (2.4), the equation of motion (2.42) for $\varphi(t)$ becomes

$$\ddot\varphi + 3H\dot\varphi + V_{,\varphi}(\varphi) = 0. \tag{2.47}$$

The self–coupling potential introduces a force which is counteracted by a damping term due to the cosmic expansion. In order to cause accelerated expansion, successful models of quintessence need to provide a "slowly rolling" scalar field in recent cosmological times. Furthermore, the presence of early dark energy is constrained by complementary probes like BBN, the formation of large–scale structure, and the fluctuation spectrum of the CMB. This allows to put constraints on the model

parameters of quintessence cosmologies. Let us now consider specific examples.

Exponential potential

The exponential potential is of the form

$$V(\varphi) = M^4 \exp\left(-\alpha\varphi\right), \tag{2.48}$$

with a dimensionless parameter $\alpha > 0$ and a constant M with units of mass (the value of $V(0)$ is arbitrary and can be changed by shifting φ). It can be motivated by the anomaly of the dilatation symmetry (Wetterich, 1988) and naturally arises in higher–dimensional theories (Wetterich, 2008). The basic features of a scalar field with an exponential potential in the context of cosmology are reviewed by Wetterich (1995); Doran and Wetterich (2003).

As an intriguing property, many quintessence models feature *tracker solutions*. These are special trajectories to which the evolution of φ converges for a large range of initial conditions. By this means, the late–time evolution of φ (under the assumption of convergence) only depends on parameters of the potential and not on the precise initial values. An instructive discussion of tracker solutions and fixed points in quintessence scenarios can be found in the textbook by Amendola and Tsujikawa (2010). The exponential potential, Eq. (2.48), provides tracker solutions with a particularly interesting feature: ρ_φ decays with the same rate as the energy density of the dominating species in the Universe, $\rho_\varphi \propto a^{-n}$ $(n = 4, 3)$; this is the so–called *scaling solution*. In this way, the huge age of the Universe provides a natural explanation for the small overall size of ρ_φ today.

The scaling solution implies that the dark energy density parameter Ω_φ stays constant during radiation or matter domination. Its value is

$$\Omega_\varphi = \frac{n}{\alpha^2}, \tag{2.49}$$

with $n = 4$ during radiation domination and $n = 3$ during matter domination. Early dark energy constraints based on CMB data (Doran et al., 2007) require $\alpha \gtrsim 10$.

Despite the tempting possibility to avoid the cosmological constant problem, the scaling solution presented above has the major drawback that it does not provide a transition to dark energy domination. If the scaling continues forever, the model cannot explain the presently accelerating expansion of the Universe. A coupling between the cosmon φ and other species in the Universe may provide a possible solution to this problem (see Chapter 3).

Inverse power–law potential

Ratra and Peebles (1988) proposed a potential of the form

$$V(\varphi) = M^{4+\alpha}\varphi^{-\alpha}, \tag{2.50}$$

where α is a positive constant and M has units of mass. This model provides a

tracker solution with an almost constant equation of state at late times,

$$w_\varphi \approx \frac{-2}{\alpha + 2}. \tag{2.51}$$

At earlier times, the evolution is more complicated (cf., e. g., Weinberg, 2008).

Accelerated expansion is possible for $\alpha < 1$. Since observations suggest $w_\varphi^0 \approx -1$, the parameter α needs to be chosen close to zero. Unlike the exponential potential, the tracker solution of this model provides a transition to dark energy domination. However, the present amount of dark energy or, equivalently, the time of matter–dark energy equality are very sensitive to the choice of the parameters α and M. A simple comparison of scales (Weinberg, 2008) leads to the condition

$$M^{4+\alpha} \approx G^{-1-\alpha/2} H_0^2. \tag{2.52}$$

With α close to zero, this is a similar fine–tuning problem as in the case of the cosmological constant Λ. Although the simplest quintessence models already exhibit appealing features, it remains difficult to solve both of the problems associated with the cosmological constant.

3 Growing Neutrino Quintessence

At the end of the previous chapter, we have studied quintessence as an alternative to the cosmological constant. We have presented scaling solutions that may explain why the dark energy density is small and comparable to the matter density at present times. Within the free theory, it is, however, challenging to find a natural explanation for the recent onset of accelerated expansion. This problem can be addressed in models of coupled quintessence as discussed in Sec. 3.1. Particularly, we will introduce Growing Neutrino Quintessence (GNQ), the central model for this thesis, which proposes a coupling between quintessence and neutrinos. After summarizing its basic concepts, we will derive the fundamental equations from an action principle (Sec. 3.2); the computation is also part of the publication Ayaita et al. (2012b). For the further discussion of the model, it is necessary to introduce linear perturbation theory (Sec. 3.3). The breakdown of linear perturbation theory serves as the motivation for developing nonlinear methods, which will be presented in this work (Chapter 5). We conclude this chapter with a brief look at the physics of neutrino mass and the specific particle physics realization of GNQ proposed by Wetterich (2007).

3.1 Motivation and overview

The total energy–momentum tensor appearing on the right–hand side of Einstein's equations (2.2) is conserved, i. e. $\nabla_\alpha T^{\alpha\beta}_{\text{tot}} = 0$. In the absence of interactions, this property carries over to the individual energy–momentum tensors describing the constituents of the Universe. Within the standard framework, this is assumed to be the case after the epoch of last scattering (cf. Sec. 2.1.3). With the introduction of a dynamical dark energy field φ, however, additional interactions are generally to be expected if not forbidden by any symmetry. Formally, a coupling between two species is represented by an energy–momentum exchange, i. e., only the sum of the two corresponding energy–momentum tensors $T^{\alpha\beta}$ and $S^{\alpha\beta}$ is conserved while the individual tensors are not:

$$\nabla_\alpha T^{\alpha\beta} = +Q^\beta \tag{3.1}$$

$$\nabla_\alpha S^{\alpha\beta} = -Q^\beta. \tag{3.2}$$

We will now investigate the case of coupled quintessence in order to find a solution to the coincidence problem of dark energy. In the following, $S^{\alpha\beta}$ will denote the energy–momentum tensor of the cosmon φ; $T^{\alpha\beta}$ corresponds to a specific matter component, e. g. CDM, baryons + CDM, or neutrinos. A specific form of the coupling, studied for instance by Amendola (2000) and Wetterich (1995), is given

by

$$Q^\alpha = -\beta\, T\, \partial^\alpha \varphi, \tag{3.3}$$

where β is a dimensionless coupling parameter and $T = T^\alpha{}_\alpha$. For the energy–momentum tensor of a perfect fluid, Eq. (2.10), we obtain $T = -\rho + 3P = -\rho(1 - 3w)$. Hence, the coupling vanishes for radiation with $w = 1/3$. Cosmological observations and local experiments impose severe constraints on the coupling to ordinary matter. One finds $\beta_b^2 < 10^{-3}$ for the cosmon–baryon coupling and $\beta_c < 0.1$ for the coupling to CDM (cf. Wetterich, 1995, Amendola and Quercellini, 2003, and references therein[1]). Even if a coupling between dark energy and matter causes the onset of accelerated expansion, the question remains why this happens just in recent times. In order to avoid a new fine–tuning problem, a kind of cosmic "trigger event" would be desirable. This is possible with a cosmon–neutrino coupling as proposed by Amendola et al. (2008). In a particle physics realization of this scenario, Wetterich (2007) motivated a particularly strong coupling between dark energy and neutrinos (cf. Sec. 3.4.2). Therefore, we will neglect possible couplings between dark energy and ordinary matter and assume $T^{\alpha\beta}$ being the energy–momentum tensor of neutrinos from now on.

Cosmology with a cosmon–neutrino coupling

The equations of motion for the coupled cosmon–neutrino fluid follow from Eqs. (3.1) to (3.3):

$$\ddot{\varphi} + 3H\dot{\varphi} + V_{,\varphi}(\varphi) = \beta\, \rho_\nu\, (1 - 3w_\nu), \tag{3.4}$$

$$\dot{\rho}_\nu + 3H(1 + w_\nu)\rho_\nu = -\beta\, \rho_\nu\, (1 - 3w_\nu)\dot{\varphi}. \tag{3.5}$$

We assume an exponential potential $V(\varphi) \propto \exp(-\alpha\varphi)$ with $\alpha > 0$. Comparing Eq. (3.4) with the uncoupled case, Eq. (2.47), we identify an additional force term $\propto \rho_\nu(1 - 3w_\nu)$ on the right–hand side. This term may counteract the driving force $-V_{,\varphi}$ and slow down the evolution of φ. The neutrino equation of state w_ν acts as a "switcher": As long as neutrinos are highly relativistic, $w_\nu \approx 1/3$, the coupling is ineffective and the cosmon field evolves just like a free field. On the other hand, once the neutrino temperature has considerably fallen below the neutrino mass scale m_ν, the equation of state approaches the limit $w_\nu = 0$; the term $\beta\rho_\nu$ then modifies the further evolution of φ. This motivates the definition of an effective potential,

$$\begin{aligned} -\frac{\mathrm{d}V_{\mathrm{eff}}}{\mathrm{d}\varphi} &= -\frac{\mathrm{d}V}{\mathrm{d}\varphi} + \beta\rho_\nu \\ &= \alpha V(\varphi) + \beta\rho_\nu. \end{aligned} \tag{3.6}$$

For $\beta < 0$, the two terms are counteracting and may cancel. The effective potential $V_{\mathrm{eff}}(\varphi)$ then exhibits a minimum. It is possible to stop the further evolution of the cosmon field by this mechanism and thereby provide an exit from the scaling

[1] The precise constraints depend on the chosen class of potential $V(\varphi)$. Amendola and Quercellini (2003) for instance use an inverse–power law potential.

solution discussed in Sec. 2.2.2 (Amendola et al., 2008). From this moment on, φ will act similar to a cosmological constant with w_φ close to -1. In contrast to the previously discussed free theory, the scenario contains late–time cosmic acceleration whose onset is triggered by the event of neutrinos becoming non–relativistic. In this way, the model addresses the "why now" problem of dark energy. However, the coupling has to be rather strong since the neutrino density is small in the Universe. Typical values are of the order $\beta \sim -10^2$.

We show the cosmological evolution for a viable set of parameters in Fig. 3.1. The figure not only highlights the transition from the scaling regime to the dark energy dominated era, but also the consequences for the evolution of the neutrino component. Apart from the distinct oscillatory features, the neutrino energy density is almost constant at late times and will soon start to dominate over the matter energy density. Obviously, the energy–momentum exchange between neutrinos and quintessence has drastic impacts on both species. This is plausible regarding the particle physics implications of the coupling.

Growing neutrino mass

On a particle physics level, the coupling is realized as a cosmon–depending neutrino mass, $m_\nu = m_\nu(\varphi)$. Here, we consider the average neutrino mass m_ν instead of distinguishing between the three neutrino species. The coupling parameter β then arises as

$$\beta = -\frac{\mathrm{d}\ln m_\nu}{\mathrm{d}\varphi}. \tag{3.7}$$

This relationship can be obtained by introducing a cosmon–depending mass in the energy–momentum tensor of neutrinos and exploiting the continuity equation for the total energy density $\rho_\mathrm{tot} = \rho_\nu + \rho_\varphi$ (cf. Amendola and Tsujikawa, 2010). One arrives at Eq. (3.4) with the above identification of β. Alternatively, one may define β via Eq. (3.7) and derive the equations of motions from an action principle. This approach will be presented in Sec. 3.2. Mass varying neutrinos are also considered in other scenarios (e. g. Fardon et al., 2004; Gu et al., 2003).

In general, the parameter β is a function of φ instead of being constant (cf. Wetterich, 2007, and Sec. 3.4.2). However, if not otherwise stated, we will assume the simplest case of a constant coupling parameter β, corresponding to

$$m_\nu \propto \exp\left(-\beta\,\varphi\right). \tag{3.8}$$

While φ is "rolling down" its potential, the neutrino mass is steadily growing. If we, for instance, assume a present neutrino mass of the order eV, it was even much smaller in the early Universe. This has to be taken into account when asking for the redshift z_nr at which the transition from relativistic to non–relativistic neutrinos takes place. For a present neutrino mass $m_\nu(t_0) \leq 2.3$ eV, this typically happens in the recent cosmological history, $z_\mathrm{nr} \approx 5$–10 (Mota et al., 2008). The strong link between the phenomenology of dark energy and the neutrino mass becomes also evident in the effective equation of state describing the combined cosmon–neutrino

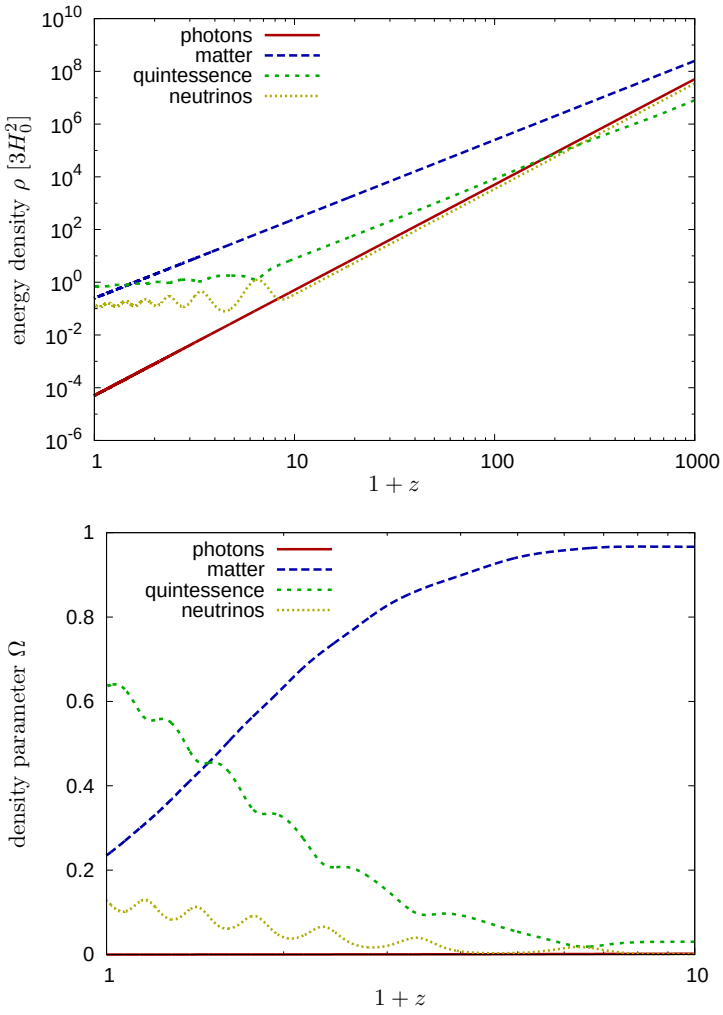

Figure 3.1: The upper figure shows the evolution of the energy densities in GNQ with $\beta = -52$ and a present neutrino mass $m_\nu^0 = 2.3$ eV (cf. Amendola et al., 2008). The lower figure shows the evolution of the density parameters in recent cosmological times. Dark energy dominates the Universe at present.

fluid (Amendola et al., 2008):

$$w_{\text{eff}} \approx -1 + \frac{m_\nu^0}{12\text{eV}}, \tag{3.9}$$

This intriguing relation yields $w_{\text{eff}} < -0.8$ for $m_\nu(t_0) < 2.3$ eV.

3.2 Fundamental equations from an action principle

In this section, we will derive the fundamental equations presented above from an action principle (Ayaita et al., 2012b). Instead of including three different neutrino species, we assume a degenerate neutrino mass (alternatively, one may think of m_ν as the average neutrino mass). Under this working hypothesis, the number of neutrino flavors enters only in the initial number density of neutrinos.

We describe the dynamics of the cosmon φ and the neutrino field ψ by a standard scalar–field Lagrangian $\mathcal{L}_\varphi$ and a Majorana Lagrangian $\mathcal{L}_\nu$ (neutrinos are generally expected to be Majorana particles, cf. Sec. 3.4),

$$\mathcal{L}_\varphi = -\frac{1}{2}\,\partial_\alpha\varphi\,\partial^\alpha\varphi - V(\varphi), \tag{3.10}$$

$$\mathcal{L}_\nu = \mathrm{i}\,\bar\psi\,\left(\gamma^\alpha\nabla_\alpha + m_\nu(\varphi)\right)\,\psi, \tag{3.11}$$

where we have included a cosmon–dependent neutrino mass $m_\nu = m_\nu(\varphi)$. The quantities $\gamma^\alpha(x)$ are a generalization of the usual Dirac matrices γ^a $(a = 0, 1, 2, 3)$ in curved spacetime based on the vierbein formalism (cf., e. g., Brill and Wheeler, 1957). The vierbein $e^\alpha_a(x)$ is related to the metric via $g^{\alpha\beta} = e^\alpha_a e^\beta_b \eta^{ab}$, with the Minkowski metric $\eta^{ab} = \mathrm{diag}(-1, 1, 1, 1)$. By virtue of the vierbein, we have $\gamma^\alpha(x) = \gamma^a e^\alpha_a(x)$. The field $\bar\psi$ is related to ψ by a Majorana constraint. The total action of the theory reads

$$S = \int \mathrm{d}^4x\,\sqrt{-g}\,\left(\mathcal{L}_0 + \mathcal{L}_\nu + \mathcal{L}_\varphi\right), \tag{3.12}$$

where $\mathcal{L}_0$ represents gravity and the remaining cosmological species.

Varying the action with respect to $\psi, \bar\psi$ yields the Dirac equations in curved spacetime,

$$\gamma^\alpha\nabla_\alpha\psi + m_\nu(\varphi)\psi = 0, \tag{3.13}$$

$$-\nabla_\alpha\bar\psi\,\gamma^\alpha + m_\nu(\varphi)\bar\psi = 0. \tag{3.14}$$

The neutrino energy–momentum tensor $T^{\alpha\beta}$ associated with $\mathcal{L}_\nu$ can be calculated from the usual definition (Brill and Wheeler, 1957) and follows as

$$T^{\alpha\beta} = -\frac{\mathrm{i}}{2}\,\bar\psi\gamma^{(\beta}\nabla^{\alpha)}\psi + \frac{\mathrm{i}}{2}\nabla^{(\alpha}\bar\psi\gamma^{\beta)}\psi. \tag{3.15}$$

In the uncoupled case, i. e. $m_\nu = \text{const.}$, the equations of motion (3.13) and (3.14) imply the conservation law $\nabla_\beta T^{\alpha\beta} = 0$. In the considered case, however, the

derivative also acts on $m_\nu(\varphi(x))$ leading to

$$\begin{aligned}\nabla_\beta T^{\alpha\beta} &= \partial^\alpha m_\nu(\varphi)\,\mathrm{i}\bar{\psi}\psi \\ &= \beta\, m_\nu(\varphi)\,\partial^\alpha\varphi\,\tilde{n}_\nu,\end{aligned} \tag{3.16}$$

where, in the last step, we have used the definition of the coupling parameter $\beta = -\mathrm{d}\ln m_\nu/\mathrm{d}\varphi$ and introduced the quantity $\tilde{n}_\nu = -\mathrm{i}\,\bar{\psi}\psi$.

Computing the trace of the energy–momentum tensor (3.15), we find

$$T = T^\alpha{}_\alpha = -m_\nu(\varphi)\tilde{n}_\nu. \tag{3.17}$$

In the non–relativistic limit, $T \approx -\rho_\nu$ and we can identify $\tilde{n}_\nu$ with the neutrino number density n_ν. In general, however, $\tilde{n}_\nu$ transforms as a scalar, while n_ν does not (even in flat spacetime, n_ν picks up volume contraction factors under Lorentz boosts).

Combining Eqs. (3.16) and (3.17), we obtain the equation of energy–momentum exchange,

$$\nabla_\beta T^{\alpha\beta} = -\beta\, T\,\partial^\alpha\varphi, \tag{3.18}$$

corresponding to Eq. (3.1) with the coupling specified in Eq. (3.3).

Varying the action, Eq. (3.12), with respect to φ yields the modified Klein–Gordon equation,

$$-\nabla^\alpha\nabla_\alpha\varphi + V_{,\varphi}(\varphi) = -\beta\, T. \tag{3.19}$$

The energy–momentum tensor associated with $\mathcal{L}_\varphi$ is found to be

$$S^{\alpha\beta} = \partial^\alpha\varphi\,\partial^\beta\varphi + g^{\alpha\beta}\mathcal{L}_\varphi, \tag{3.20}$$

and one can straightforwardly verify the second exchange equation

$$\nabla_\beta S^{\alpha\beta} = +\beta\, T\,\partial^\alpha\varphi, \tag{3.21}$$

in accordance with Eq. (3.2).

The introduction of a varying neutrino mass $m_\nu = m_\nu(\varphi)$ on a fundamental level leads to the coupling equations of the previous section.

3.3 Linear perturbations

So far, we have only considered GNQ in a perfectly homogeneous and isotropic universe. We will now introduce perturbations on the FLRW background. As long as these perturbations are *small*, it is appropriate to incorporate only first–order corrections. This is, for instance, extremely useful in the standard ΛCDM model, where perturbations are still linear on large scales. In GNQ, however, Mota et al. (2008) have shown that neutrino perturbations grow non–linear in recent times even on large scales. This motivates a more accurate treatment, which will be the topic of Chapter 5. We will now quickly review linear perturbation theory (mainly based on Doran, 2008, and Ma and Bertschinger, 1995) and summarize the findings of Mota et al. (2008) afterwards. In the context of perturbation theory, we will use

the conformal time η which is related to the cosmic time t via $\mathrm{d}t = a\mathrm{d}\eta$.

3.3.1 General formalism

We first split into homogeneous background quantities $\bar{g}_{\alpha\beta}(\eta)$, $\bar{T}_{\alpha\beta}(\eta)$ and perturbations $\delta g_{\alpha\beta}(\eta, \boldsymbol{x})$, $\delta T_{\alpha\beta}(\eta, \boldsymbol{x})$ varying in time and space. The most general form of the perturbed FLRW metric $g_{\alpha\beta} = \bar{g}_{\alpha\beta} + \delta g_{\alpha\beta}$ reads

$$\mathrm{d}s^2 = a^2(\eta)[-(1+2A(\eta,\boldsymbol{x}))\mathrm{d}\eta^2 - 2B_i(\eta,\boldsymbol{x})\mathrm{d}\eta\mathrm{d}x^i + (\delta_{ij}+2H_{ij}(\eta,\boldsymbol{x}))\mathrm{d}x^i\mathrm{d}x^j]. \quad (3.22)$$

Perturbations are usually expanded in scalar, vector, and tensor modes by virtue of appropriate basis functions (cf., e. g., Doran, 2008). We will restrict ourselves to scalar perturbations, in which case we recover the usual Fourier decomposition for a function

$$A(\eta, \boldsymbol{x}) = \int \frac{\mathrm{d}^3k}{(2\pi)^3} A(\eta, \boldsymbol{k}) Q_{\boldsymbol{k}}(\boldsymbol{x}), \quad (3.23)$$

with the basis function $Q_{\boldsymbol{k}}(\boldsymbol{x}) = \exp(\mathrm{i}\boldsymbol{k}\cdot\boldsymbol{x})$. As a short hand, we usually simply write $A(\eta, \boldsymbol{x}) = A(\eta)Q$. Defining $Q_i = -k^{-1}\partial_i Q$ and $Q_{ij} = k^{-2}\partial_i\partial_j Q + 1/3\,\delta_{ij}Q$ with $k = |\boldsymbol{k}|$, we construct the scalar modes of vector and tensor fields,

$$B_i(\eta, \boldsymbol{x}) = B(\eta)Q_i, \quad (3.24)$$

$$H_{ij}(\eta, \boldsymbol{x}) = H_L(\eta)Q\delta_{ij} + H_T(\eta)Q_{ij}. \quad (3.25)$$

Before turning to the perturbed energy–momentum tensor, we make use of the gauge freedom in order to simplify the form of the perturbed metric, Eq. (3.22). Gauge transformations arise from infinitesimal coordinate transformations that keep perturbations small. While ordinary coordinate transformations would also change the unperturbed background, gauge transformations, by definition, only affect the perturbation quantities (for a derivation of the transformation laws, cf., e. g., Doran, 2008; Ma and Bertschinger, 1995). In this thesis, we will use the conformal Newtonian gauge ($H_T = B = 0$),

$$\mathrm{d}s^2 = a^2(\eta)\left[-(1+2\Psi(\eta,\boldsymbol{x}))\mathrm{d}\eta^2 + (1-2\Phi(\eta,\boldsymbol{x}))\mathrm{d}\boldsymbol{x}^2\right], \quad (3.26)$$

using the sign conventions of Ma and Bertschinger (1995).

We now introduce perturbations to the energy–momentum tensor of the perfect fluid. The perturbed energy density and pressure become $\rho = \bar{\rho} + \delta\rho$ and $P = \bar{P} + \delta P$; we will also use the density contrast $\delta = \delta\rho/\bar{\rho}$. In addition, we take into account the coordinate (or peculiar) velocity $v^i = \mathrm{d}x^i/\mathrm{d}\eta$, related to the four–velocity u^i via $u^i = v^i/a$ to first order in perturbations.[2] Moreover, we allow for an anisotropic stress tensor $\Sigma^i{}_j$. The entries of the energy–momentum tensor in

[2]Since v^i is not a tensor, we do not distinguish between upper and lower indices, i. e. $v_i = \delta_{ij}\,v^j$.

linear perturbation theory (cf. Ma and Bertschinger, 1995) then are

$$\begin{aligned} T^0{}_0(\eta,\boldsymbol{x}) &= -\left[\bar{\rho}(\eta)+\delta\rho(\eta,\boldsymbol{x})\right], \\ T^0{}_i(\eta,\boldsymbol{x}) &= \left[\bar{\rho}(\eta)+\bar{P}(\eta)\right] v^i(\eta,\boldsymbol{x}) = -T^i{}_0(\eta,\boldsymbol{x}), \\ T^i{}_j(\eta,\boldsymbol{x}) &= \left[\bar{P}(\eta)+\delta P(\eta,\boldsymbol{x})\right]\delta^i_j + \Sigma^i{}_j(\eta,\boldsymbol{x}), \quad \Sigma^i{}_i = 0. \end{aligned} \tag{3.27}$$

The peculiar velocity v^i, as defined above, appears as the perturbation to the uniform Hubble flow due to peculiar motion: $\dot{\boldsymbol{d}} = \partial_t(a\boldsymbol{r}) = H\,\boldsymbol{d} + a\dot{\boldsymbol{r}} = H\,\boldsymbol{d} + \boldsymbol{v}$, where we have used $\partial_\eta = a\partial_t$. In the following, we will use a prime to indicate derivatives with respect to η. It is useful to define the conformal Hubble parameter $\mathcal{H} = a'/a = aH$.

Evolution of perturbations

The evolution of perturbations follows from the perturbed Einstein equations $\delta G^\alpha{}_\beta = 8\pi G\,\delta T^\alpha{}_\beta$ (for a computation of the perturbed Einstein tensor, cf., e. g. Amendola and Tsujikawa, 2010). In Fourier space, each mode $\boldsymbol{k}$ evolves independently and we can omit the basis function $Q_{\boldsymbol{k}}$. One of the fundamental equations is the relativistic Poisson equation for the metric perturbation Φ:

$$k^2\Phi = -\frac{1}{2}a^2\left(\delta\rho + 3\frac{\mathcal{H}}{k}(\bar{\rho}+\bar{P})\,v\right), \tag{3.28}$$

where v is the scalar part of the velocity perturbation (cf. Eq. 3.24), $v_i = v\,Q_i$. On subhorizon scales (the most important case for us), $k \gg \mathcal{H}$, the equation can be simplified to

$$k^2\Phi = -\frac{1}{2}a^2\delta\rho. \tag{3.29}$$

In the non–relativistic limit, $\delta\rho$ describes the distribution of mass and Φ can be identified with the usual Newtonian gravitational potential. The second metric perturbation Ψ follows from

$$k^2(\Phi-\Psi) = a^2\Sigma, \tag{3.30}$$

where Σ is the scalar part of the anisotropic stress tensor,[3] $\Sigma_{ij} = \Sigma\cdot Q_{ij}$ ($\Sigma_L = 0$ per definition). The dominant contribution to anisotropic stress comes from relativistic neutrinos (Ma and Bertschinger, 1995). This may have interesting implications in the context of GNQ as we will discuss later (Chapter 6). In the absence of anisotropic stress, the metric perturbations equal each other, $\Phi = \Psi$. Due to their meaning in the Newtonian limit, we usually speak of the two gravitational potentials Ψ and Φ.

In the uncoupled case, the evolution of matter perturbations is described by the relativistic continuity and Euler equations,

$$\delta'_m = -k\,v_m + 3\Phi', \tag{3.31}$$

$$v'_m = -\mathcal{H}v_m + k\Psi, \tag{3.32}$$

[3] In order to avoid confusion, we remark that Σ corresponds to $\bar{P}\Pi$ in the notation of Doran (2008) and to $\frac{3}{2}(\bar{\rho}+\bar{P})\sigma$ in the notation of Ma and Bertschinger (1995).

where v_m is the scalar part of the matter peculiar velocity. Gravitational acceleration is mediated by the gradient of Ψ, while the cosmic expansion enters in form of a damping term $\propto \mathcal{H}v$. These equations remain valid in GNQ.

The situation is more complicated for relativistic species like photons and neutrinos. Even without any coupling, the treatment outlined above is not appropriate, since the velocity perturbations can no longer be treated linearly. Instead, one considers the full phase–space distribution function

$$f(\eta, x^i, q, n_j) = \bar{f}(q, \eta) \left(1 + \psi(\eta, x^i, q, n_j)\right), \tag{3.33}$$

where $q_j = q n_j$ is the comoving three–momentum with magnitude q and direction n_j, $\bar{f}(q, \eta)$ is the Fermi–Dirac (or Bose–Einstein) distribution with a time–dependent temperature (cf. Sec. 2.1.3), and ψ denotes a linear perturbation. The distribution function f allows to reconstruct the full energy–momentum tensor. The evolution of ψ is governed by the Boltzmann equation,

$$\frac{\mathrm{d}f}{\mathrm{d}\eta} = \frac{\partial f}{\partial \eta} + \frac{\mathrm{d}x^i}{\mathrm{d}\eta}\frac{\partial f}{\partial x^i} + \frac{\mathrm{d}q}{\mathrm{d}\eta}\frac{\partial f}{\partial q} + \frac{\mathrm{d}n_j}{\mathrm{d}\eta}\frac{\partial f}{\partial n_j} = C[f], \tag{3.34}$$

with a possible collision term $C[f]$ (e. g. due to Compton scattering). In GNQ, the cosmon–dependent neutrino mass $m_\nu = m_\nu(\varphi(x))$ generates additional terms when a derivative acts on the momentum q (Ichiki and Keum, 2008; Mota et al., 2008). The Boltzmann equation is usually solved as follows (cf. Ma and Bertschinger, 1995). While the spatial coordinates are transformed to Fourier space, $\boldsymbol{x} \mapsto \boldsymbol{k}$, the momentum q is integrated out in order to reduce the number of variables. The dependence on the momentum direction $\boldsymbol{n}$ is expanded in a series of Legendre polynomials $P_\ell(\hat{\boldsymbol{k}} \cdot \boldsymbol{n})$ ($\hat{\boldsymbol{k}} = \boldsymbol{k}/k$) allowing to project out moment equations for each ℓ. The resulting hierarchy of equations is truncated at some $\ell_{\max}$ in order to achieve a finite set of scalar perturbation equations.

In models of quintessence, we also have to consider perturbations to the cosmon field, $\varphi(\eta, \boldsymbol{x}) = \bar{\varphi}(\eta) + \delta\varphi(\eta, \boldsymbol{x})$. These are obtained from the perturbed Klein Gordon equation (cf., e. g., Mota et al., 2008, and Sec. 5.3.1).

Initial conditions

In Fourier space, the linear perturbation equations discussed above are a set of coupled ordinary differential equations in time depending only on the magnitude $k = |\boldsymbol{k}|$ but not on the direction of the Fourier mode $\boldsymbol{k}$. Hence, the general solution $A(\eta, \boldsymbol{k})$ for an arbitrary perturbation variable A can be written as a superposition of normal modes $A_{n,k}(\eta)$ which depend only on k and η (cf. Weinberg, 2008):

$$A(\eta, \boldsymbol{k}) = \sum_n \alpha_n(\boldsymbol{k})\, A_{n,k}(\eta). \tag{3.35}$$

While the functions $A_{n,k}(\eta)$ belong to the specific perturbation variable A, the coefficients $\alpha_n(\boldsymbol{k})$ are the same for all perturbations. Let us for simplicity assume

that only a single mode is dominant[4] and drop the index n (for a thorough discussion, see, e. g., Weinberg, 2008). Still, we have an infinite number of coefficients $\alpha(\boldsymbol{k})$ that need to be fixed by initial conditions. These are traced back to quantum fluctuations generated during inflation. This provides a powerful probabilistic description:

1. The initial perturbation fields $\hat{A}(\boldsymbol{k})$ are *Gaussian random fields*, i. e., they are fully characterized by their two–point functions $\langle \hat{A}(\boldsymbol{k})\, \hat{A}^*(\boldsymbol{k}')\rangle$. Under the assumption of statistical homogeneity and isotropy, the correlation function can be written as

$$\langle \hat{A}(\boldsymbol{k})\, \hat{A}^*(\boldsymbol{k}')\rangle = (2\pi)^3\, P_{\hat{A}}(k)\, \delta_D^3(\boldsymbol{k}-\boldsymbol{k}'), \tag{3.36}$$

   defining the power spectrum $P_{\hat{A}}(k)$.

2. The *primordial spectrum* $P_{\mathrm{prim}}(k)$ is nearly scale–invariant, commonly parameterized as

$$P_{\mathrm{prim}}(k) = \frac{2\pi^2}{k^3}\, A_s \left(\frac{k}{k_{\mathrm{pivot}}}\right)^{n_s-1}, \tag{3.37}$$

   with the spectral index $n_s \approx 1$ and the scalar amplitude A_s normalized at a pivot scale k_{pivot}. Here, we choose to normalize the mode functions so that the k–dependence of the primordial spectrum is fully attributed to the spectrum of $\alpha(\boldsymbol{k})$,

$$\left\langle \alpha(\boldsymbol{k})\, \alpha^*(\boldsymbol{k}')\right\rangle = (2\pi)^3 P_{\mathrm{prim}}(k)\, \delta_D^3(\boldsymbol{k}-\boldsymbol{k}'). \tag{3.38}$$

The time–evolution of linear perturbations, Eq. (3.35), then implies

$$\langle A(\eta,\boldsymbol{k})\, A^*(\eta,\boldsymbol{k}')\rangle = (2\pi)^3\, |A_k(\eta)|^2\, P_{\mathrm{prim}}(k)\, \delta_D^3(\boldsymbol{k}-\boldsymbol{k}'). \tag{3.39}$$

Analogous relations hold for higher n–point functions. Consequently, linear perturbation theory preserves Gaussianity and the spectrum of A at some time η can be obtained by multiplying the primordial spectrum with the factor $|A_k(\eta)|^2$. The latter can be efficiently calculated with the help of Boltzmann codes like CAMB (Lewis et al., 2000) or CMBEASY (Doran, 2005).

Finally, the *adiabatic mode* which is predicted by the most prominent models of inflation refers to initial conditions of the type

$$\delta_\gamma = \frac{4}{3}\delta_c = \frac{4}{3}\delta_b = \delta_\nu = \frac{4}{3}(1+w_\varphi)^{-1}\delta_\varphi, \tag{3.40}$$

together with additional constraints for the velocity perturbations (Doran et al., 2003). The overall amplitude of the perturbations has to be fixed by observations.

[4] The assumption of a single mode (adiabatic perturbations) is in concordance with models of single–field inflation, cf., e. g., Tsujikawa (2003).

3.3.2 Breakdown of linear perturbation theory

Mota et al. (2008) have implemented the linear perturbation equations for GNQ in modified versions of the cosmological Boltzmann codes CAMB (Lewis et al., 2000) and CMBEASY (Doran, 2005). Without quoting the full equations here, we point out that the scalar field gives rise to a *fifth force* acting on neutrinos. The Euler equation governing the neutrino acceleration v'_ν contains a term $\propto -k\,\beta\,\delta\varphi$ in addition to the gravitational acceleration $k\Psi$. Studying the perturbed Klein–Gordon equation for $\delta\varphi$ in the Newtonian limit[5] (see also Wintergerst et al., 2010) shows, that $k\,\delta\varphi \approx 2|\beta|k\,\Psi_\nu$, with Ψ_ν denoting the neutrino induced gravitational potential. Hence, the cosmon perturbations $\delta\varphi$ mediate a new attractive forth between neutrinos with the strength of $2\beta^2$ compared to gravity. For typical values, $\beta \sim -10^2$, this force is extremely strong.

As a result, Mota et al. (2008) find a rapid growth of neutrino perturbations once the coupling becomes effective. In turn, the cosmon perturbations $\delta\varphi$ and the gravitational potential Φ strongly grow and the linear approximation breaks down soon. At redshift $z_{\rm nl} \lesssim 2$, overdensities in the neutrino fluid have become non–linear on supercluster scales ($k \lesssim 0.1h/\mathrm{Mpc}$). These results suggest substantial neutrino clustering on large scales. The details of the clustering process and its consequences for the cosmological evolution of GNQ cannot be studied within the linear approximation and motivate non–linear methods for further analyses. Of particular interest are the magnitude of the large–scale gravitational potential and the integrated Sachs–Wolfe effect (ISW) due to late–time growth of the gravitational potential (cf. Sec. 4.1), and the effects on dark matter perturbations (Mota et al., 2008). The method presented in this work (Chapter 5) is specifically designed to explore GNQ beyond the linear level. In Chapter 6, we will come back to the aforementioned observables.

The peculiarity of nonlinear perturbations on large cosmic scales is due to the relativistic nature of neutrinos in the early Universe. As mentioned in Sec. 2.1.3, relativistic species damp out perturbations below their free–streaming length. Consequently, neutrino perturbations first grow on large scales as is known from "hot dark matter" scenarios.

3.4 Neutrino mass

We complete our introduction of GNQ with a quick review of the concept of neutrino masses in particle physics. In Sec. 3.4.1, we summarize important bounds on the neutrino mass and briefly introduce neutrino mass terms as extensions to the standard model. Afterwards, we will turn to the particle physics realization of GNQ presented by Wetterich (2007).

3.4.1 Experimental and theoretical aspects

The standard model of particle physics provides only left–handed neutrinos and assumes vanishing neutrino masses. The detection of neutrino flavor oscillations

[5] The perturbation equation for $\delta\varphi$ will be discussed in more detail in Sec. 5.3.1.

(Fukuda et al., 1998), however, requires neutrinos to have mass. The amplitudes of flavor oscillations depend on the quadratic mass splittings $\Delta m_{ij}^2 = |m^2(\nu_i) - m^2(\nu_j)|$ with $i, j = 1, 2, 3$ for three families. Neutrino oscillation experiments consequently allow to constrain differences between the neutrino masses. Concerning the absolute mass scales, at least, lower bounds can be inferred. For instance, Ahn et al. (2006) report a best–fit value of $\Delta m^2 = 2.8 \times 10^{-3}$ eV^2 for the oscillation between ν_μ and ν_τ flavor states. This corresponds to a lower limit $m_\nu \gtrsim 0.05$ eV for at least one neutrino species. Consistent results are also found by Adamson et al. (2012). Direct constraints on the absolute neutrino mass scale are challenging, but can in principle be inferred from the kinematics of beta decay, cosmological and astrophysical observations, and the neutrinoless double beta decay (see Rodejohann, 2011, for a recent review of experimental methods, focusing on the neutrinoless double beta decay). A conservative upper bound on the mass of the electron neutrino has been obtained from experiments on tritium beta spectroscopy: $m_{\nu_e} \leq 2.3$ eV at the 95% confidence level (Kraus et al., 2005). Considerable improvements are expected from KATRIN, a tritium beta decay experiment intended to measure the electron neutrino mass with sub–eV sensitivity (Osipowicz et al., 2001). Upper bounds on the sum of the neutrino masses can also be inferred from cosmology. Considering the possibility of a time–varying neutrino mass, it is, however, crucial to note that these bounds apply to the neutrino masses in the early Universe, particularly during the epoch of structure formation. The WMAP team (Komatsu et al., 2011) quotes $\sum m_\nu = 0.58$ eV (at the 95% confidence level); if neutrino masses are measured today that significantly exceed this bound, this would strongly support the idea of a growing neutrino mass.

Following Kayser (2003), we will now briefly review the theoretical aspects of neutrino mass. For simplicity, we consider the case of a single neutrino species. A possible extension of the standard model assumes the existence of a right–handed neutrino ν_R in addition to the left–handed standard model neutrino ν_L. The most general mass term constructed from these fields reads

$$\mathcal{L}_{m_\nu} = -m_D \, \overline{\nu_R} \nu_L - \frac{m_L}{2} \, \overline{\nu_L^c} \nu_L - \frac{m_R}{2} \, \overline{\nu_R^c} \nu_R + \text{h.c.}, \tag{3.41}$$

with a Dirac mass m_D and a left–handed and right–handed Majorana mass, m_L and m_R, respectively. Here, $\nu_{R,L}^c$ denotes the charge–conjugate field. Majorana mass terms are forbidden for charged fermions due to electric charge conservation (a Majorana mass term for quarks, for instance, would imply transitions between quarks and antiquarks). The Dirac masses in the standard model arise from Yukawa couplings to the Higgs field and are of the form $h_i d$, with h_i denoting a coupling constant and d the vacuum expectation value of the Higgs doublet of the order $d \sim 10^2$ GeV. Thus, if we do not assume an extremely small coupling h_ν between neutrinos and the Higgs, the scale of m_D is expected to be much larger than the typical scale of neutrino masses. Since neutrinos are electrically neutral and right–handed fermions are usually described as weak–isospin singlets (which we adopt for ν_R), the presence of a right–handed Majorana mass term for neutrinos (in addition to the Dirac mass term) is compatible with the standard model gauge group. The

total mass term can then be rewritten as

$$\mathcal{L}_{m_\nu} = -\frac{1}{2}\,(\overline{\nu_L^c}, \overline{\nu_R}) \begin{pmatrix} 0 & m_D \\ m_D & m_R \end{pmatrix} \begin{pmatrix} \nu_L \\ \nu_R^c \end{pmatrix} + \text{h.c.} \tag{3.42}$$

The symmetric matrix

$$M = \begin{pmatrix} 0 & m_D \\ m_D & m_R \end{pmatrix} \tag{3.43}$$

can be diagonalized. Assuming $m_R \gg m_D$, the eigenvalues are given by

$$m_1 \approx \frac{m_D^2}{m_R} \quad \text{and} \quad m_2 \approx m_R, \tag{3.44}$$

In terms of the mass eigenstates, Eq. (3.42) becomes

$$\mathcal{L}_{m_\nu} = -\sum_{i=1}^{2} \frac{m_i}{2} \overline{\nu_i} \nu_i, \tag{3.45}$$

The fields ν_i fulfill the Majorana condition $\nu_i^c = \nu_i$ (see, e. g., Kayser, 2003). Consequently, the combination of Dirac and Majorana mass terms predicts Majorana neutrinos. The mechanism outlined above is known as the "seesaw mechanism" due to relation (3.44). In order to obtain a light neutrino mass of the order 10^{-1} eV, m_R needs to be of order 10^{15} GeV if $h_\nu \lesssim 1$.

Extending the formalism to three families of neutrinos, the parameters m_D and m_R are replaced by 3×3 matrices M_D and M_R. The seesaw relation (3.44) then involves the matrix product $M_D\, M_R^{-1}\, M_D^T$. Additionally, we also consider the possibility of generating neutrino masses by effective dimension five operators without the necessity for right–handed neutrinos. This contribution is accounted for by a matrix M_L. The most general mass matrix for the three species of light neutrinos reads

$$M_\nu = M_D\, M_R^{-1}\, M_D^T + M_L. \tag{3.46}$$

The induced triplet mechanism (Wetterich, 2007, and references therein) gives $M_L = h_L\, \gamma\, d^2/M_t^2$, where M_t is the mass of a heavy $\mathrm{SU}(2)_L$ triplet field, $\gamma \sim M_{B-L}$ is associated with the characteristic scale of B (baryon number) – L (lepton number) violating effects, and h_L is a dimensionless coupling constant.

3.4.2 Varying neutrino mass

The previous considerations lead to the following expression for the average neutrino mass m_ν:

$$m_\nu = \frac{h_\nu^2 d^2}{m_R} + \frac{h_L \gamma d^2}{M_t^2}. \tag{3.47}$$

A growing neutrino mass can be realized by introducing a time dependence either of M_t or m_R. Realizing a cosmon–dependent triplet mass, Wetterich (2007) proposes

$$M_t^2 = c_t\, M_{GUT}^2 \left[1 - \frac{1}{\tau} \exp(-\varepsilon\varphi)\right], \tag{3.48}$$

with dimensionless parameters c_t and τ of the order one, a negative parameter $\varepsilon < 0$, and the grand unification scale $M_{GUT} \sim 10^{16}$ GeV. The crucial feature of this expression is that it has a zero for $\varphi_t = -\varepsilon^{-1} \ln \tau$. As a consequence, m_ν rapidly increases when φ approaches φ_t. A Taylor expansion of $M_t(\varphi)$ around φ_t yields

$$m_\nu(\varphi) = \frac{\bar{m}_\nu}{\varepsilon(\varphi - \varphi_t)}, \tag{3.49}$$

with a constant $\bar{m}_\nu$ of characteristic size $\bar{m}_\nu \approx 3 \times 10^{-5}$ eV. Here, the seesaw contribution has been neglected.

The equation of motion for the cosmon φ, Eq. (3.4), now includes a time–dependent coupling $\beta(\varphi)$. In the vicinity of φ_t, it is approximately of the form

$$\beta(\varphi) = \frac{1}{\varphi - \varphi_t}. \tag{3.50}$$

The coupling can become arbitrarily large in this scenario and will efficiently slow down φ once it approaches φ_t. Hence, the evolution of φ will be almost stopped and $V(\varphi_t)$ acts as an effective cosmological constant. Choosing exemplary parameters resulting in a present neutrino mass $m_\nu^0 = 0.44$ eV, the model provides an expansion history very close to the standard ΛCDM case (Wetterich, 2007). The crossover to the regime with an almost constant dark energy density happens in recent times, at $z_c \approx 5$. Together with the scaling solution provided by the exponential potential, the model avoids the two fundamental problems associated with the cosmological constant.

The divergence of the neutrino mass for $\varphi \to \varphi_t$ is the reason for a very strong coupling between quintessence and neutrinos. Thus, compared to other standard model particles, neutrinos are singled out by the specific mechanism by which they acquire mass. In the subsequent chapters, we will return to the simpler case of a constant, but rather large, coupling parameter β and neglect couplings between dark energy and other species.

4 Observing the Large–Scale Potentials: 3D WL

The present chapter contains an excursus on a precision method for observing the large–scale gravitational potentials: 3D Weak Lensing (Heavens, 2003). Taking advantage of the full photometric distance information in analyses of the cosmic shear field, this technique is expected to considerably improve constraints on cosmological parameters and the growth of perturbations (Heavens, 2003; Castro et al., 2005; Kitching et al., 2011). Concerning GNQ, for instance, this offers a promising way to detect signatures of large–scale neutrino clustering (suggested by the study of linear perturbations, cf. Sec. 3.3.1). The neutrino–induced gravitational potential should amplify gravitational lensing and leave an imprint in cosmic shear spectra. Later, in Chapter 6, we will confirm a significant growth of the large–scale gravitational potential during the stage of neutrino structure formation. But even in uncoupled models, an enhanced amplitude of the potentials on cosmic scales could be traced back to the dynamical nature of dark energy: In models with a dark energy sound speed below unity, e. g. within the class of k–essence (Armendariz-Picon et al., 2000), dark energy itself clusters on subhorizon scales and contributes to the right–hand side of the Poisson equation (3.29). Observations of the large–scale gravitational potentials therefore provide an exciting window on the dynamics of dark energy.

The numerical tools we develop in Sec. 4.3 are not designed for a specific model, but allow to compute cosmic shear spectra for any prediction or parameterization of the large–scale gravitational potential $\Phi(z, k)$. This is not yet fully available for GNQ. Here, we apply our methods to a simple parameterization of clustering dark energy (Sec. 4.4). This allows us to forecast the expected uncertainty in the dark energy sound speed c_s^2 for a combination of Euclid (see, e. g., Amendola et al., 2012) and Planck (see, e. g., Ade et al., 2011) data. The sound speed is particularly difficult to constrain since the signal of clustering dark energy is heavily suppressed for a dark energy equation of state w in the vicinity of -1 (cf. Sec. 4.4.1). We will see that it may become possible to determine at least its order of magnitude.

The work presented in Secs. 4.2 – 4.4 has been published (Ayaita et al., 2012a). Our presentation will closely follow the structure and content of the paper. We focus, however, on the computation of the 3D shear spectrum. Optimizations concerning the Fisher matrix analysis are not part of this work.

We will now start with a brief consideration of photon propagation in the perturbed FLRW spacetime (Sec. 4.1), which forms the basis for an understanding of weak lensing (WL). The integrated Sachs–Wolfe effect (ISW) will also be introduced in this context. The basics of 3D WL will then be covered in Sec. 4.2, where we will also present the Fisher matrix.

4.1 ISW and WL

The effects discussed in this section are linked to the propagation of photons through the inhomogeneous Universe, described by the perturbed metric, Eq. (3.26), which we repeat for convenience

$$\mathrm{d}s^2 = a^2 \left[-(1+2\Psi)\,\mathrm{d}\eta^2 + \left(1-2\Phi\right)\mathrm{d}\boldsymbol{x}^2\right]. \tag{4.1}$$

Introducing the photon momentum $k^\alpha = \mathrm{d}x^\alpha/\mathrm{d}\lambda$, with an affine parameter λ, the photon propagation is described by the geodesic equation

$$\frac{\mathrm{d}k^\alpha}{\mathrm{d}\lambda} + \Gamma^\alpha_{\rho\sigma}\, k^\rho k^\sigma = 0, \tag{4.2}$$

together with the null condition $k_\alpha k^\alpha = 0$. As usual, one splits k^α into a background part and a perturbation, $k^\alpha = \bar{k}^\alpha + \delta k^\alpha$. The zeroth component δk^0 corresponds to an energy shift, whereas the spatial perturbations $\delta\boldsymbol{k}$ express deflection. The calculation is presented in detail in the textbook by Amendola and Tsujikawa (2010). Here, we only quote the results. Perturbations are taken to first order.

The zeroth component of Eq. (4.2) implies

$$\left(\frac{\delta k^0}{k^0}\right)_O = \left(\frac{\delta k^0}{k^0}\right)_E - 2(\Psi_O - \Psi_E) + \int_E^O \left(\frac{\partial\Phi}{\partial\eta} + \frac{\partial\Psi}{\partial\eta}\right)\mathrm{d}\eta, \tag{4.3}$$

where O and E indicate the instants of observation and emission, respectively. Considering the photons of the CMB, E refers to the surface of last scattering (cf. Sec. 2.1.3). The energy shift δk^0 can then be related to a temperature shift δT. Intrinsic fluctuations $(\delta k^0/k^0)_E$ and the gravitational potential Ψ_E contribute to the so–called *ordinary Sachs–Wolfe effect*, which amounts to $(\delta T/\bar{T})_{\mathrm{SW}} = (1/3)\,\Psi_E$. It is typically not much affected by dark energy (assuming negligible early dark energy). This is different for the integral over the time variation of the gravitational potentials, representing the integrated Sachs–Wolfe effect (Sachs and Wolfe, 1967),

$$\left(\frac{\delta T}{\bar{T}}\right)_{\mathrm{ISW}} = \int_E^O \partial_\eta\,(\Phi+\Psi)\,\mathrm{d}\eta. \tag{4.4}$$

In a pure matter universe, $\Omega_m = 1$, the large–scale gravitational potentials are constant and the effect vanishes (at the linear level). This is no longer true in a universe containing dark energy: Accelerating expansion generally implies decaying gravitational potentials with a characteristic ISW signal. Correlating CMB temperature anisotropies with projections of the large–scale structure (provided by a combination of various datasets), Giannantonio et al. (2008) and Ho et al. (2008) detect a signal at the $\gtrsim 4\sigma$ level, which even slightly exceeds the ΛCDM expectation. Complementary studies (Granett et al., 2008b,a) associate hot and cold spots in the CMB with the most significant structures found in data of the Sloan Digital Sky Survey. They also provide evidence (above the 4σ level) of the ISW.

Let us briefly comment on the situation in GNQ. An important extra contribution

to the ISW is expected from the rapid growth of large–scale neutrino fluctuations in recent cosmological times (cf. Sec. 3.3.2). Depending on the details of the non–linear evolution, this may lead to characteristic signatures in the spectrum of CMB temperature anisotropies (Pettorino et al., 2010). Our analysis in Chapter 6 indeed reveals a significant growth of the gravitational potentials on large scales at redshifts $z \gtrsim 1$. Precise measurements of the ISW are expected to become an important probe for constraining the model.

Next, we turn to the implications of the spatial components of Eq. (4.2). Considering a radial light ray and two directions x^1 and x^2 orthogonal to the unperturbed propagation direction, one obtains (cf., e. g., Amendola and Tsujikawa, 2010)

$$\frac{\mathrm{d}^2 x^i}{\mathrm{d}r^2} = -\partial_i(\Phi + \Psi), \tag{4.5}$$

with $i = 1, 2$. This equation expresses the familiar gravitational lensing effect. For a comprehensive review of weak lensing (WL), see Bartelmann and Schneider (2001), and Bartelmann (2010). Integrating Eq. (4.5) yields a relation between the angular position of an observed image (for instance of a galaxy) $\boldsymbol{\theta}_O$ and the actual angular position of the source $\boldsymbol{\theta}_S$. In the linear approximation, the mapping $\boldsymbol{\theta}_O \mapsto \boldsymbol{\theta}_S$ is described by the matrix

$$\mathcal{A} = \begin{pmatrix} 1-\kappa-\gamma_1 & -\gamma_2 \\ -\gamma_2 & 1-\kappa+\gamma_1 \end{pmatrix}, \tag{4.6}$$

defining the convergence κ and the shear (γ_1, γ_2). While the convergence determines the magnification of an image, the shear determines its distortion. The convergence field and the shear field share the same statistics (identical power spectra). From an observer's perspective, however, image distortions caused by weak lensing can be detected much easier than the convergences (Bartelmann, 2010).

Convergence and shear can be calculated from second derivatives of the *lensing potential* ϕ, e. g.,

$$\kappa = \frac{1}{2}\Delta_{\vartheta,\varphi}\phi, \tag{4.7}$$

where ϕ is defined as the line–of–sight projection of the gravitational potentials. In a flat universe,

$$\phi(\boldsymbol{\theta}, r) = \int_0^r \mathrm{d}r' \, \frac{r-r'}{rr'}(\Psi(\boldsymbol{r}') + \Phi(\boldsymbol{r}')). \tag{4.8}$$

In the standard approach, an averaging over the redshift range of the sources is performed resulting in two–dimensional fields $\tilde{\kappa}(\boldsymbol{\theta})$ etc. These fields represent a direct probe of the integrated gravitational potentials Ψ and Φ, which in turn are sourced by the density perturbations in the Universe. Hence, WL can be used as a probe of the total matter power spectrum without relying on galaxy bias models (Jain and Seljak, 1997; Hu and White, 2001).

Most of the more recent studies usually divide their data set in bins according to the redshifts of the source galaxies instead of averaging over the whole range of redshifts. This approach, lensing tomography, is known to increase the sensitivity

for constraining specific cosmological parameters (Hu, 2002a). In particular, tomographic measurements considerably improve constraints on the properties of dark energy, i. e. mainly its equation of state w (Huterer, 2002; Jain and Taylor, 2003; Heavens, 2003; Bernstein and Jain, 2004; Takada and Jain, 2004; Hannestad et al., 2006; Heavens et al., 2006; Amendola et al., 2008; Hollenstein et al., 2009; Kilbinger et al., 2009; Huterer, 2010). The possibility of further reducing statistical errors by taking into account the full 3D information provided by the individual source redshifts was first explored by Heavens (2003). The relationship between the two methods has been studied by Kitching et al. (2011). The loss of information due to the averaging over redshift bins for tomography generally leads to larger statistical errors as in a full 3D analysis. For an investigation of the redshift dependence of the signal, tomography can nonetheless add valuable information.

4.2 3D weak lensing

In this section, we follow Heavens (2003) and quote an appropriate estimator for a weak lensing galaxy survey containing full information on the photometric source redshifts. Based on this estimator, the 3D WL Fisher matrix will be constructed used to forecast constraints on cosmological parameters.

As already mentioned, the statistics of the convergence field κ can hardly be observed directly; the shear field (γ_1, γ_2) is usually measured instead. Since, however, the statistics of convergence and shear are identical, we can restrict ourselves to a consideration of κ.

In a 3D analysis, we do not perform any line–of–sight averaging of the lensing potential and, thus, retain the source distance information $\phi = \phi(\vartheta, \varphi, r)$ as in Eq. (4.8). The convergence field consequently is a three–dimensional field $\kappa(\vartheta, \varphi, r)$. Heavens (2003) proposed a combined Fourier and spherical transform,

$$\kappa_{\ell m}(k) = \sqrt{\frac{2}{\pi}} \int r^2 \mathrm{d}r \, \mathrm{d}\Omega \, \kappa(\vartheta, \varphi, r) \, j_\ell(k\, r) \, Y^*_{\ell m}(\vartheta, \varphi), \tag{4.9}$$

relating the comoving distance r to a wavenumber k, and the angular position (ϑ, φ) to multipoles (ℓ, m). In this representation, Eq. (4.7) becomes

$$\kappa_{\ell m}(k) = -\frac{\ell(\ell+1)}{2} \, \phi_{\ell m}(k), \tag{4.10}$$

according to the well known property of the spherical harmonics. Further, we may use Eq. (4.8) to relate the convergence to the gravitational potentials. Let us assume for simplicity that anisotropic stress is negligible (at least on the scales of interest) and use $\Phi = \Psi$. It is also convenient to introduce the growth factor $g(k, a)$ expressing the (generally scale dependent) growth of the gravitational potential as

$$\Phi(k, a) = g(k, a) \, \Phi^0(k)/a. \tag{4.11}$$

The normalization with a factor of a^{-1} is motivated by the case of a matter dominated universe, in which the Poisson equation gives $-k^2\Phi = \frac{1}{2} a^2 \bar{\rho}_m \delta_m = \frac{1}{2} \bar{\rho}^0_m \delta_m / a$.

Hence, in this case, the function $g(k,a)$ just describes the growth of the matter density contrast, $\delta_m(k,a) = g(k,a)\delta_m^0(k)$. This is of course no longer correct in the general case.

The central relation between the lensing potential and the gravitational potential can now be written as

$$\phi_{\ell m}(k) = \eta_\ell(k,k')\,\Phi^0_{\ell m}(k'), \tag{4.12}$$

where we have, following Heavens (2003), introduced the quantity

$$\eta_\ell(k,k') = \frac{4}{\pi}\int_0^\infty r^2 \mathrm{d}r\, j_\ell(k\,r)\int_0^r \mathrm{d}r'\,\frac{r-r'}{r\,r'}\,j_\ell(k'r')\,\frac{g(k',a')}{a'} \tag{4.13}$$

and made use of the summation convention

$$A(k,k')\,B(k',k'') \equiv \int_0^\infty k'^2 \mathrm{d}k'\,A(k,k')\,B(k',k''). \tag{4.14}$$

4.2.1 Estimator

Let us now consider a survey containing a sample of galaxies $\{g\}$ with convergences $\{\kappa_g\}$. The estimator for the convergence spectrum $\hat{\kappa}_{\ell m}$ is defined as the discrete transform,

$$\hat{\kappa}_{\ell m}(k) = \sqrt{\frac{2}{\pi}}\sum_{\text{galaxies }g}\kappa_g\,j_\ell(k\,r_g)\,Y^*_{\ell m}(\vartheta_g,\varphi_g). \tag{4.15}$$

Only in an idealized situation, the estimator $\hat{\kappa}_{\ell m}(k)$ is identical to the actual convergence $\kappa_{\ell m}(k)$. The main differences occur due to uncertainties of redshift measurements and the discrete distribution of galaxies (Heavens, 2003).

Redshift errors are in the simplest case described by a Gaussian distribution with a standard deviation σ_z equal for all galaxies,

$$p(r'|r)\,\mathrm{d}r' = \frac{1}{\sqrt{2\pi}\sigma_z}\exp\left[-\frac{(z-z')^2}{2\sigma_z^2}\right]\mathrm{d}z', \tag{4.16}$$

with a typical figure $\sigma_z = 0.02$. For an extension of the method allowing for individual redshift errors, see Kitching et al. (2011).

The survey's galaxy distribution is encoded in the number density $n(\boldsymbol{r}) \equiv n(r)$ assumed rotationally symmetric. It constitutes a statistical weight favoring distances r (or, equivalently, redshifts z) where the density of galaxies is higher. We will employ a common parameterization,

$$n(z)\,\mathrm{d}z \propto z^2\exp\left[-\left(\frac{z}{z_0}\right)^\beta\right]\mathrm{d}z. \tag{4.17}$$

For our applications, we will assume 100 galaxies per square arcminute, $z_0 = 0.64$, and $\beta = 3/2$, yielding a median redshift of $z_{\text{med}} = 0.9$ (Amara and Réfrégier, 2007). For convenience, we consider the idealised case of full sky coverage, $f_{\text{sky}} = 1$ (see Heavens, 2003, for the general equations). Concerning the Fisher matrix analysis,

the estimated errors can approximately be scaled by $f_{\rm sky}^{-1/2}$ for a realistic fraction $f_{\rm sky} < 1$.

Taking these two sources of uncertainties into account, the expectation value of $\hat{\kappa}_{\ell m}$ follows as

$$\bar{\kappa}_{\ell m}(k) = Z_\ell(k,k')\, M_\ell(k',k'')\, \kappa_{\ell m}(k''), \tag{4.18}$$

where the summation convention, Eq. (4.14), is understood and we have defined the quantities

$$Z_\ell(k,k') = \frac{2}{\pi}\int r'^2 {\rm d}r' \int {\rm d}r\, p(r'|r)\, j_\ell(k'r)\, j_\ell(k\,r'), \tag{4.19}$$

$$M_\ell(k,k') = \frac{2}{\pi}\int r^2 {\rm d}r\, j_\ell(k\,r)\, j_\ell(k'r)\, n(r), \tag{4.20}$$

Instead of directly measuring the convergence (or shear) field, observations infer its power spectrum,

$$S_{\ell\ell' mm'}(k,k') = \langle \bar{\kappa}_{\ell m}(k) \bar{\kappa}^*_{\ell' m'}(k')\rangle. \tag{4.21}$$

The Cosmological Principle states that the large–scale averages of the shear and convergence fields vanish; the two–point functions or power spectra are however definite predictions of perturbation theory within a specific model. Collecting Eqs. (4.10), (4.12), and (4.18), we arrive at

$$S_{\ell\ell' mm'}(k,k') = A^2\, B_\ell(k,k'')\, P^0_\Phi(k'')\, B_\ell(k',k'')\, \delta_{\ell\ell'}\delta_{mm'}, \tag{4.22}$$

with $A = \ell(\ell+1)/2$ and the convenient abbreviation

$$B_\ell(k,k') = Z_\ell(k,k'')\, M_\ell(k'',k''')\, \eta_\ell(k''',k'). \tag{4.23}$$

Note, that the Kronecker deltas $\delta_{\ell\ell'}$ and $\delta_{mm'}$ are a consequence of the assumed full–sky coverage and we have replaced the spectrum of $\Phi_{\ell,m}(k)$ by the common spectrum $P_\Phi(k)$ based on the three–dimensional Fourier transform (cf., Heavens, 2003),

$$\langle \Phi(z,\boldsymbol{k})\, \Phi^*(z,\boldsymbol{k}')\rangle = (2\pi)^3\, P_\Phi(z,k)\, \delta^3_D(\boldsymbol{k}-\boldsymbol{k}'). \tag{4.24}$$

Equation (4.22) describes the 3D WL signal. Cosmological information is encoded in the dependence of $S_{\ell\ell' mm'}(k,k')$ on the parameters. But the full covariance also contains a shot noise part due to discrete galaxy sampling,

$$N_{\ell\ell' mm'}(k,k') = \frac{\sigma_e^2}{4} M_\ell(k,k')\, \delta_{\ell\ell'}\delta_{mm'}, \tag{4.25}$$

with $\sigma_e^2 \sim 0.1$ (Heavens, 2003). In principle, the correlation between the ellipticities of neighbouring galaxies due to intrinsic alignments (Heavens et al., 2000; Schäfer, 2009) contributes an additional source of noise. This effect can however be neglected for large–scale studies. For a discussion of systematic effects in 3D WL and tomography, we refer to March et al. (2011); Takada and Jain (2009); Kitching et al. (2008), and Huterer et al. (2006). For our purposes, we stick to the noise

term in Eq. (4.25). The covariance matrix is then defined as

$$C_{\ell\ell' mm'}(k,k') = S_{\ell\ell' mm'}(k,k') + N_{\ell\ell' mm'}(k,k'). \tag{4.26}$$

In order to keep notation simpler, we usually write $S_\ell(k,k')$, $N_\ell(k,k')$, and $C_\ell(k,k')$, where $S_{\ell\ell' mm'}(k,k') = S_\ell(k,k')\delta_{\ell\ell'}\delta_{mm'}$ etc.

4.2.2 Fisher matrix

The Fisher matrix analysis is a standard method for forecasting how well future experiments can constrain cosmological parameters. In Sec. 4.4, we will explore the possibility of constraining the dark energy speed of sound c_s^2 with a combination of data from Euclid and Planck. For a general introduction to the formalism, see Tegmark et al. (1997) or Amendola and Tsujikawa (2010).

As a starting point, we consider the likelihood $L = L(\hat{\kappa}_{\ell m}(k)|\boldsymbol{p})$ describing the probability of observing convergences $\hat{\kappa}_{\ell m}(k)$ given cosmological parameters $\boldsymbol{p}$. For given data, we could ask for the so–called *maximum likelihood parameters* $\hat{\boldsymbol{p}}$ that maximize the likelihood L. Expanding $\ln L$ around $\hat{\boldsymbol{p}}$, yields

$$\ln L(\boldsymbol{p}) \approx \ln L(\hat{\boldsymbol{p}}) + \frac{1}{2}\left.\frac{\partial^2 \ln L}{\partial p_i \partial p_j}\right|_{\boldsymbol{p}=\hat{\boldsymbol{p}}} (p_i - \hat{p}_i)(p_j - \hat{p}_j). \tag{4.27}$$

The likelihood (as a function of the parameters) takes the simple form of a multivariate Gaussian in this approximation:

$$L \propto \exp\left(-\frac{1}{2}(p_i - \hat{p}_i)\hat{F}_{ij}(p_j - \hat{p}_j)\right), \tag{4.28}$$

where we have defined the symmetric matrix

$$\hat{F}_{ij} = -\left.\frac{\partial^2 \ln L}{\partial p_i \partial p_j}\right|_{\boldsymbol{p}=\hat{\boldsymbol{p}}}. \tag{4.29}$$

Indices i, j run over the number of cosmological parameters in this section.

Clearly, when analyzing a future experiment, the maximum likelihood parameters $\hat{\boldsymbol{p}}$ are not known. Instead, one may assume that they are represented by some *fiducial* cosmology and ask for the resulting confidence regions around these values. This is the basic idea of the Fisher matrix analysis. The general definition of the *Fisher matrix* is given by

$$F_{ij} = \left\langle -\frac{\partial^2 \ln L}{\partial p_i \partial p_j} \right\rangle, \tag{4.30}$$

where angular brackets, in this context, indicate averaging over the data distribution ($L(\boldsymbol{x}|\boldsymbol{p})\,\mathrm{d}\boldsymbol{x}$). Within the approximation (4.27), F_{ij} coincides with $\hat{F}_{ij}$ (cf., e. g., Amendola and Tsujikawa 2010) and thus fully describes the likelihood (4.28) in the vicinity of the chosen fiducial values. Moreover, the Fisher matrix provides stringent lower bounds on the individual uncertainties Δp_i of the form

$$\Delta p_i \geq \sqrt{(F^{-1})_{ii}}. \tag{4.31}$$

This bound is known as the Cramér–Rao inequality.

Based on the considerations of the previous section, we can now construct the 3D WL Fisher matrix. Following Heavens (2003), we take the likelihood as a multivariate Gaussian in the data with the covariance matrix C specified in Eq. (4.26). A straightforward computation (cf., Tegmark et al., 1997) then yields

$$F_{ij} = \frac{1}{2}\mathrm{tr}\left[C^{-1}(\partial_i C)C^{-1}(\partial_j C)\right], \tag{4.32}$$

with "tr" indicating the trace over the indices $(\ell, \ell', m, m', k, k')$. In our case, the summation over m is trivial (cf. Eqs. 4.22 and 4.25), leading to a simplified expression,

$$F_{ij} = \sum_{\ell}^{\ell_{\max}} \frac{2\ell+1}{2}\mathrm{tr}\left[C_\ell^{-1}(\partial_i C_\ell)C_\ell^{-1}(\partial_j C_\ell)\right], \tag{4.33}$$

with "tr" now denoting the trace over Fourier modes k.

At the end of this section, let us point out that the Fisher matrix has some nice and useful properties, which are listed and explained in detail in the textbook by Amendola and Tsujikawa (2010). We briefly summarize those features which will be of relevance in this work:

1. If one fixes a specific parameter p_i to its fiducial value $\hat{p}_i$, the rows and columns related to this parameter are simply removed from the Fisher matrix.

2. Marginalizing over a parameter p_i (i. e., integrating out its probability distribution) is equivalent to removing from the inverse Fisher matrix F^{-1} the row and column associated with the particular parameter.

3. Independent data sets can be combined by adding the corresponding Fisher matrices.

4.3 Numerical strategy

In the previous section, we have introduced the 3D WL estimator $\hat{\kappa}_{\ell m}(k)$ and the covariance matrix $C_\ell(k, k')$ representing its statistics. Further, we have seen that the Fisher matrix F_{ij} can directly be computed from the covariance according to Eq. (4.33). By closer inspection, the computation of the signal part $S_\ell(k, k')$, Eq. (4.22), contains multiple nested integrals involving oscillating functions (cf. Eqs. 4.13, 4.19, 4.20). In this section, we derive adequate strategies to tackle these numerical difficulties.

4.3.1 The matrix $B_\ell(k, k')$

The main ingredient of the signal part $S_\ell(k, k')$ is the projection $B_\ell(k, k')P^0_\Phi(k')$, with the previously defined quantity $B_\ell(k, k')$ (see Eq. 4.23). In principle, the quantities Z_ℓ, M_ℓ and η_ℓ could be computed independently from one another. Then, in a second step, they would need to be combined to obtain B_ℓ. This procedure would require a total number of seven nested integrals, each introducing

new numerical inaccuracies. In this section, we propose an alternative procedure for the calculation of B_ℓ. Our approach requires no preparation of the individual quantities Z_ℓ, M_ℓ, and η_ℓ. The additional (unproblematic) computation of M_ℓ is then only required for the noise part, Eq. (4.25). The great advantage of this approach is that we can reduce the number of necessary numerical integrations by exploiting the orthogonality relation of spherical Bessel functions,

$$\int_0^\infty k^2 \mathrm{d}k\, j_\ell(k\,r)\, j_\ell(k\,r') = \frac{\pi}{2r^2}\delta_D(r-r'). \tag{4.34}$$

For instance, let us consider the product $Z_\ell(k,q)M_\ell(q,k')$ in detail:

$$\begin{aligned}
&Z_\ell(k,q)M_\ell(q,k') = \\
&= \frac{4}{\pi^2}\int q^2\mathrm{d}q \int r'^2\mathrm{d}r' \int \mathrm{d}r\, p(r'|r) j_\ell(q\,r) j_\ell(k\,r') \int s^2\mathrm{d}s\, j_\ell(q\,s) j_\ell(k's) n(s) \\
&= \frac{4}{\pi^2}\int r'^2\mathrm{d}r' \int \mathrm{d}r \int s^2\mathrm{d}s\, p(r'|r) j_\ell(k\,r') j_\ell(k's) n(s) \int q^2\mathrm{d}q\, j_\ell(q\,r) j_\ell(q\,s) \\
&= \frac{2}{\pi}\int r'^2\mathrm{d}r' \int \mathrm{d}r\, p(r'|r) j_\ell(k\,r') j_\ell(k'r) n(r).
\end{aligned} \tag{4.35}$$

In the first line, we have inserted the definitions, Eqs. (4.19) and (4.20) and the convention Eq. (4.14). After appropriate rearranging of the integrals (second line), we have identified the integral over q with the orthogonality relation (4.34) and made use of the delta function to solve the integral over s. We have already reduced the number of integrations by two. In a similar way, we can simplify the multiplication with η_ℓ and finally end up with

$$B_\ell(k,k') = \frac{4}{\pi}\int r'^2\mathrm{d}r'\, j_\ell(k\,r') \int \mathrm{d}r\, p(r'|r)\, n(r)\, f_\ell(k',r), \tag{4.36}$$

where we have defined

$$f_\ell(k,r) = \int_0^r \mathrm{d}r'\, j_\ell(k\,r')\, \frac{r-r'}{r\,r'}\frac{g(k,a')}{a'}. \tag{4.37}$$

We will now explain how to efficiently evaluate the inner integral in Eq. (4.36). The algorithm is based on a discrete Fourier transform (DFT), for which fast methods exist. In a first step, we need to sample the function f_ℓ for a given k at discrete values $\{r_j\}$, $j = 1,\ldots,N$. For this, it is not necessary to calculate the full integral (4.37) for each r_j. Instead, one can decompose $f_\ell(k,r)$ into two integrals whose integrands are independent of r,

$$f_\ell(k,r) = \int_0^r \frac{\mathrm{d}r'}{r'}\, j_\ell(k\,r')\frac{g(k,a')}{a'} - \frac{1}{r}\int_0^r \mathrm{d}r'\, j_\ell(k\,r')\frac{g(k,a')}{a'}. \tag{4.38}$$

The values $f_\ell(k,r_j)$ can then be obtained successively by computing the integrals from r_{j-1} to $r_j > r_{j-1}$ and reusing the result of the previous calculation.

Further, we assume that the conditional distribution $p(z|z')$, describing the uncertainties of redshift measurements, only depends on $(z'-z)$. This is true for

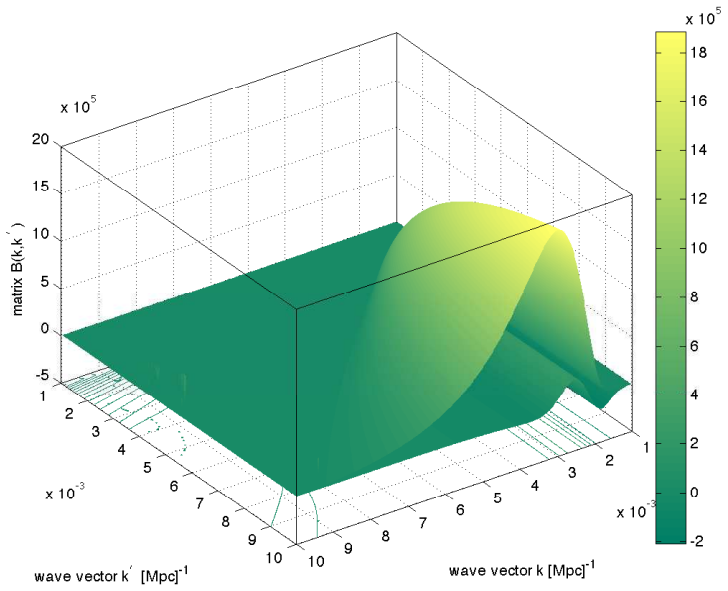

Figure 4.1: The quantity $B_\ell(k,k') = Z_\ell(k,k'')\,M_\ell(k'',k''')\,\eta_\ell(k''',k')$ for $\ell = 10$ (upper surface) obtained by the method described in the text. We have also included the difference between the full integration and the Limber approximation. The error amounts to $\lesssim 10\%$ of the amplitude.

the Gaussian assumed in Eq. (4.16). It allows us to express the inner integral in Eq. (4.36) as a convolution in redshift space,

$$\int_0^\infty \mathrm{d}r\, p(r'|r)\, n(r)\, f_\ell(k',r) = \frac{\mathrm{d}z'}{\mathrm{d}r'} \int_0^\infty \mathrm{d}z\, p(z'-z) \left(\frac{\mathrm{d}r}{\mathrm{d}z}\, n(r(z))\, f_\ell(k',z) \right) . \quad (4.39)$$

The convolution integral can be efficiently solved by virtue of the Fourier transform. This is due to the fact, that a convolution in real space refers to a simple multiplication in Fourier space and vice versa. The Fourier transform of a Gaussian is again a Gaussian and hence analytically known. The Fourier coefficients of the second factor are obtained by virtue of a fast Fourier transform (FFT) routine (e. g. Frigo and Johnson, 2005); therefor, the sampled values of f_ℓ are needed. For completeness, $\mathrm{d}r/\mathrm{d}z = H^{-1}(z)$ in a flat FLRW universe.

The steps outlined above allow for a fast and accurate computation of the quantity $B_\ell(k,k')$ and thereby of the covariance $C_\ell(k,k')$. For the purpose of a Fisher matrix analysis, further numerical optimization is possible. Since the Fisher matrix F_{ij} is given in terms of a trace (cf. Eq. 4.33), one has the freedom to change the basis in which the covariance matrix is represented. We point out, that it is possible to circumvent the remaining r'–integration in Eq. (4.36) by a suitable transformation (Ayaita et al., 2012a). These operations are however not part of this thesis. Applying $B_\ell(k,k')$ to the present spectrum of the gravitational potential according to Eq. (4.22) eventually yields the signal part of the covariance matrix $C_\ell(k,k')$.

We note that the computation of $B_\ell(k,k')$ is also specifically simple within the

so–called Limber approximation (see, e. g., Kitching et al., 2011). For large ℓ, the spherical Bessel functions j_ℓ can be approximated by Dirac delta functions; most of the necessary integrations can then be performed analytically (see Ayaita et al., 2012a for details). The results for small ℓ are, however, affected by inaccuracies, which do not allow for a precise calculation of the covariance. For the investigation of large–scale phenomena (such as dark energy clustering, see Sec. 4.4), the Limber approximation generally is not recommendable and we advocate the more appropriate method described above.

For illustration, we plot the numerical results for $B_\ell(k, k')$ in Fig. 4.1 for $\ell = 10$. The figure also shows the difference between the full integration and the Limber approximation.

4.3.2 Computation of the Fisher matrix

From the covariance matrix to the Fisher matrix, the following steps have to be taken (cf. Eq. 4.33):

1. Computation of the derivatives $\partial_i C_\ell(k, k')$.
   For each parameter p_i, we evaluate the covariance matrix for slightly varied values $p_i = \hat{p}_i \pm \varepsilon_i$ around the fiducial value $\hat{p}_i$ (while keeping the other parameters fixed; $p_j = \hat{p}_j$, for $i \neq j$). We typically choose $\varepsilon_i = 0.05\,\hat{p}_i$. The derivative $\partial_i C_\ell(k, k')$ is then estimated with the difference quotient,

$$\partial_i C_\ell(k, k') \approx \frac{C_\ell(k, k'; \hat{p}_i + \varepsilon_i) - C_\ell(k, k'; \hat{p}_i - \varepsilon_i)}{2\varepsilon_i}. \tag{4.40}$$

2. Multiplication with the inverse $C_\ell^{-1}(k, k')$.
   Equation (4.33) involves matrix products $C_\ell^{-1}\,\partial_i C_\ell$. Instead of explicitly calculating the inverse matrix C_ℓ^{-1}, we solve the linear system

$$C_\ell(k, k')\, X_\ell^{(i)}(k', k'') = \partial_i C_\ell(k, k''), \tag{4.41}$$

   by virtue of a standard LU–decomposition of C_ℓ (for this purpose, we employ facilities of the GNU Scientific Library, cf. Galassi et al., 2009).

3. Final matrix product and summation.
   For calculating the trace, we only need the diagonal elements of the matrix product $X_\ell^{(i)} X_\ell^{(j)}$, with $X_\ell^{(i)} = C_\ell^{-1}\,\partial_i C_\ell$ as above. The Fisher matrix then follows as

$$F_{ij} = \sum_{\ell,k,k'} \frac{2\ell + 1}{2}\, X_\ell^{(i)}(k, k')\, X_\ell^{(j)}(k', k). \tag{4.42}$$

4.4 Application to clustering dark energy

In the previous sections, we have reviewed the theory of 3D WL and developed adequate numerical tools for a quantitative analysis. In the following, we will representatively study clustering dark energy as a scenario including a modified growth

of perturbations on large scales. The decisive quantity is the dark energy speed of sound c_s introducing a new characteristic scale for the evolution of perturbations, the sound horizon. Constraining both, the dark energy equation of state w and its sound speed c_s, can help to distinguish between competing dark energy candidates (Hu, 2002b; Erickson et al., 2002; DeDeo et al., 2003; Hu and Scranton, 2004). Unfortunately, current observational data has not yet provided significant constraints on c_s (cf., e. g., Bean and Dore, 2004; de Putter et al., 2010; Li and Xia, 2010).

The signature of a clustering dark energy component is an enhanced gravitational potential on large scales. This is partly due to the presence of large–scale dark energy perturbations and partly due to the "dragging effect" on matter perturbations (we will discuss these effects in more detail in Sec. 4.4.1). As discussed in Sec. 4.1, the standard WL spectrum provides only an integral measure of the gravitational potentials. Due to the averaging procedure, the signal coming from large scales is hardly visible in the spectrum. This serves as the motivation for employing the 3D method presented in Sec. 4.2. The Fisher matrix analysis in Sec. 4.4.3 will concentrate on the properties of dark energy. We will present and discuss constraints expected from a combination of Euclid (Amendola et al., 2012) and Planck (Ade et al., 2011) data.

4.4.1 The dark energy speed of sound c_s

Neglecting possible direct couplings to other species in the Universe, the influence of dark energy on the evolution of the cosmic background and the dynamics of linear perturbations is restricted to gravity. The role of the equation of state, $w = \bar{P}/\bar{\rho}$, has already been discussed in previous chapters. Here, we introduce the (squared) speed of sound, $c_s^2 = \delta P/\delta\rho$, as a characteristic parameter on the level of linear perturbations. The sound speed is only well defined after specifying a gauge (cf. Sec. 3.3.1). In our notation, c_s^2 always refers to the rest–frame speed of sound, computed in a frame where the velocity perturbation of the fluid vanishes, $v = 0$. For a brief introduction to dark energy clustering, see, e. g., Gordon and Hu (2004).

Typically, the sound speed defines a characteristic scale $\lambda_{\text{eff}} \propto |c_s|/\mathcal{H}$, below which gravitational clustering is prevented. Dark energy density perturbations δ_{DE} are thus primarily expected on scales above λ_{eff}. In consequence, one may hope to observe traces of a clustering dark energy component if λ_{eff} lies within the horizon, $\lambda_{\text{eff}} < \mathcal{H}^{-1}$.

A more accurate consideration of the perturbation equations (cf., e. g., Ayaita et al., 2012a) shows that the clustering properties of dark energy are also sensitive to the equation of state w. For the observationally preferred value $w \approx -1$, only very small values $c_s^2 < 1 + w$ may lead to a significant growth of dark energy perturbations on sub–horizon scales. We will come back to this point when we have introduced our parameterization of dark energy.

The sound speed of scalar field dark energy

If dark energy is represented by a cosmological constant, it is perfectly homogeneous by definition. Alternatively, we have considered a canonical scalar field φ as a form of dynamical dark energy (cf. Sec. 2.2.2). Introducing a perturbation $\varphi = \bar{\varphi} + \delta\varphi$,

we may derive the linear perturbations of the energy–momentum tensor, Eq. (2.43). The density and pressure perturbations are found to be

$$\delta\rho_\varphi = \dot{\bar{\varphi}}\,\delta\dot{\varphi} + V_{,\varphi}(\bar{\varphi})\delta\varphi, \tag{4.43}$$
$$\delta P_\varphi = \dot{\bar{\varphi}}\,\delta\dot{\varphi} - V_{,\varphi}(\bar{\varphi})\delta\varphi. \tag{4.44}$$

The velocity perturbation v_i can be read off (cf. Eq. 3.27) from

$$T^0{}_i = -\dot{\bar{\varphi}}\,\partial_i\delta\varphi, \tag{4.45}$$

which implies $v \propto \delta\varphi$ for the scalar velocity perturbation v. In the rest frame ($v = \delta\varphi = 0$), we find $c_s^2 = \delta P/\delta\rho = 1$. Dark energy clustering does not occur on sub–horizon scales. This is a well known result for standard quintessence.

Clearly, the situation is very different in models of coupled quintessence, where the dynamics of the perturbations are no longer described by gravity alone. In GNQ, for instance, scalar field perturbations mainly grow due to the interaction with neutrinos. While it is still possible to define a sound speed parameter for the coupled fluid of quintessence and the specific matter component, the quantity is not of the same importance anymore. Other parameters have to be taken into account (e. g., the coupling parameters) and need to be constrained. Weak lensing constraints for models with a coupling between dark energy and dark matter have been studied in the literature (Schäfer et al., 2008; La Vacca and Colombo, 2008; Caldera-Cabral et al., 2009; De Bernardis et al., 2011).

Another prominent class of scalar field models, k–essence (Armendariz-Picon et al., 2000, 2001), assumes non–standard kinetic terms. Thereby, it is possible to obtain arbitrary values of the sound speed c_s^2 (for a discussion of causality, see Babichev et al., 2008). Similar to w, the parameter generally varies in time, which can give rise to characteristic signatures (Ansari and Unnikrishnan, 2011). Promising 3D WL constraints have already been forecasted for a specific model within this class (Camera et al., 2010).

The wCDM+c_s^2 parameterization

The previous considerations suggest that a measurement of the sound speed parameter c_s^2 may provide a means to distinguish between models of dark energy. In principle, dynamical dark energy needs to be described by generic functions $w(z)$ and $c_s^2(z)$. For many purposes, however, simple parameterizations are used. Here, we will adopt a generalization of the wCDM parameterization (Turner and White, 1997) including the sound speed c_s^2 as a free parameter. The equation of state and the rest–frame speed of sound are assumed constant. Obviously, this simple parameterization can, by far, not represent the large class of dynamical dark energy models. Instead, we consider the parameterization as a practical tool to measure how sensitive future experiments are to deviations from the ΛCDM prediction. Still, each specific model of dark energy needs to be confronted with the actual data in order to constrain its parameters.

The clustering dark energy component appears as an extra term on the right–

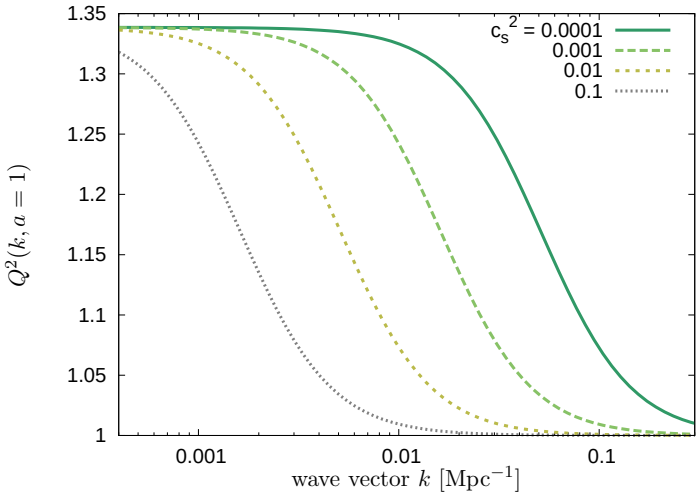

Figure 4.2: The scale dependence of Q^2 for varying c_s^2 and a fixed equation of state $w = -0.8$ at $a = 1$. Dark energy perturbations are generally only present at large scales.

hand side of the Poisson equation (3.29):

$$\begin{aligned} k^2\Phi &= -\frac{1}{2}a^2\left(\bar{\rho}_m\delta_m + \bar{\rho}_{\rm DE}\delta_{\rm DE}\right) \\ &= -\frac{1}{2}a^2\,Q\,\bar{\rho}_m\delta_m, \end{aligned} \tag{4.46}$$

where we have introduced the quantity $Q = Q(k, a)$,

$$Q = 1 + \frac{\bar{\rho}_{\rm DE}\,\delta_{\rm DE}}{\bar{\rho}_m\,\delta_m}. \tag{4.47}$$

Note, that on sub–horizon scales the density contrasts δ_i in the conformal Newtonian gauge coincide with the gauge–invariant quantities Δ_i used in the paper (Ayaita et al., 2012a). We adopt a suitable parameterization of Q for constant dark energy parameters w and c_s^2 (Sapone et al., 2010),

$$Q \approx 1 + \frac{1-\Omega_m^0}{\Omega_m^0}\frac{(1+w)\,a^{-3w}}{1-3w+y^2}, \quad y^2 \equiv \frac{2}{3}\frac{k^2c_s^2a}{\Omega_m^0\mathcal{H}_0^2}. \tag{4.48}$$

For illustration, we plot the function $Q^2(k, a = 1)$ for $w = -0.8$ and various values of c_s^2 in Fig. 4.2 (the squared value of Q is relevant for the spectrum P_Φ). The separation of scales is clearly visible. For each value of c_s^2, we can find a typical scale $\lambda_{\rm eff} = 1/k_{\rm eff}$ below which dark energy is still homogeneous, $Q^2 \approx 1$, whereas perturbations are present on larger scales. More quantitatively, let us define the scale $\lambda_{\rm eff}$ by requiring $Q(k, a = 1) \gtrsim 1 + \varepsilon$ for $\lambda > \lambda_{\rm eff}$ and a small number ε.

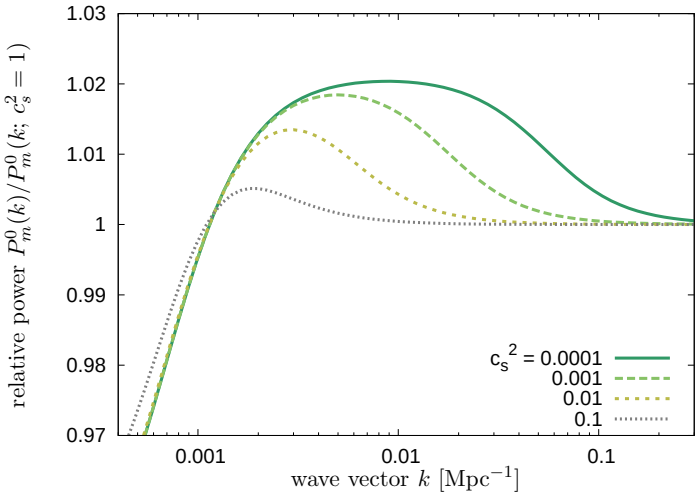

Figure 4.3: The present matter power spectrum $P_m^0(k)$ for $w = -0.8$ and varying dark energy speed of sound c_s^2 divided by the spectrum for $c_s^2 = 1$. (The spectrum is computed from the gauge–invariant density contrast Δ_m, which is identical to δ_m in the conformal Newtonian gauge on sub–horizon scales.)

Choosing $\Omega_m^0 \approx 0.3$ and $\varepsilon \approx 1\%$, we find

$$\lambda_{\text{eff}} \approx 0.1 \, \frac{|c_s|}{\sqrt{1+w}} \mathcal{H}_0{}^{-1}. \tag{4.49}$$

One may hope to detect dark energy clustering if λ_{eff} lies well within the horizon, $\lambda_{\text{eff}} \ll \mathcal{H}_0^{-1}$, i. e. $c_s^2 < (1+w)$. For the critical value $w = -1$, we have $\lambda_{\text{eff}} \to \infty$. In this case, $Q(k,a) = 1$ on all scales and the dark energy sound speed c_s^2 becomes meaningless.

The factor $Q(k,a)$ in Eq. (4.46) takes into account the direct contribution of dark energy perturbations to the gravitational potential. In addition, during the course of their evolution, matter perturbations feel an enhanced gravitational potential due to the presence of clustering dark energy. This "dragging effect" modifies large–scale matter perturbations. We use CAMB (Lewis et al., 2000) to illustrate the effect. The code integrates the linear perturbation equations for constant dark energy parameters, w and c_s^2, and adiabatic initial conditions. We show the impact on the present matter power spectrum $P_m^0(k)$ for different choices of c_s^2 and a fixed equation of state $w = -0.8$ in Fig. 4.3. According to the numerical results, the effect is below the percent level for $c_s^2 \gtrsim 0.1$ and only affects large scales. For w closer to -1, the modifications will be even weaker.

The modified growth of matter perturbations can also be parameterized by means of the function Q. For this purpose, we introduce the growth index $\gamma(k,a)$ (Linder and Cahn, 2007),

$$\frac{\mathrm{d}\ln\delta^{(m)}}{\mathrm{d}\ln a} = \Omega_m^{\gamma}, \tag{4.50}$$

and use the approximation (cf. Sapone and Kunz, 2009; Sapone et al., 2010; Linder

and Cahn, 2007)

$$\gamma \approx \frac{3\,(1-w-A)}{5-6w}, \quad A \equiv \frac{Q-1}{1-\Omega_m}. \tag{4.51}$$

Collecting the equations above allows us to calculate the growth factor $g(k,a)$ (defined in Eq. 4.11):

$$g(k,a) = \frac{Q(k,a)}{Q^0(k)}\,\exp\left(\int_1^a \frac{\mathrm{d}a'}{a'}\,\Omega_m(a')^{\gamma(k,a')}\right), \tag{4.52}$$

with Q and γ specified in Eqs. (4.48) and (4.51).

3D weak lensing with clustering dark energy

Let us briefly point out where the effects of dark energy clustering enter the analysis presented in Sec. 4.2. The indirect and dynamical effect on the growth of matter perturbations is accounted for by using the modified growth function, Eq. (4.52), in the definition of $\eta_\ell(k,k')$, Eq. (4.13). Further, the spectrum P_Φ^0 is a crucial part of the signal covariance, Eq. (4.22). By virtue of Eq. (4.46), we find $P_\Phi^0(k) \propto k^{-4}[Q^0(k)]^2 P_m^0(k)$ with the present matter power spectrum $P_m^0(k)$. Equation (4.22) then reads

$$S_{\ell\ell' mm'}(k,k') = \tilde{A}^2\,B_\ell(k,k'')\,\frac{[Q^0(k'')]^2 P_m^0(k'')}{k''^4}\,B_\ell(k',k'')\,\delta_{\ell\ell'}\delta_{mm'}, \tag{4.53}$$

with $\tilde{A} = \frac{1}{2}\bar{\rho}_m^0\,\frac{\ell(\ell+1)}{2}$.

4.4.2 Fisher matrix analysis

Before we employ the Fisher matrix formalism (cf. Sec. 4.2.2) to estimate constraints from a 3D WL study, we need to discuss a caveat concerning constraints on c_s^2. The Fisher matrix formalism owes much of its predictive power to the Cramér–Rao inequality, $\Delta p_i \geq \sqrt{(F^{-1})_{ii}}$. We have to bear in mind, however, that these bounds are realistic estimates of the actual errors only in the case of an approximately Gaussian likelihood L (as a function of the parameters). This is always the case, if $\ln L$ can be described by a linear expansion around the fiducial cosmology (cf. Eq. 4.27). If a parameter, such as c_s^2, is only weakly constrained, we have to expect a rather "broad" likelihood instead, reaching into regions of the parameter space where the linear approximation becomes invalid. This is related to the question whether the dependence of the observed spectrum on the parameter under consideration can approximately be described at the linear level (Ballesteros and Lesgourgues, 2010). Considering Figs. 4.3 and 4.2, which give a rough impression of how the 3D WL convergence spectrum depends on the dark energy sound speed, one may conclude that the parameter $\log_{10} c_s^2$ is better suited for a Fisher matrix analysis than c_s^2 itself. Still, the Cramér–Rao bounds should only be considered as first–order estimates of the actual future constraints. As long as the constraints on c_s^2 are small, we have $\Delta c_s^2/c_s^2 \approx \ln(10)\,\Delta \log_{10} c_s^2 \approx 2.3\,\Delta \log_{10} c_s^2$.

Our model involves six parameters, $p_i \in \{\Omega_m^0, A_s, h, n_s, w, \log_{10} c_s^2\}$. We neglect the energy contribution of radiation and do not distinguish between baryons and

cold dark matter, i. e. $\Omega_m = \Omega_b + \Omega_c$. The flatness condition determines $\Omega_{DE} = 1 - \Omega_m$. This leads to a 6×6 Fisher matrix, which will be calculated according to Eq. (4.33). In addition, we will use information from observations of the CMB.

CMB Fisher matrix

The additivity of Fisher matrices from independent experiments (cf. Sec. 4.2.2) allows us to combine a WL study with observations of the CMB. The complementary information coming from the CMB will, for instance, provide tight constraints on the parameters describing the primordial spectrum, $\{A_s, n_s\}$. Here, we will adopt the expected performance of the Planck satellite and include CMB temperature (TT), polarization (EE) and cross–correlation (TE) spectra. For an introduction to the physics of CMB anisotropies, see Doran (2008).

CMB sky maps are usually expanded in spherical harmonics, e. g.,

$$\frac{\delta T}{\bar{T}}(\vartheta, \varphi) = \sum_{\ell,m} a^T_{\ell m} Y^m_\ell(\vartheta, \varphi), \tag{4.54}$$

where the coefficients $a^T_{\ell m}$ contain a signal $s^T_{\ell m}$ and a noise part $n^T_{\ell m}$, $a^T_{\ell m} = s^T_{\ell m} + n^T_{\ell m}$. The spectrum of the noise part can be modelled (cf. Knox, 1995; Perotto et al., 2006) as

$$N^{PP'}_\ell = \langle n^{P*}_{\ell m} n^{P'}_{\ell m} \rangle = \delta_{PP'} \left(\frac{\Delta_P}{\bar{T}} \right)^2 \exp\left(\ell(\ell+1) \frac{\theta^2_{\mathrm{fwhm}}}{8 \ln 2} \right), \tag{4.55}$$

where θ_{fwhm} is the full width at half maximum of the beam (assumed Gaussian), σ_P characterizes the instrumental noise, and $P \in \{T, E\}$ specifies the observable. Non–diagonal terms are assumed to vanish. Assuming full–sky observation (f_{sky} will be reinserted later) and vanishing correlation between the signal and noise part, the full covariance reads

$$\langle a^{P*}_{\ell m} a^{P'}_{\ell' m'} \rangle = \left(C^{PP'}_\ell + N^{PP'}_\ell \right) \delta_{\ell\ell'} \delta_{mm'}, \tag{4.56}$$

where the spectra $C^{PP'}_\ell$ represent the actual CMB anisotropies. For the computation of the Fisher matrix $F^{(\mathrm{CMB})}_{ij}$, we follow Perotto et al. (2006). Using the abbreviation $\tilde{C}^{PP'}_\ell = C^{PP'}_\ell + N^{PP'}_\ell$, we define the 3×3 matrix

$$A_\ell = \frac{2}{(2\ell+1) f_{\mathrm{sky}}} \times \begin{pmatrix} \left(\tilde{C}^{TT}_\ell\right)^2 & \left(\tilde{C}^{TE}_\ell\right)^2 & \tilde{C}^{TE}_\ell \, \tilde{C}^{TT}_\ell \\ \left(\tilde{C}^{TE}_\ell\right)^2 & \left(\tilde{C}^{EE}_\ell\right)^2 & \tilde{C}^{TE}_\ell \, \tilde{C}^{EE}_\ell \\ \tilde{C}^{TE}_\ell \, \tilde{C}^{TT}_\ell & \tilde{C}^{TE}_\ell \, \tilde{C}^{EE}_\ell & \frac{1}{2}\left[\left(\tilde{C}^{TE}_\ell\right)^2 + \tilde{C}^{TT}_\ell \, \tilde{C}^{EE}_\ell \right] \end{pmatrix}. \tag{4.57}$$

The Fisher matrix can then be computed according to

Beam width	$\theta_{\mathrm{fwhm}} = 7$ arcmin
Temperature noise	$\sigma_T = 28\ \mu$K arcmin
Polarization noise	$\sigma_E = 57\ \mu$K arcmin
Sky fraction	$f_{\mathrm{sky}} = 0.65$

Table 4.1: Characteristics of the Planck survey (Hollenstein et al., 2009) assumed for the calculation of the CMB Fisher matrix.

$$F_{ij}^{(\mathrm{CMB})} = \sum_{\ell=2}^{\ell_{\max}} \sum_{PP',QQ'} \partial_i C_\ell^{PP'} \left(A_\ell^{-1}\right)_{PP'QQ'} \partial_j C_\ell^{QQ'}, \tag{4.58}$$

with the indices $PP', QQ' \in \{TT, EE, TE\}$ in our case.

For each set of cosmological parameters, we employ CAMB for the computation of the theoretical spectra $C_\ell^{PP'}$. The noise part follows from Eq. (4.55). We list the assumed properties of the Planck survey according to Hollenstein et al. (2009) in Tab. 4.1. In all subsequent calculations, we include CMB multipoles up to $\ell_{\max} = 2250$. Only for the purpose of constructing the CMB Fisher matrix, we involve the baryon density parameter Ω_b^0; before $F_{ij}^{(\mathrm{CMB})}$ is added to the WL Fisher matrix, we marginalize over Ω_b^0 (cf. Sec. 4.2.2) to obtain a 6×6 matrix.

4.4.3 Results

We will now present constraints on cosmological parameters obtained from a numerical implementation (programming language: C) of the strategies discussed in Sec. 4.3. We are mainly interested in the dark energy parameters w and c_s^2. From our considerations in Sec. 4.4.1, we expect the constraints on c_s^2 to strongly depend on the chosen fiducial parameters. The critical scale above which dark energy clustering is dominant was found to be proportional to $|c_s|/\sqrt{1+w}$. In particular, if $w = -1$, the signal vanishes completely. The tightest constraints are thus expected for large values of w and small values of c_s^2. We can study this dependence quantitatively by employing the Fisher matrix analysis for varying fiducial values. For this purpose, we keep the other parameters fixed to the WMAP estimates (Komatsu et al., 2011) and consider the 2×2 Fisher matrix F_{ij}, $i, j \in \{\log_{10} c_s^2, w\}$. The fidu-

Maximum multipole	$\ell_{\max} = 300$ (50)
Range of included scales k	$(10^{-3}$ – $10^{-1})$ Mpc^{-1} $N_k = 500$ (200)
Range of included redshifts z	10^{-4} – 10 $N_z = 1000$

Table 4.2: Numerical parameters used for the Fisher matrix analysis. The values in brackets are used for the results shown in Fig. 4.4. N_k and N_z are the numbers of equidistant steps in k and z. (The CMB Fisher matrix involves multipoles up to $\ell = 2250$ in all calculations.)

cial values are varied between -4 and 0 for $\log_{10} c_s^2$, and -0.99 and -0.6 for w. For each pair of fiducial values, the Fisher matrix analysis yields constraints $\Delta \log_{10} c_s^2$ and Δw (Cramér–Rao bounds, cf. Sec. 4.2.2). Since the Fisher matrix has to be computed many times for this application, we choose a somewhat reduced accuracy than for subsequent computations. The numerical parameters are specified in Tab. 4.2. The uncertainties $\Delta \log_{10} c_s^2$ and $\Delta w/|w|$ are shown in Fig. 4.4.

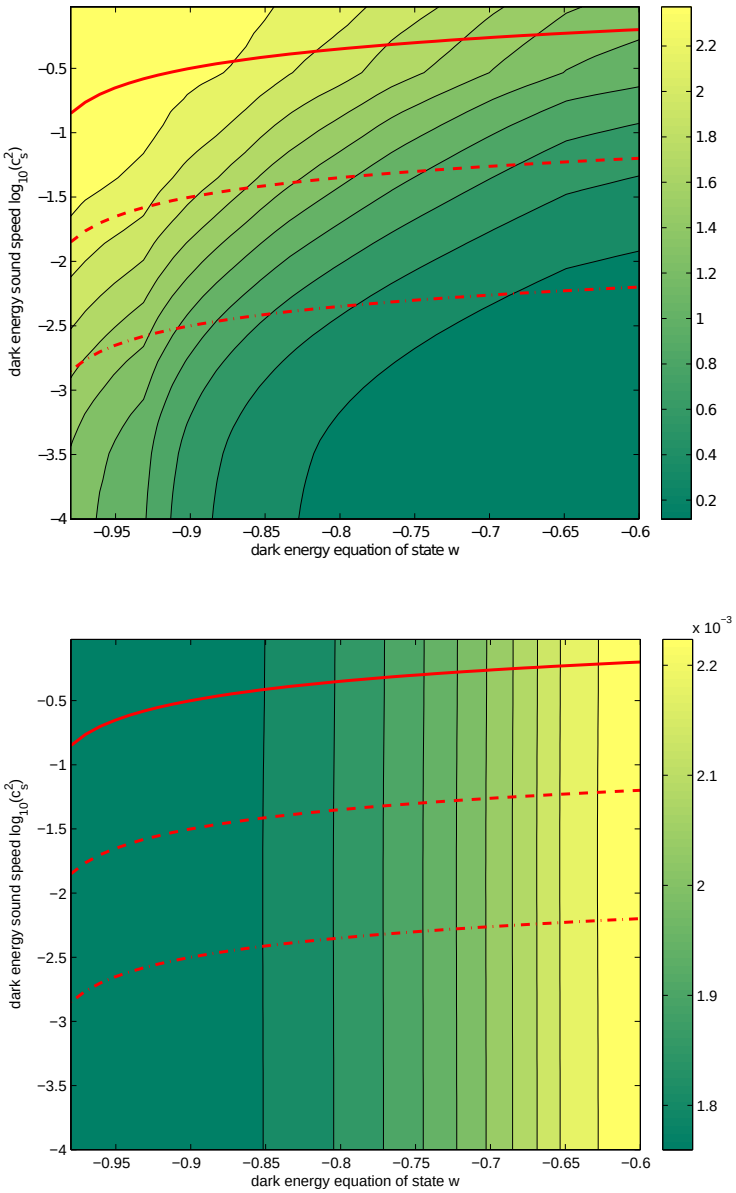

Figure 4.4: Cramér–Rao bounds on $\Delta \log_{10} c_s^2$ (upper figure) and $\Delta w/|w|$ (lower figure) for varying fiducial values w and $\log_{10} c_s^2$. The three red lines mark (from top to bottom) the scales $\lambda_{\text{eff}} = 10^{-n} \mathcal{H}_0^{-1}$, $n = 1, 2, 3$ (cf. Eq. 4.49).

Let us first discuss the constraints on the equation of state parameter w. The estimated errors $\Delta w/|w|$ are virtually independent of the assumed sound speed c_s^2 and below the percent level. Our findings agree with earlier results: Future 3D WL studies (combined with information from the CMB) offer promising prospects for constraining the dark energy equation of state w (Heavens, 2003; Heavens et al., 2006). The precise value of w plays an important role when it comes to constraints on the sound speed. Here, the figure shows a strong variation of $\Delta \log_{10} c_s^2$ over the considered range of fiducial parameters. For sufficiently small c_s^2, and w not too close to -1 (e. g. $w \gtrsim -0.95$), we can identify regions with $\Delta \log_{10} c_s^2 \lesssim 1$. In these cases, next–generation surveys may be capable of determining the order of magnitude of c_s^2. Since current data prefer an equation of state very close to -1 (e. g. $w \approx -0.97$, see Sec. 2.1.3), dark energy clustering (in uncoupled scenarios) will only be detectable if c_s^2 is close to zero.

Full Fisher matrix analysis

We will now include variations in all six parameters of our model. Since the value of c_s^2 is completely undetermined, we freely chose an exemplary fiducial value $c_s^2 = 10^{-2}$. A natural choice of fiducial parameters for Ω_m^0, A_s, h, n_s is given by the WMAP recommended parameters (Komatsu et al., 2011). The choice of w is problematic, since the effect of dark energy clustering vanishes for $w \to -1$. Disregarding current observational constraints on w, we thus choose the illustrative value $w = -0.8$ for which dark energy perturbations grow on sub–horizon scales (cf. Figs. 4.2 and 4.3). This choice of w also corresponds to other studies of dark energy perturbations (e. g. Sapone and Kunz, 2009; Sapone et al., 2010).

In Fig. 4.5, we show the confidence regions constructed from the Fisher matrix. The combination of 3D WL and the CMB provides stringent bounds on most of the parameters. The sound speed c_s^2 is pinned down within an order of magnitude. This does not change significantly if one considers 3D WL alone (cf. Ayaita et al., 2012a). The tight constraints on A_s and n_s, on the other hand, are mainly due to the CMB.

We can further investigate which range of multipoles ℓ needs to be incorporated for constraining a specific parameter. For this purpose, we consider the estimated errors Δp_i as a function of $\ell_{\max}$. In Fig. 4.6, we plot $\Delta \log_{10} c_s^2$ together with the relative errors $\Delta p_i/|p_i|$ ($p_i \neq \log_{10} c_s^2$) for varying $\ell_{\max}$. We observe that $\log_{10} c_s^2$ is mainly constrained by multipoles $\ell \lesssim 20$; further increasing $\ell_{\max}$ cannot considerably reduce the error on $\log_{10} c_s^2$. Since dark energy clustering is a large–scale phenomenon (cf. Sec. 4.4.1), this comes as no surprise. As can be easily seen within the Limber approximation (cf. Ayaita et al., 2012b), the multipole ℓ primarily probes the scale $k \approx \ell/r_*$, where r_* is a characteristic comoving distance of the survey (for instance, the position of the peak in the galaxy distribution, cf. Eq. 4.17). Hence, increasing $\ell_{\max}$ primarily adds more information coming from small scales, which however are not very sensitive to c_s^2.

On the other hand, the companion figure shows that Ω_m, h, and w benefit a lot from larger multipoles. For these parameters, the 3D WL signal on smaller scales provides valuable information. The parameters of the primordial spectrum, A_s and n_s, are different. As already mentioned above, they are mainly constrained

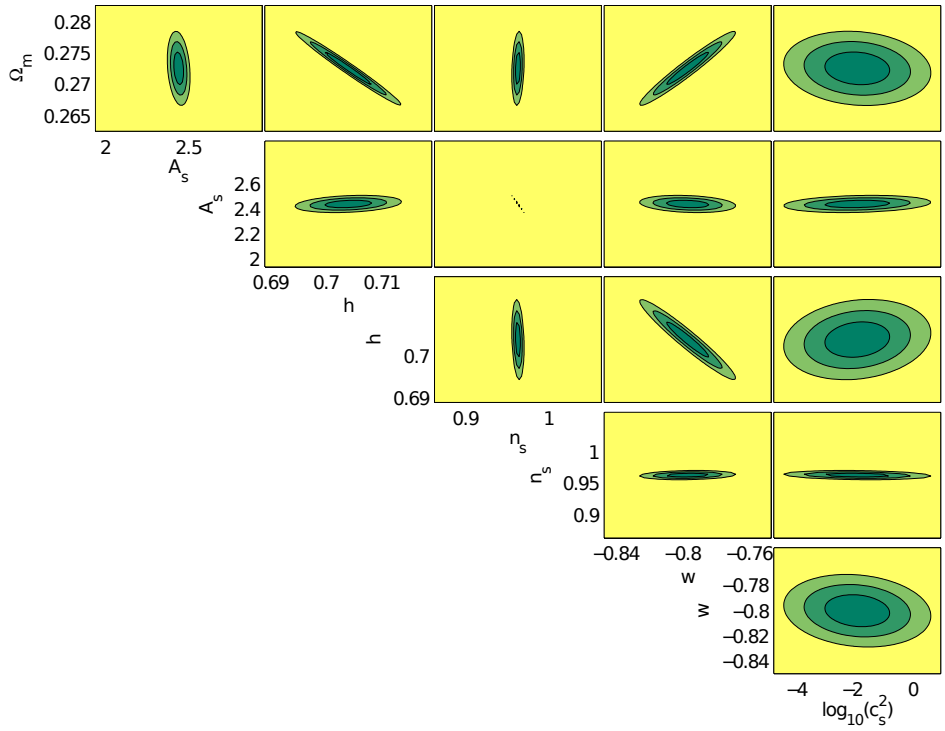

Figure 4.5: Estimated confidence ellipses (1σ, 2σ, and 3σ) for the combination of 3D WL with the CMB. The constraints on A_s have been rescaled by a factor of 10^9.

by the CMB and the 3D WL signal cannot notably improve these tight constraints. Therefore, the uncertainties ΔA_s and Δn_s are almost independent of $\ell_{\max}$.

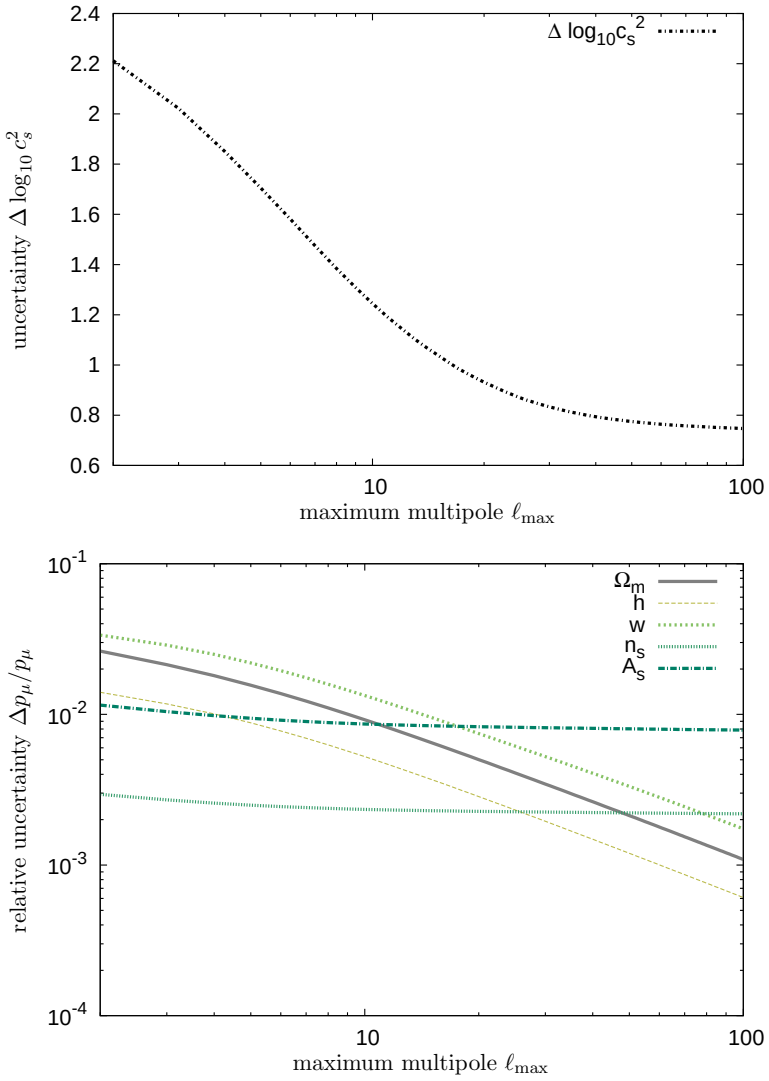

Figure 4.6: Estimated uncertainty $\Delta \log_{10} c_s^2$ (upper figure) and relative uncertainties $\Delta p_i/|p_i|$ for other cosmological parameters (lower figure) as a function of the maximum multipole $\ell_{\max}$ entering the 3D WL analysis. (The CMB Fisher matrix generally includes all multipoles from 2 to 2250.)

Summary

Forecasts for constraints on the sound speed parameter c_s^2 strongly depend on the assumed fiducial values for the equation of state w and c_s^2 itself. We have quantified this dependence in Fig. 4.4. Although it remains challenging to constrain c_s^2 for w close to -1, our results show that it is worthwhile to consider 3D WL in addition to tomography and galaxy clusters (cf. Sapone et al., 2010). With a combination of data from Euclid and Planck, it may become possible to determine the order of magnitude of c_s^2. Choosing illustrative fiducial values $w = -0.8$ and $c_s^2 = 10^{-2}$, for which dark energy clustering affects sub–horizon scales, we have found promising constraints on all cosmological parameters, cf. Figs. 4.5 and 4.6; the constraints on c_s^2 will be weaker for w closer to -1 or larger values of c_s^2.

The value of c_s^2 can help to distinguish between simple scenarios of dark energy (cf. Sec. 4.4.1). Measuring the order of magnitude $\log_{10} c_s^2$ could already be a decisive step into this direction. On the other hand, we have already mentioned that in more complex models of dark energy the speed of sound parameter c_s^2 becomes less important. From a more general perspective, our results suggest that 3D WL provides a valuable probe of the large–scale gravitational potentials. This is of particular interest for scenarios in which the large–scale dynamics deviate from ΛCDM. The comparison of 3D WL spectra with actual data, coming, e. g., from Euclid, may yield stringent constraints on the parameters of these models.

5 Simulating Growing Neutrino Quintessence

In Chapter 3, we have introduced GNQ as a possible solution to the "why now" problem of dark energy. Understanding its evolution on the level of perturbations is, however, challenging (cf. Sec. 3.3.2). The strong coupling between neutrinos and the cosmon field induces non–linear neutrino clustering on cosmic scales. Furthermore, variations of the neutrino mass in space and time have to be taken into account. An appropriate method is required that allows us to follow the cosmological evolution of GNQ including all major effects. Building on previous studies of the model, we will motivate a relativistic N–body treatment of growing neutrinos combined with an explicit computation of the local cosmon field (Sec. 5.1). The development and application of this simulation method has led to a publication (Ayaita et al., 2012b). In this work, we focus on the modelling of the neutrino species. We will derive the equation of motion and explain the numerical realization in Sec. 5.2; the generation of initial conditions and the computation of relevant components of the averaged neutrino energy–momentum tensor are also part of this section. In Sec. 5.3, we then turn to the computation of the cosmon field. The treatment of gravity and matter will be described in Sec. 5.4. Finally, we comment on the runtime and resolution of the method (Sec. 5.5).

5.1 Requirements and general setup

The results of linear perturbation theory (Mota et al., 2008) show that at redshift $z \lesssim 2$ the neutrino density contrast becomes of order unity on large scales ($k \sim 10^{-2} h/\mathrm{Mpc}$). The linear approximation consequently becomes invalid from this time on. For any quantitative analysis of GNQ at later time, it is necessary to overcome the linear theory and to simulate the fully nonlinear evolution of neutrino perturbations. This brings us to the first and most fundamental requirement on our method:

Requirement 1. *Accurate evolution of neutrino perturbations in the nonlinear regime. In particular, neutrino density perturbations $\delta\rho_\nu(x)$ can no longer be treated as linear perturbations.*

In a first approach, Wintergerst et al. (2010) studied isolated neutrino overdensities in hydrodynamic simulations. Their findings suggest that the overdensities collapse and form virialized lumps. Hydrodynamic equations of motion, however, usually employ only the first few moments of the phase–space distribution function $f(\eta, x^i, p_j)$. Since higher moments may play an important role for the nonlinear process of lump formation, we advocate a method that directly samples the

neutrino phase–space distribution function f_ν. This is the basic idea of N–body simulations (for a brief review of the theory and history of N–body simulations, see, e. g., Dehnen and Read, 2011; Dolag et al., 2008; Bagla and Padmanabhan, 1997). This simulation technique has become a powerful tool of computational cosmology. To give some examples of their applications, N–body simulations have been used to rule out the hot dark matter scenario (Davis et al., 1985), and to characterize the density profile of dark matter halos (Navarro et al., 1996). Nowadays, large simulations provide robust and precise predictions concerning the formation of dark matter structures and galaxies that can be confronted with data from extensive galaxy surveys in order to test the paradigm of structure formation (Springel et al., 2005). N–body simulations are not only used within the standard model, but have also been applied to many competing models (e. g., Zhao et al., 2011; Li et al., 2011; Khoury and Wyman, 2009; Stabenau and Jain, 2006).

Extensions of the successful GADGET-2 code (Springel, 2005) exist that are designed to incorporate an interacting dark energy component (Baldi et al., 2010). In particular, a first implementation of GNQ has been studied and allowed to investigate some aspects of the model (Baldi et al., 2011). Several important features of the model could, however, not have been included yet. First of all, on the level of perturbations, the neutrino mass varies in space and time (cf. Eq. 3.8),

$$m_\nu(x) = m_\nu(\bar{\varphi})\, \exp(-\beta\, \delta\varphi(x)), \tag{5.1}$$

with $m_\nu(\bar{\varphi}) \propto \exp(-\beta\bar{\varphi})$ abbreviating the purely time dependent part. The method employed by Baldi et al. (2011) neglect the variation due to the cosmon fluctuations $\delta\varphi(x)$. But even if $\delta\varphi$ is still linear, the combination $\beta\,\delta\varphi$ can reach order unity (typically, $|\beta| \sim 10^2$). Studying idealized configurations, Nunes et al. (2011) found that the local neutrino mass inside nonlinear structures can be substantially suppressed, $m_\nu(x) \ll m_\nu(\bar{\varphi})$, which, in turn, strongly influences the neutrino–induced gravitational potential. A reliable estimate of the gravitational potential is, for example, crucial in connection with CMB observables (Pettorino et al., 2010). In addition, local mass variations can have important dynamical impacts. Hence, we decide to resolve the local cosmon field and to respect spatial variations of the neutrino mass:

Requirement 2. *Explicit computation of the cosmon perturbations $\delta\varphi(x)$ in order to allow for local neutrino mass variations.*

The first N–body approach to GNQ revealed another important obstacle. We have already pointed out that the cosmon–mediated fifth force is substantially stronger than gravity. Standard N–body schemes employ Newtonian dynamics to describe the acceleration of particles. Within this description, the extra force can be described in terms of an effective Newton constant (cf. Baldi et al., 2011),

$$G_{\text{eff}} = G\,(1 + 2\beta^2) \gtrsim 5000\, G, \tag{5.2}$$

for typical values of β (we will use $\beta = -52$). In consequence, neutrinos feel a rapid acceleration once the coupling is effective, i. e., once they have become sufficiently non–relativistic. Baldi et al. (2011) have studied the growth of neutrino velocities

and found that at $z \lesssim 1.5$ roughly 80% of the neutrino particles already have velocities larger than $0.1\,c$; in the subsequent evolution, the neutrino velocities exceed the speed–of–light limit. The Newtonian description breaks down and we have to respect the fully relativistic law of motion instead:

Requirement 3. *Relativistic description of the neutrino dynamics. The law of motion remains valid for velocities close to the speed of light.*

Furthermore, careful attention has to be paid to the evolution of the cosmological background. In the standard approach, the evolution of all background quantities is obtained independently from perturbations. Technically this means that, in a first step, perturbations are completely neglected and the field equations are solved for "averaged" quantities. In a second step, perturbations are introduced and their evolution is studied on the previously calculated cosmological background. The reason why this procedure usually works well is the smallness of perturbations: Starting from the full field equations, one arrives at the usual background equations if one first linearizes in the perturbations and then performs the average (perturbations are defined with vanishing mean). In the presence of nonlinearities, this procedure can become inaccurate and perturbations can give rise to correction terms influencing the evolution of the averaged quantities. This phenomenon is referred to as *backreaction*. It is a well known issue whether nonlinear matter perturbations can introduce significant corrections to the dynamics of the metric, possibly even accounting for the observed cosmic acceleration (cf., e. g., Buchert and Ehlers, 1997; Wetterich, 2003; Rasanen, 2004; Behrend et al., 2008; Brown et al., 2009). However, estimates suggest that the backreaction effect induced by CDM structure formation introduces only small corrections (Wetterich, 2003). In GNQ, on the contrary, the situation is expected to be different (Baldi et al., 2011; Nunes et al., 2011; Pettorino et al., 2010). This is also related to the strong mass suppressions inside nonlinear structures (as will become clearer in Sec. 5.2.4). We conclude that the usual split between background and perturbations is not advisable in GNQ:

Requirement 4. *Adequate treatment of backreaction effects on the cosmological background evolution due to the presence of nonlinear neutrino perturbations.*

Finally, let us consider the initial conditions for an N–body simulation of GNQ. It is our intention to provide an accurate continuation of linear perturbation theory. Hence, when distributing particles and assigning initial peculiar velocities, we need to respect the predicted statistics of the perturbation variables as obtained from the linear calculation (Mota et al., 2008):

Requirement 5. *Appropriate generation of initial conditions consistent with the results of linear perturbation theory.*

In the subsequent sections, we will present our simulation method in detail and derive the necessary equations. In summary, the aforementioned requirements motivate the following general setup:

- The neutrino and matter components in the Universe are described by a finite number of effective N–body particles.
- Each neutrino particle carries a (comoving) position vector $\boldsymbol{x}$, a peculiar velocity vector $\boldsymbol{v} = \mathrm{d}\boldsymbol{x}/\mathrm{d}\eta$, and a (variable) mass M_ν. Matter particles carry a position vector and a velocity vector; their mass M_m is constant.
- Necessary dynamical fields are realized on a three–dimensional grid. In particular, the cosmon perturbations $\delta\varphi(x)$ are explicitly computed and discretized.
- Neutrino particles are accelerated using the fully relativistic law of motion. Their mass varies according to the present position of the particle (Eq. 5.1). For matter particles, the Newtonian description is sufficient.
- Background quantities are evolved simultaneously to perturbations. The required components of the average neutrino energy–momentum tensor are *measured* in the simulation volume.
- The initial conditions for the simulation are obtained from the linear code (Mota et al., 2008). An appropriate routine generates initial particle configurations respecting correlations between perturbations.

We specify the properties and typical values of our simulation in Tab. 5.1.

Description	*Symbol*	*Typical value*
Simulation volume (cubical)	$V = L^3$	$600^3\, h^{-3}\mathrm{Mpc}^3$
Neutrino particles	N_ν	2×10^7
Matter particles	N_m	2×10^7
Particle properties	$\boldsymbol{x}$, $\boldsymbol{v}$, M_ν, M_m	-
Number of cells	N_c	256^3
Size of a cell	$\Delta x = L/N_c^{1/3}$	$2.34\ h^{-1}\mathrm{Mpc}$
Dynamical fields	Ψ, Φ, $\delta\varphi$	-
Background quantities	$\mathcal{H}$, $\bar{\varphi}$, $\bar{\rho}_\nu$, $\bar{P}_\nu$, $\bar{\rho}_m$	
Initial redshift	z_i	4 (neutrinos), 49 (matter)

Table 5.1: Simulation Properties. All lengths are in comoving units.

5.2 Modelling of neutrinos

The neutrino component plays the central role in our simulations. In this section, we will discuss the theoretical and numerical aspects concerning its treatment. Let us start with deriving the relativistic law of motion.

5.2.1 Equation of motion

In our model, the motion of a neutrino particle deviates from the standard geodesic equation due to the coupling to the cosmon field φ. This coupling is realized as a varying mass $m_\nu(\varphi(\xi))$ along the particle's world line ξ^α. We thus propose the one–particle action,

$$\begin{aligned} S_\nu &= -\int \mathrm{d}\tau\, m_\nu(\varphi(\xi)) \\ &= -\int \sqrt{-g_{\alpha\beta}\mathrm{d}\xi^\alpha \mathrm{d}\xi^\beta}\, m_\nu(\varphi(\xi)), \end{aligned} \tag{5.3}$$

with the particle's proper time τ defined via $\mathrm{d}\tau = \sqrt{-g_{\alpha\beta}\mathrm{d}\xi^\alpha \mathrm{d}\xi^\beta}$. Varying the action with respect to the ξ^α yields the modified geodesic equation. In the uncoupled case, $m_\nu = \text{const.}$, the result reduces to the standard geodesic equation in curved spacetime (see, e. g., Carroll, 2004). The variation corresponds to

$$\xi^\alpha \;\mapsto\; \xi^\alpha + \delta\xi^\alpha, \tag{5.4}$$

$$g_{\alpha\beta} \;\mapsto\; g_{\alpha\beta} + \partial_\sigma g_{\alpha\beta}\, \delta\xi^\sigma \tag{5.5}$$

$$\begin{aligned} m_\nu(\varphi) \;&\mapsto\; m_\nu(\varphi) + \partial_\alpha m_\nu(\varphi)\, \delta\xi^\alpha \\ &= m_\nu(\varphi) - \beta\, m_\nu(\varphi)\, \partial_\alpha\varphi\, \delta\xi^\alpha, \end{aligned} \tag{5.6}$$

where we have used the definition $\beta = -\mathrm{d}\ln m_\nu/\mathrm{d}\varphi$ in the last line. We remark that the whole derivation is not restricted to a constant coupling constant β, but equally applies to the general case[1], $\beta = \beta(\varphi)$. In order to keep notation short, we nevertheless simply write β.

The variation of the action, Eq. (5.3), yields

$$\delta S_\nu = \int \mathrm{d}\tau\, m_\nu(\varphi) \left(\frac{1}{2}\partial_\sigma g_{\alpha\beta} \frac{\mathrm{d}\xi^\alpha}{\mathrm{d}\tau}\frac{\mathrm{d}\xi^\beta}{\mathrm{d}\tau}\delta\xi^\sigma + \beta\, \partial_\alpha\varphi\, \delta\xi^\alpha + g_{\alpha\beta}\frac{\mathrm{d}\xi^\alpha}{\mathrm{d}\tau}\frac{\mathrm{d}(\delta\xi^\beta)}{\mathrm{d}\tau} \right). \tag{5.7}$$

The last term requires integration by parts,

$$\int \mathrm{d}\tau\, m_\nu(\varphi) g_{\alpha\beta}\frac{\mathrm{d}\xi^\alpha}{\mathrm{d}\tau}\frac{\mathrm{d}(\delta\xi^\beta)}{\mathrm{d}\tau} = -\int \mathrm{d}\tau \frac{\mathrm{d}}{\mathrm{d}\tau}\left(m_\nu(\varphi)\, g_{\alpha\beta}\frac{\mathrm{d}\xi^\alpha}{\mathrm{d}\tau} \right) \delta\xi^\beta, \tag{5.8}$$

and gives rise to another extra term due to the time derivative acting on m_ν,

$$\frac{\mathrm{d}m_\nu(\varphi(\xi))}{\mathrm{d}\tau} = -\beta\, m_\nu(\varphi)\, \partial_\alpha\varphi\, \frac{\mathrm{d}\xi^\alpha}{\mathrm{d}\tau}. \tag{5.9}$$

[1] This is true since only first order derivatives of $m_\nu(\varphi)$ are involved. Secondary derivatives would also act on $\beta(\varphi)$.

The final result can be written as

$$\delta S_\nu = -\int \mathrm{d}\tau\, m_\nu(\varphi)\,\delta\xi^\sigma \times \tag{5.10}$$
$$\left[g_{\alpha\sigma}\frac{\mathrm{d}^2\xi^\alpha}{\mathrm{d}\tau^2} + \frac{1}{2}\left(\partial_\alpha g_{\beta\sigma} + \partial_\beta g_{\alpha\sigma} - \partial_\sigma g_{\alpha\beta}\right)\frac{\mathrm{d}\xi^\alpha}{\mathrm{d}\tau}\frac{\mathrm{d}\xi^\beta}{\mathrm{d}\tau} - \beta\left(\partial_\sigma\varphi + g_{\alpha\sigma}\partial_\beta\varphi\frac{\mathrm{d}\xi^\alpha}{\mathrm{d}\tau}\frac{\mathrm{d}\xi^\beta}{\mathrm{d}\tau}\right)\right].$$

Modifications to the standard geodesic equation are proportional to the coupling constant β. Setting $\delta S_\nu = 0$ for arbitrary variations $\delta\xi^\alpha$ yields the equation of motion,

$$\boxed{\frac{\mathrm{d}u^\alpha}{\mathrm{d}\tau} + \Gamma^\alpha_{\rho\sigma}u^\rho u^\sigma = \beta\,\partial^\alpha\varphi + \beta\,u^\lambda\partial_\lambda\varphi\,u^\alpha,} \tag{5.11}$$

with the four–velocity $u^\alpha = \mathrm{d}\xi^\alpha/\mathrm{d}\tau$ and the Christoffel symbols

$$\Gamma^\alpha_{\rho\sigma} = \frac{1}{2}g^{\alpha\lambda}(\partial_\rho g_{\lambda\sigma} + \partial_\sigma g_{\lambda\rho} - \partial_\lambda g_{\rho\sigma}). \tag{5.12}$$

The same result can also be derived from Eq. (3.1) describing the energy–momentum transfer between neutrinos and quintessence. All we have to do is specify the one–particle neutrino energy–momentum tensor $T^{\alpha\beta}$. A straightforward generalization of the expression known from special relativity is given by

$$T^{\alpha\beta} = \frac{1}{\sqrt{-g}}\int \mathrm{d}\tau\, m_\nu(\varphi(\xi))\,u^\alpha u^\beta\delta^4_D(x-\xi), \tag{5.13}$$

where the factor $(-g)^{-1/2}$ is required by the normalization of the Dirac delta function in curved spacetime. The form of the energy–momentum tensor can also be derived from the proposed action, Eq. (5.3), employing the general definition, Eq. (2.3). Using the normalization of the four–velocity, $u^\alpha u_\alpha = -1$, the right–hand side of Eq. (3.1) is simply given by

$$-\beta\,T\,\partial^\alpha\varphi = \frac{1}{\sqrt{-g}}\int \mathrm{d}\tau\, m_\nu(\varphi)\,\beta\,\partial^\alpha\varphi\,\delta^4_D(x-\xi). \tag{5.14}$$

Evaluating the covariant derivative on the left–hand side,

$$\nabla_\beta T^{\alpha\beta} = \partial_\beta T^{\alpha\beta} + \Gamma^\alpha_{\beta\lambda}T^{\lambda\beta} + \Gamma^\lambda_{\beta\lambda}T^{\alpha\beta}, \tag{5.15}$$

we have to pay attention to derivatives acting on $m_\nu(\varphi)$. Let us consider

$$\begin{aligned}
\partial_\beta(\sqrt{-g}\,T^{\alpha\beta}) &= \int \mathrm{d}\tau\, m_\nu(\varphi(\xi))u^\alpha u^\beta\frac{\partial}{\partial x^\beta}\delta^4_D(x-\xi) && (5.16)\\
&= -\int \mathrm{d}\tau\, m_\nu(\varphi(\xi))u^\alpha u^\beta\frac{\partial}{\partial\xi^\beta}\delta^4_D(x-\xi) && (5.17)\\
&= \int \mathrm{d}\tau\,\frac{\mathrm{d}}{\mathrm{d}\tau}\Big(m_\nu(\varphi)\,u^\alpha\Big)\,\delta^4_D(x-\xi), && (5.18)
\end{aligned}$$

where we have used the chain rule $u^\beta\frac{\partial}{\partial\xi^\beta} = \frac{\mathrm{d}}{\mathrm{d}\tau}$ and integrated by parts. The time–derivative $\mathrm{d}m_\nu/\mathrm{d}\tau$ is already known from Eq. (5.9). Apart from this extra

term, Eq. (5.15) reproduces the standard geodesic equation. Thus, we can already anticipate the result,

$$\begin{aligned}\nabla_\beta T^{\alpha\beta} =& \frac{1}{\sqrt{-g}} \int \mathrm{d}\tau \, m_\nu(\varphi) \, \delta_D^4(x-\xi) \\ & \times \left(\frac{\mathrm{d}u^\alpha}{\mathrm{d}\tau} + \Gamma^\alpha_{\rho\sigma} u^\rho u^\sigma - \beta \, u^\lambda \partial_\lambda \varphi \, u^\alpha \right). \end{aligned} \tag{5.19}$$

Together with Eq. (5.14), we again obtain Eq. (5.11). It is worth mentioning that the equation of motion for coupled neutrinos can also be derived using a conformal transformation of the standard geodesic equation (Baldi et al., 2011).

Interpretation

The law of motion, Eq. (5.11), describes the deviation from the free geodesic motion due to the cosmon–neutrino coupling. On the left–hand side, we identify the standard geodesic equation with the Christoffel symbols accounting for gravity. They give rise to the usual Hubble damping and describe local curvature effects in terms of the potentials Ψ and Φ (see Eq. 3.26 for the metric). Let us focus on the terms on the right–hand side:

- The first term, $\beta \, \partial^\alpha \varphi$, contains the cosmon–mediated fifth force: The gradient $\boldsymbol{\nabla}\varphi$ contributes to the acceleration $\mathrm{d}\boldsymbol{u}/\mathrm{d}\tau$. In the case of a smooth cosmon field, $\varphi(x) = \bar{\varphi}(\eta)$, the effect vanishes. In Sec. 5.3, we will briefly discuss the Newtonian limit and confirm that the force is about $2\beta^2$ times stronger than gravity (consistent with Eq. 5.2).

- The second term, $\beta \, u^\lambda \partial_\lambda \varphi \, u^\alpha$, represents a velocity–dependent force that can be understood from momentum conservation: A particle is accelerated if it looses mass along its path; a growing mass implies deceleration. At the background level, the neutrino mass only changes due to time variations of the homogeneous cosmon field $\bar{\varphi}$. This effect is usually interpreted as a modification of the Hubble damping (cf. Baldi et al., 2011), $\mathcal{H} \mapsto (\mathcal{H} - \beta\bar{\varphi}')$. Including perturbations, the mass also changes due to the particle's motion through the inhomogeneous field $\varphi(x)$. The scalar product $u^\lambda \partial_\lambda \varphi = \boldsymbol{u} \cdot \boldsymbol{\nabla}\varphi + u^0 \varphi'$ incorporates both contributions.

5.2.2 Time integration

With the previously derived equation of motion, we can straightforwardly evolve a particle's four–velocity $\boldsymbol{u}$ in time. However, in order to move particles in our simulation volume, we actually require their coordinate velocity $\boldsymbol{v} = \mathrm{d}\boldsymbol{x}/\mathrm{d}\eta$. It is related to the four–velocity via

$$\boldsymbol{u} = \frac{\mathrm{d}\eta}{\mathrm{d}\tau} \, \boldsymbol{v} = u^0 \, \boldsymbol{v}. \tag{5.20}$$

At this point, it is convenient to introduce a generalization of the Lorentz factor,

$$\gamma = \frac{\sqrt{-g_{00}}\mathrm{d}x^0}{\mathrm{d}\tau} \tag{5.21}$$

$$= \frac{1}{\sqrt{1-(1-2\Psi-2\Phi)\boldsymbol{v}^2}}. \tag{5.22}$$

The definition in the first line is chosen such that $\gamma = 1$ for a particle at rest. The second line directly follows from the metric, Eq. (3.26). Thus, $u^0 = \gamma\,(1-\Psi)/a$ (metric perturbations are treated in linear approximation). Solving Eq. (5.20) for $\boldsymbol{v}$ yields:

$$\boldsymbol{v} = \frac{a(1+\Psi)}{\sqrt{1+(1-2\Phi)a^2\boldsymbol{u}^2}}\boldsymbol{u}. \tag{5.23}$$

This procedure automatically respects the speed of light limit and is much more robust than dynamically evolving $\boldsymbol{v}$ itself. Note, that u^0 also relates $\mathrm{d}\boldsymbol{u}/\mathrm{d}\eta$ to $\mathrm{d}\boldsymbol{u}/\mathrm{d}\tau$, where the latter is given by Eq. (5.11).

We can now specify the numerical scheme for the time evolution of the effective neutrino particles in our simulation. Below, we will denote the acceleration of $\boldsymbol{u}$ by $\boldsymbol{g} = \mathrm{d}\boldsymbol{u}/\mathrm{d}\eta$. Let us consider a particle with the current position $\boldsymbol{x}_n$ and the current four–velocity $\boldsymbol{u}_n$ at an instant η_n (the subscript n labels discrete time steps). The position $\boldsymbol{x}_{n+1}$ and the four–velocity $\boldsymbol{u}_{n+1}$ at the time $\eta_{n+1} = \eta_n + \Delta\eta$ are obtained by the following procedure:

$$\boldsymbol{u}_{n+1} = \boldsymbol{u}_n + \boldsymbol{g}_n\Delta\eta, \quad \text{(by virtue of Eq. 5.11)} \tag{5.24}$$

$$\boldsymbol{u}_{n+1} \mapsto \boldsymbol{v}_{n+1}, \quad \text{(Eq. 5.23)} \tag{5.25}$$

$$\boldsymbol{x}_{n+1} = \boldsymbol{x}_n + \boldsymbol{v}_{n+1}\Delta\eta, \tag{5.26}$$

where $\boldsymbol{g}_n = \boldsymbol{g}(\eta_n, \boldsymbol{x}_n, \boldsymbol{u}_n)$. In contrast to the standard Euler method, we use $\boldsymbol{v}_{n+1}$ instead of $\boldsymbol{v}_n$ in the last line. This corresponds to the semi–implicit or symplectic Euler method (symplectic integrators are better suited to preserve certain invariants of motion, cf., e. g., Dehnen and Read, 2011; Vesely, 1994). A more common choice in modern N–body simulations is the *leapfrog integration* or generalizations thereof (e. g. Quinn et al., 1997). This second–order scheme updates position and velocity in an alternating way exploiting the fact that the acceleration $\boldsymbol{g}$ for standard Newtonian gravity does not depend on the velocity. For example, the so–called KDK ("kick–drift–kick") scheme (employed, e. g., in GADGET-2) sets $\boldsymbol{u}_{n+1} = \boldsymbol{u}_{n+1/2} + \frac{1}{2}\boldsymbol{g}_{n+1}$ after having obtained $\boldsymbol{x}_{n+1}$ and $\boldsymbol{u}_{n+1/2}$ from previous steps. In our case, the acceleration $\boldsymbol{g}_{n+1}$ also depends on $\boldsymbol{u}_{n+1}$ and we would have to solve an implicit equation for the final velocity update of each particle. For this reason, we stay with the simpler prescription given above.

The time–steps need not necessarily be chosen equidistant but may vary from step to step. The size of $\Delta\eta$ needs to be adjusted to the timescale of neutrino dynamics which is approximately $1/\sqrt{2\beta^2}$ times smaller than in simulations of standard gravity (Baldi et al., 2011). Further, we need to bear in mind that our resolution of the particles' dynamics is limited by the size Δx of the grid cells on which the dynamical fields ($\delta\varphi$, Ψ, Φ) are realized (cf. Secs. 5.3 and 5.4). Clearly,

the distance $|\boldsymbol{x}_{n+1} - \boldsymbol{x}_n|$ should be smaller than Δx for each particle in the simulation. Since the particles' speed is limited from above by the speed of light, we can impose the robust limit $\Delta\eta \ll \Delta x$. This criterion is most restrictive for high–resolution runs.

5.2.3 Initial conditions

We will now outline how to obtain an appropriate initial configuration of effective neutrino particles from which our simulation starts. First of all, we have to choose an initial redshift z_i at which we draw random perturbation fields according to the results of the linear theory. A convenient choice is $z_i = 4$ at which perturbations are still linear, but neutrinos are no longer highly relativistic ($w_\nu \approx 10^{-2}$ at $z = 4$ for the model investigated by Mota et al., 2008). This allows us to approximate the initial phase–space distribution function by taking into account only its first few moments. Local variations in the neutrino mass are also negligible at this early stage. We emphasize at this point, that $z_i = 4$ is not appropriate for the matter component, which has to be treated non–linearly much earlier; our N–body treatment of matter already starts at $z = 49$ (see also Sec. 5.4). In the following, we generally refer to the chosen initial redshift z_i and omit the time argument.

The unperturbed neutrino phase–space distribution function is given by the Fermi–Dirac distribution,

$$\bar{f}(v^i)\,\mathrm{d}^3v \propto \frac{1}{\mathrm{e}^{p/T_\nu} + 1}\,\mathrm{d}^3p \tag{5.27}$$

with $p^i = m_\nu u^i = \gamma m_\nu\, v^i$ and $T_\nu = T_\nu^0(1+z_i) = (4/11)^{1/3} T_\gamma^0(1+z_i)$ (cf. Sec. 2.1.3). In accordance with homogeneity and isotropy, $\bar{f}$ does not depend on $\boldsymbol{x}$ and the distribution of particle velocities is locally isotropic. The magnitude of the velocity dispersion decreases with the temperature but is non–negligible at $z_i = 4$. Once we include perturbations, the distribution in space involves small inhomogeneities described by $\delta_\nu(\boldsymbol{x})$ and the growth of perturbations implies peculiar motion $\boldsymbol{v}_\nu^{\mathrm{pec}}(\boldsymbol{x})$ which needs to be added to the thermal velocities drawn from $\bar{f}$. We approximate the perturbed phase–space distribution function by

$$f_\nu(x^i, v_j) = \frac{N_\nu}{V}\,\bar{f}(\boldsymbol{v} - \boldsymbol{v}_\nu^{\mathrm{pec}}(\boldsymbol{x}))\,(1 + \delta_\nu(\boldsymbol{x})). \tag{5.28}$$

The peculiar velocity field $\boldsymbol{v}_\nu^{\mathrm{pec}}$ is related to the scalar velocity perturbation v_ν introduced in Sec. 3.3.1 via $\boldsymbol{v}_\nu^{\mathrm{pec}} = \boldsymbol{\nabla} v_\nu$. The number density field follows as

$$n_\nu(\boldsymbol{x}) = \int \mathrm{d}^3v\, f_\nu(x^i, v_j) = \frac{N_\nu}{V}(1 + \delta_\nu(\boldsymbol{x})). \tag{5.29}$$

Once we have generated the initial perturbation fields $\delta_\nu(\boldsymbol{x})$ and $\boldsymbol{v}_\nu^{\mathrm{pec}}(\boldsymbol{x})$, the following steps are taken to sample the distribution function f_ν:

1. Each cell $\boldsymbol{x}_n$ ($n = 1, \ldots, N_c$) is assigned the rounded number of particles $\lfloor n(\boldsymbol{x}_i)\,(a_i \Delta x)^3 \rfloor$ (in order to correct the error statistically, a uniformly distributed random number is drawn which decides whether an additional par-

ticle is added or not). Within the volume of a single cell, the particles are distributed randomly.

2. For each particle, the thermal velocity $\boldsymbol{v}^{\mathrm{th}}$ is drawn from the Fermi–Dirac distribution. Therefor, we first obtain the magnitude of the momentum p from the distribution $\bar{f}(p)\mathrm{d}p \propto p^2\mathrm{d}p/[\exp(p/T_\nu)+1]$ and then use $v^{\mathrm{th}} = p/\sqrt{p^2+m_\nu^2}$. Second, a random vector $\hat{\boldsymbol{v}}$ is drawn from an isotropic distribution and normalized to $|\hat{\boldsymbol{v}}| = 1$. The sum of the thermal velocity $v^{\mathrm{th}}\hat{\boldsymbol{v}}$ and the peculiar velocity $\boldsymbol{v}^{\mathrm{pec}}(\boldsymbol{x})$ finally yields the total initial velocity of the particle. In order to enforce the local average $\langle \boldsymbol{v}^{\mathrm{th}}\rangle_{\boldsymbol{x}} = 0$, we generate a second particle with opposite thermal velocity at the same position (cf. Klypin et al., 1993).

We have checked our strategy by estimating the power spectra of the perturbation quantities δ_ν and v_ν from the particle distribution and comparing the results to the input from linear perturbation theory. Apart from an expected shot noise contribution due to discrete sampling (see, e. g., Amendola and Tsujikawa, 2010), we find good agreement at the specified initial redshift. The remainder of this section is dedicated to the procedure of realizing initial random fields $\delta_\nu(\boldsymbol{x})$ and $\boldsymbol{v}^{\mathrm{pec}}(\boldsymbol{x})$ on a discrete grid.

Discrete realizations of initial random fields

In Sec. 3.3.1, we have discussed the concept of stochastic initial conditions for the perturbation variables. There, we have introduced the mode functions (we assume the adiabatic mode) and the stochastic coefficients $\alpha(\boldsymbol{k})$ whose statistics are described by the primordial spectrum $P_{\mathrm{prim}}(k)$ (Eqs. 3.37 and 3.38). Once we have drawn a realization of $\alpha(\boldsymbol{k})$, the evolution of each perturbation quantity is determined (cf. Eq. 3.35), e. g.,

$$\begin{pmatrix}\delta_\nu(\eta,\boldsymbol{k})\\ v_\nu(\eta,\boldsymbol{k})\end{pmatrix} = \alpha(\boldsymbol{k})\begin{pmatrix}\delta_{\nu,k}(\eta)\\ v_{\nu,k}(\eta)\end{pmatrix}. \tag{5.30}$$

The (adiabatic) mode functions, $\delta_{\nu,k}$ and $v_{\nu,k}$, can be computed with the modified version of CAMB provided by Mota et al. (2008).

In our numerical implementation, the Gaussian random field $\alpha(\boldsymbol{k})$ is replaced by discrete random numbers $\tilde{\alpha}_i$ with $i = 1,\ldots,N_c$ labelling discrete modes $\boldsymbol{k}_i$. In particular, we employ a discrete Fourier transform (DFT) instead of the continuous transformation. The relation between $\alpha(\boldsymbol{k}_i)$ and $\tilde{\alpha}_i$ can be derived by discretizing the Fourier integral. For this purpose, we define $\boldsymbol{k}_i = (i_1,i_2,i_3)\Delta k$ with $\Delta k = 2\pi/L$ and $\boldsymbol{x}_j = (j_1,j_2,j_3)\Delta x$ with $\Delta x = L/n$, $n = (N_c)^{1/3}$. It follows

$$\begin{aligned}\alpha(\boldsymbol{k}_i) &= \int \mathrm{d}^3x\,\alpha(\boldsymbol{x})\,\mathrm{e}^{-\mathrm{i}\boldsymbol{k}_i\cdot\boldsymbol{x}_j}\\ &\approx \frac{V}{N_c}\sum_j \alpha(\boldsymbol{x}_j)\,\mathrm{e}^{-2\pi\mathrm{i}\,(i_1j_1+i_2j_2+i_3j_3)/n}\\ &= \frac{V}{N_c}\,\tilde{\alpha}_i,\end{aligned} \tag{5.31}$$

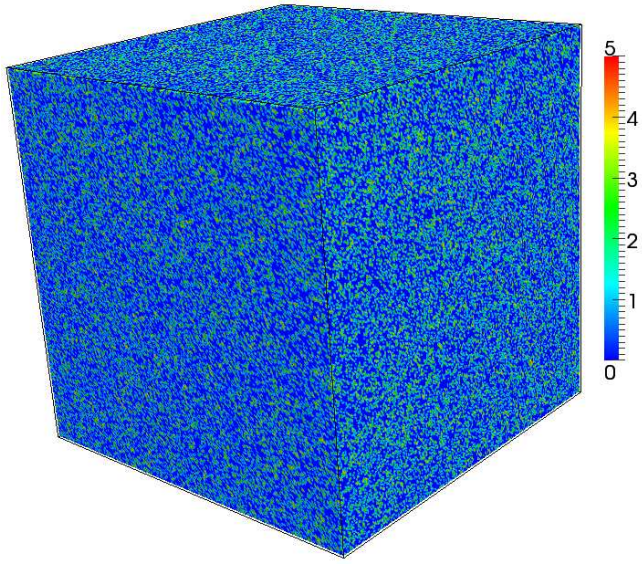

Figure 5.1: Illustration of neutrino inhomogeneities in our simulation box at $z_i = 4$. The colors indicate values of $n_\nu(\boldsymbol{x})/\bar{n}_\nu = 1 + \delta_\nu(\boldsymbol{x})$.

where we have used the definition of the three–dimensional DFT (cf. Galassi et al., 2009). In the next step, we also discretize the right–hand side of Eq. (3.38) by replacing the Dirac delta function by a Kronecker delta,

$$\begin{aligned}(2\pi)^3 P_{\rm prim}(k_i)\,\delta_D^3(\boldsymbol{k}_i - \boldsymbol{k}_j) &\approx (2\pi)^3 P_{\rm prim}(k_i)\,\frac{\delta_{ij}}{(\Delta k)^3} \\ &= P_{\rm prim}(k_i)\,L^3\,\delta_{ij}. \end{aligned} \tag{5.32}$$

The factor $(\Delta k)^{-3}$ appears due to the normalization condition $\int \mathrm{d}^3k\,\delta_D^3(\boldsymbol{k}) = 1$. The combination of Eqs. (5.31) and (5.32) provides the discrete version of Eq. (3.38):

$$\left\langle |\tilde{\alpha}_i|^2 \right\rangle = \frac{N_c^2}{V} P_{\rm prim}(k_i). \tag{5.33}$$

The coefficients $\tilde{\alpha}_i$ need to be drawn from a Gaussian distribution with vanishing mean and the specified variance. Additionally, we have to impose the reality condition for $\alpha(\boldsymbol{x})$, i. e. only approximately half of the N_c numbers $\tilde{\alpha}_i$ are independent and the others follow from $\alpha^*(\boldsymbol{k}) = \alpha(-\boldsymbol{k})$.

At last, we multiply with the corresponding mode functions and obtain random realizations of the perturbation fields in Fourier space. A final transform to real space yields the required perturbation fields. For illustration, Fig. 5.1 shows the simulation volume at $z_i = 4$ with colors indicating small neutrino inhomogeneities $n_\nu(\boldsymbol{x})/\bar{n}_\nu$.

5.2.4 Averaging the energy–momentum tensor

The evolution of the cosmological background in strongly coupled quintessence models is complicated by possible backreaction effects (Baldi et al., 2011; Nunes et al., 2011; Pettorino et al., 2010; Schrempp and Brown, 2010; Wetterich, 2003). In our case, the presence of nonlinearities in the neutrino fluid may have a great impact on the evolution of the averaged neutrino energy–momentum tensor $\bar{T}^{\alpha}_{\ \beta}$ and it is an important question to what extent this carries over to the dynamics of $\bar{\varphi}$. Our simulation method takes these effects into account by computing the actual averages $\bar{T}^{\alpha}_{\ \beta}$ in every time step. In particular, as will be explained in Sec. 5.3, the averaged trace $\bar{T}$ is used to evolve the background cosmon field $\bar{\varphi}$. Furthermore, the averaged energy density $\bar{\rho}_\nu$ enters the Friedmann equation determining the expansion rate, $3\mathcal{H}^2 = \sum_s \bar{\rho}_s a^2$ with $s \in \{m, \nu, \varphi\}$. We will now collect the expressions for computing averaged components of the neutrino energy–momentum tensor from the distribution of N–body particles.

Let us start with the energy density $\bar{\rho}_\nu = -\bar{T}^0_{\ 0}$. The energy density associated with a single particle with world line ξ^α is obtained from the one–particle energy–momentum tensor, Eq. (5.13). A straightforward computation yields

$$\rho = -T^0{}_0 = \frac{1}{\sqrt{\tilde{g}}}\,\gamma\, M_\nu\, \delta_D^3(\boldsymbol{x} - \boldsymbol{\xi}) \quad \text{(one–particle contribution)}, \tag{5.34}$$

with $\tilde{g}$ denoting the determinant of the spatial metric,

$$\tilde{g} = \det(g_{ij}), \qquad \sqrt{\tilde{g}} = a^3\,(1 - 3\Phi). \tag{5.35}$$

Summing up the contributions of all N_ν particles yields the total energy density $\rho_\nu(\boldsymbol{x})$. By virtue of ergodicity, we then calculate the average $\bar{\rho}_\nu$ according to

$$\bar{\rho}_\nu = \frac{\int_V \mathrm{d}^3x \sqrt{\tilde{g}} \rho_\nu(\boldsymbol{x})}{\int_V \mathrm{d}^3x\, \sqrt{\tilde{g}}} \tag{5.36}$$

$$= \frac{1}{a^3 V} \sum_{\text{particles } p} \gamma_p\, M_\nu[\varphi(\boldsymbol{\xi}_p)]. \tag{5.37}$$

Analogously, one can express the remaining components of the averaged energy–momentum tensor as sums over one–particle contributions. We quote the results for the pressure $\bar{P}_\nu = \bar{T}^i_{\ i}/3$ and the trace $\bar{T} = \bar{T}^\alpha_{\ \alpha}$:

$$\bar{P}_\nu = \frac{1}{a^3 V} \sum_{\text{particles } p} \frac{1}{3}\gamma_p\, M_\nu[\varphi(\boldsymbol{\xi}_p)]\,(1 - 2\Psi(\boldsymbol{\xi}_p) - 2\Phi(\boldsymbol{\xi}_p))\boldsymbol{v}_p^2, \tag{5.38}$$

$$\bar{T} = \frac{-1}{a^3 V} \sum_{\text{particles } p} \frac{M_\nu[\varphi(\boldsymbol{\xi}_p)]}{\gamma_p}. \tag{5.39}$$

Equations (5.37), (5.38), and (5.39) fulfill the familiar relationship $\bar{T} = -\bar{\rho}_\nu + 3\bar{P}_\nu$. The explicit appearance of Ψ and Φ in Eq. (5.38) can be rooted to our definition of the peculiar velocity with respect to the unperturbed metric.

Relevance

We illustrate the relevance of computing actual averages instead of using background equations using the example of $\bar{T}$. Equation (5.39) reveals that this quantity can be significantly affected by strong local mass suppressions (expected inside nonlinear structures corresponding to Nunes et al., 2011) and relativistic neutrino velocities. Both effects are only present at the level of perturbations and both go into the same direction: the suppression of $|\bar{T}|$ compared to the homogeneous solution. Neglecting these effects would lead to an inconsistent evolution. This can be illustrated as follows. We run a modified simulation without taking into account backreaction effects (the background can then be calculated a priori to the simulation). In the course of the evolution, neutrinos cluster under the influence of the strong fifth force. We measure the effect on $\bar{T}$ by comparing the actual average with the prediction of the pre–calculated background. The results are shown in Fig. 5.2 (we plot $-\bar{T}$ to allow easier comparison with $\bar{\rho}_\nu$). As expected, we observe the suppression of $|\bar{T}|$ due to the aforementioned effects. At early times, the correction is negligible, but once neutrino perturbations have entered the nonlinear regime, the disagreement becomes unacceptable. For comparison, we have also plotted the evolution of the measured average $\bar{\rho}_\nu$. The difference between $\bar{\rho}_\nu$ and $-\bar{T}$ manifests relativistic corrections. We conclude that backreaction in the cosmon–neutrino fluid cannot be neglected.

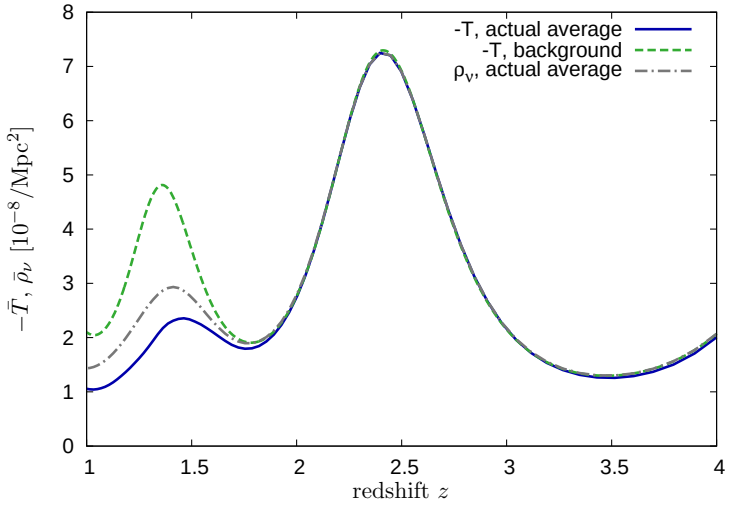

Figure 5.2: Illustration of the backreaction effect on $\bar{T}$. The plot shows how the actual average of $-\bar{T}$ more and more deviates from the assumed background evolution. Additionally, the figure also includes the actual average of the energy density $\bar{\rho}_\nu = -\bar{T}_\nu + 3\bar{P}_\nu$.

5.3 Computation of the cosmon field

The cosmon–neutrino interaction has important consequences for both species. Neutrinos are accelerated due to variations of $\varphi(x)$ (Eq. 5.11) and steadily change their mass according to Eq. (5.1). Let us now turn to the dynamics of the cosmon field itself. We have already derived the modified Klein–Gordon equation in Chapter 3, which we repeat here for convenience:

$$-\nabla^\alpha \nabla_\alpha \varphi + V_{,\varphi}(\varphi) = -\beta\, T, \tag{5.40}$$

with $T = T^\alpha{}_\alpha$ denoting the trace of the neutrino energy–momentum tensor.

5.3.1 Background and perturbation equations

We assume that the metric perturbations $\delta g_{\alpha\beta}$ and the cosmon perturbation $\delta\varphi$ can be treated in linear approximation and that their time derivatives are small compared to spatial derivatives. Under these assumptions, we can straightforwardly split Eq. (5.40) into a background field $\bar\varphi$ and a perturbation $\delta\varphi$. At the background level, we find

$$\bar\varphi'' + 2\mathcal{H}\bar\varphi' + a^2 V_{,\varphi}(\bar\varphi) = -a^2\beta\,\bar T. \tag{5.41}$$

We have already discussed the meaning of this equation in Sec. 3.1. Once neutrinos have become non–relativistic, $\bar T = -\bar\rho_\nu$, the term on the right–hand side shall slow down the evolution of $\bar\varphi$. As already emphasized at the beginning of this chapter, backreaction effects require us to obtain averaged neutrino quantities directly from the particle distribution. The computation of $\bar T$ was presented in Sec. 5.2.4. With this quantity at hand, we can use Eq. (5.41) to evolve $\bar\varphi$ and $\bar\varphi'$ in parallel to the particles.

Let us now focus on the perturbation field $\delta\varphi$. From Eq. (5.40), we obtain to first order in the perturbations

$$\Delta\delta\varphi - a^2 V_{,\varphi\varphi}(\bar\varphi)\,\delta\varphi + 2\Psi(\bar\varphi'' + 2\mathcal{H}\bar\varphi') = a^2\beta\,\delta T. \tag{5.42}$$

In the fluid description, we would have $\delta T = -\delta\rho_\nu + 3\delta P_\nu$. Instead, we calculate δT directly from the distribution of particles. Before we turn to the numerical treatment of this equation, let us have a brief look at its Newtonian approximation which is better suited for interpretation.

The fifth force in the Newtonian limit

For a moment, let us neglect gravity and assume non–relativistic neutrinos, $P_\nu \ll \rho_\nu$. The simplified equation then takes the form

$$\Delta_r\delta\varphi - V_{,\varphi\varphi}(\bar\varphi)\,\delta\varphi = -\beta\,\delta\rho_\nu, \tag{5.43}$$

where Δ_r denotes the Laplace operator with respect to physical coordinates $\boldsymbol{r} = a\boldsymbol{x}$. A solution of this equation is given by the well–known Yukawa potential,

$$\delta\varphi(\boldsymbol{r}) = \beta \int \mathrm{d}^3 r' \, \frac{\delta\rho_\nu(\boldsymbol{r}')}{4\pi|\boldsymbol{r}-\boldsymbol{r}'|} \, \mathrm{e}^{-m_\varphi|\boldsymbol{r}-\boldsymbol{r}'|}, \tag{5.44}$$

with $m_\varphi^2 = V_{,\varphi\varphi}(\bar{\varphi})$. Comparing this result with the Newtonian gravitational potential $\Psi_\nu(\boldsymbol{r})$ generated by neutrino inhomogeneities $\delta\rho_\nu(\boldsymbol{r})$, the only differences (neglecting homogeneous solutions) are the exponential screening, $\exp(-m_\varphi|\boldsymbol{r}-\boldsymbol{r}'|)$, and an overall factor.

The fifth force mediated by $\delta\varphi$ has a characteristic range $l_\varphi = m_\varphi^{-1}$. During the scaling regime it is related to the Hubble radius via $l_\varphi = \sqrt{2}/3\, H^{-1}$ (Wetterich, 1995; Amendola et al., 2008). We further know that $\Omega_\varphi = \rho_\varphi/(3H^2) = 3/\alpha^2$ during matter domination (cf. Sec. 2.2.2), implying $H = \alpha\sqrt{\rho_\varphi}/3$. Once the coupling has become effective, we may assume that φ stays approximately constant (cf., e. g., Fig. 3.1). This allows us to estimate l_φ in recent times:

$$l_\varphi \approx \sqrt{\frac{2}{3\alpha^2\Omega_\varphi^0}} H_0^{-1} \approx 0.1\, H_0^{-1}, \tag{5.45}$$

for $\Omega_\varphi^0 \approx 0.7$ and $\alpha = 10$. This result shows that the range of the force extends to cosmic scales.

The overall factor is given by $2|\beta|$ in units where $8\pi G = 1$. Taking into account another factor of $|\beta|$ in front of $\boldsymbol{\nabla}\delta\varphi$ in the equation of motion for neutrinos (5.11), we arrive at the often–cited relationship $|\boldsymbol{F}| \approx 2\beta^2 |\boldsymbol{F}_{\mathrm{gravity}}|$ characterizing the strength of the fifth force $\boldsymbol{F}$. In summary, neutrinos feel a new attractive, long–ranged force which is substantially stronger than gravity.

5.3.2 Solving the perturbed Klein–Gordon equation

For a given neutrino source term $\delta T(\boldsymbol{x})$, the perturbed Klein–Gordon Equation (5.42) can be treated similar to the Poisson equation for gravity. In Fourier space,

$$\left(\Delta - a^2 V_{,\varphi\varphi}(\bar{\varphi})\right) \, \delta\varphi(\boldsymbol{x}) \mapsto -\left(k^2 + a^2 V_{,\varphi\varphi}(\bar{\varphi})\right) \, \delta\varphi(\boldsymbol{k}), \tag{5.46}$$

leading to a simple algebraic equation which can be solved for the Fourier modes $\delta\varphi(\boldsymbol{k})$. Transforming back to position space yields the field $\delta\varphi(\boldsymbol{x})$. Before the final transform is performed, one can also obtain the gradient of $\delta\varphi$ in Fourier space according to $\mathrm{i}\boldsymbol{k}\delta\varphi(\boldsymbol{k}) \mapsto \boldsymbol{\nabla}\delta\varphi(\boldsymbol{x})$. In our simulation, the fields $\delta\varphi(\boldsymbol{x})$ and $\boldsymbol{\nabla}\delta\varphi(\boldsymbol{x})$ are realized on a discrete grid. The discrete transforms are efficiently performed by virtue of a fast Fourier transform (FFT) routine (Frigo and Johnson, 2005).

At this point, we need to discuss a caveat of the method described above. In fact, we have not linearized the equation completely, since the perturbation of the neutrino energy–momentum tensor δT implicitly depends on $\delta\varphi$ due to the cosmon–depending neutrino mass $m_\nu(\varphi) \propto \exp(-\beta\varphi)$. As already mentioned in Sec. 5.1, this dependence is expected to give rise to important backreaction effects and we have warned against linearizing in $\beta\delta\varphi$. As a first approach, we may use

the neutrino masses of the previous time step in order to compute the source term on the right–hand side of Eq. (5.42). As long as the time steps are chosen small enough, this procedure is not expected to produce large errors. However, even small errors may accumulate and systematically lead to a wrong evolution. Alternatively, one may attempt to apply non–linear methods to Eq. (5.42). For instance, one could discretize the Laplacian and search for the solution $\delta\varphi(\boldsymbol{x}_i)$ using Newton's method. This would have to be done at each time step. Due to the large number of cells (typically 256^3) this method becomes numerically intractable; more elaborate methods are necessary.

As a compromise, our simulation method employs an iterative scheme building on the simple Fourier method: Starting from an estimate of the particle masses $\{M_\nu^{(0)}\}$ at a given instant of time (e. g. the particle masses from the previous time step), we solve Eq. (5.42) by virtue of the DFT as explained above. The solution $\delta\varphi^{(1)}(\boldsymbol{x})$ is then used to update the neutrino masses, $M_\nu^{(1)}(\boldsymbol{x}) = M_\nu[\bar{\varphi}, \delta\varphi^{(1)}(\boldsymbol{x})]$, and the perturbation $\delta T(\boldsymbol{x})$. These steps can be repeated as often as desired:

$$M_\nu^{(0)}[\bar{\varphi}, \delta\varphi^{(0)}(\boldsymbol{x})] \mapsto \delta\varphi^{(1)}(\boldsymbol{x}) \mapsto M_\nu^{(1)}[\bar{\varphi}, \delta\varphi^{(1)}(\boldsymbol{x})] \mapsto \cdots \mapsto \delta\varphi^{(n)}(\boldsymbol{x}). \tag{5.47}$$

If this iteration converges, the fixed point $\delta\varphi^{(\infty)}(\boldsymbol{x})$ is necessarily the true solution of Eq. (5.42). With this strategy and a few iteration steps ($n \sim 10$) we achieve good results until $z = 1$. For later times, the sequence does not seem to converge and we therefore decide to stop our simulation.

Asking which factors influence the convergence behavior of the iteration (5.47), it is instructive to study an idealized configuration of only one dense structure of mass M and physical size R in the simulation volume (see Ayaita et al., 2012b). As a result, very large concentrations M/R hinder the convergence of $\delta\varphi^{(n)}$. This is clearly a drawback of the scheme we have chosen. Nonetheless, it allows us for the first time to investigate the nonlinear evolution of GNQ including all of its major effects until $z = 1$. As we will see in Chapter 6, this already reveals a rich phenomenology of the model. Further, we will find that almost all neutrinos are bound to approximately spherically symmetric lumps at $z = 1$. This may open the possibility to employ an effective (and hopefully much simpler) description for studying the further evolution until $z = 0$ (we will also comment on this idea in subsequent chapters).

5.4 Matter and gravity

In this section, we outline the treatment of matter particles and the computation of the gravitational potentials Ψ and Φ. Many aspects are similar to what we have discussed in the context of neutrino particles (Sec. 5.2) and cosmon perturbations (Sec. 5.3).

5.4.1 N–body treatment of matter

As already mentioned, we describe the matter component with N_m effective N–body particles. Matter is not coupled to any other species in our model, therefore

its dynamics are fully described by gravity and the motion of particles follows the standard geodesic equation

$$\frac{\mathrm{d}u^\alpha}{\mathrm{d}\tau} + \Gamma^\alpha_{\rho\sigma} u^\rho u^\sigma = 0. \tag{5.48}$$

In contrast to neutrinos, we may assume $\boldsymbol{v}^2 \ll 1$. Consequently, $\gamma \approx 1$ and $u^0 = \mathrm{d}\eta/\mathrm{d}\tau \approx a(1+\Psi)$. Since $\boldsymbol{u} = u^0 \boldsymbol{v}$, we also have $\boldsymbol{u}^2 \ll 1$. With these approximations and after inserting the relevant Christoffel symbols, the equation of motion takes the simple and intuitive form

$$\frac{\mathrm{d}\boldsymbol{v}}{\mathrm{d}\eta} = -\boldsymbol{\nabla}\Psi - \mathcal{H}\,\boldsymbol{v}. \tag{5.49}$$

For the time integration, we use the same scheme as for the neutrino particles (cf. Sec. 5.2.2) with the difference that we evolve $\boldsymbol{v}$ directly instead of first updating $\boldsymbol{u}$. The latter was necessary to robustly respect the speed of light limit for relativistic neutrinos.

The initial configuration of matter particles is generated analogously to the procedure presented for neutrinos (Sec. 5.2.3). The fact that thermal velocities are negligible for matter allows us to approximate the initial phase space distribution function as

$$f_m(x^i, v_j) = \frac{N_m}{V}\,\delta^3(\boldsymbol{v} - \boldsymbol{v}_m^{\mathrm{pec}}(\boldsymbol{x}))\,(1 + \delta_m(\boldsymbol{x})). \tag{5.50}$$

The random fields $\delta_m(\boldsymbol{x})$ and $\boldsymbol{v}_m^{\mathrm{pec}}(\boldsymbol{x})$ are drawn at redshift $z_i = 49$, at which we start the N–body treatment of matter. The coefficients $\tilde{\alpha}_i$ used for the realization of initial random fields are the same as for the neutrinos. Until neutrino particles are added, matter evolves under the influence of gravity on a GNQ background.

5.4.2 Computation of Ψ and Φ

The gravitational potentials Ψ and Φ are related to the perturbations of the total energy–momentum tensor by virtue of the linearized Einstein equations (cf. Sec. 3.3.1). It is most convenient to solve these equations in Fourier space. As mentioned before, metric perturbations are treated linearly and we assume that time derivatives are small compared to spatial variations.

The Poisson equation (3.29) expresses $\Phi(\boldsymbol{k})$ in terms of the density perturbation $\delta\rho = \sum_s \delta\rho_s$, with $s \in \{m, \nu, \varphi\}$ labelling the relevant species and $\delta\rho_s(\boldsymbol{x}) = \rho_s(\boldsymbol{x}) - \bar{\rho}_s$ as usual. The contribution of the cosmon field to linear order in $\delta\varphi$ is given by

$$\delta\rho_\varphi = \frac{\bar{\varphi}'\,\delta\varphi}{a^2} + V_{,\varphi}(\bar{\varphi})\,\delta\varphi. \tag{5.51}$$

The neutrino and matter density perturbations need to be obtained from the distribution of the effective N–body particles. As described in Sec. 5.2.4, the energy–densities $\rho_\nu(\boldsymbol{x})$ and $\rho_m(\boldsymbol{x})$ follow by summing up one–particle contributions (Eq. 5.34, with $\gamma = 1$ for matter particles). The averaged neutrino energy–density $\bar{\rho}_\nu$ is given by Eq. (5.37); the analogue expression for matter implies the familiar result $\bar{\rho}_m \propto a^{-3}$, which can be used instead. We have now collected all contribu-

tions to the perturbation field $\delta\rho(\boldsymbol{x}) = \sum_s \delta\rho_s(\boldsymbol{x})$. Hence, by virtue of the Fourier transform and Eq. (3.29), we can calculate $\Phi(\boldsymbol{k})$.

Next, we consider $\Psi(\boldsymbol{k})$. The difference between the two potentials is sourced by anisotropic stress (cf. Eq. 3.30). In our situation, we only need to account for the contribution from relativistic neutrinos. The anisotropic stress $\Sigma^i{}_j$ associated with the one–particle energy–momentum tensor, Eq. (5.13), is given by

$$\Sigma^i{}_j = T^i{}_j - \frac{1}{3}\delta^i_j\, T^k{}_k \tag{5.52}$$

$$= \frac{1 - 2\Psi - 2\Phi}{\sqrt{\tilde{g}}}\gamma M_\nu \left(v^i v_j - \frac{\boldsymbol{v}^2}{3}\right)\delta_D^3(\boldsymbol{x} - \boldsymbol{\xi}). \tag{5.53}$$

The factor $(1-2\Psi-2\Phi)$ appears due to the definition of the peculiar velocity $\boldsymbol{v}$ with respect to comoving coordinates and conformal time. The total shear field is the sum of the contributions from all neutrino particles. The scalar perturbation Σ is obtained by a suitable projection in Fourier space (see Ma and Bertschinger, 1995; Ayaita et al., 2012b). Using the previously calculated potential $\Phi(\boldsymbol{k})$, we obtain $\Psi(\boldsymbol{k})$ from Eq. (3.30). At this point, it is also advisable to store the coefficients of the gradients $-\mathrm{i}\boldsymbol{k}\Phi(\boldsymbol{k})$ and $-\mathrm{i}\boldsymbol{k}\Psi(\boldsymbol{k})$. Finally, transforming back to position space results in the fields $\Psi(\boldsymbol{x})$ and $\Phi(\boldsymbol{x})$, together with $\boldsymbol{\nabla}\Psi(\boldsymbol{x})$ and $\boldsymbol{\nabla}\Phi(\boldsymbol{x})$.

Two comments are in order here. First, we have, for convenience, assumed continuous positions $\boldsymbol{x}$ and Fourier modes $\boldsymbol{k}$ above. As explained in previous sections, we actually perform a discrete transform. The discretized values $\delta\rho(\boldsymbol{x}_i)$ and $\Sigma(\boldsymbol{x}_i)$ are obtained by collecting all particles contained in the corresponding cell. Second, the computation of $\rho_\nu(\boldsymbol{x})$ and $\Sigma^i{}_j(\boldsymbol{x})$ already involves the potentials Φ and Ψ (in sub–leading order). We circumvent this problem by approximating the values of the potentials, only for this purpose, by the results of the previous time step. For small, slowly–varying potentials and not too large time steps this is an adequate approximation.

5.5 Runtime and resolution

The simulation method described in Secs. 5.2 to 5.4 has been implemented in the programming language `C++`. As discussed in Sec. 5.3.2, it is successful until $z = 1$, where we stop our simulation. In each time step, the code has to perform several Fourier transforms (cf. Secs. 5.3 and 5.4) and summations over all particles (see, e. g., Eqs. 5.37 and 5.39). In order to keep runtime short, we use parallel programming for these steps (and wherever it is possible). This is achieved by virtue of the libraries OPENMP and FFTW (Frigo and Johnson, 2005). Running on a present–day eight–core processor, the wall–clock time amounts to a couple of days and hence poses no serious problem.

We also need to address the issue of resolution. The dynamical fields $\Psi(\boldsymbol{x})$, $\Phi(\boldsymbol{x})$, and $\delta\varphi(\boldsymbol{x})$ entering the equations of motion, Eqs. (5.11) and (5.49), are realized on a grid whose resolution is limited by the finite cell size $\Delta x = L/N_c^{1/3}$. Indeed, modern CDM simulations sum up two–body forces in a highly efficient scheme and thereby obtain an excellent resolution even on small scales (e. g., GADGET–2, Springel 2005).

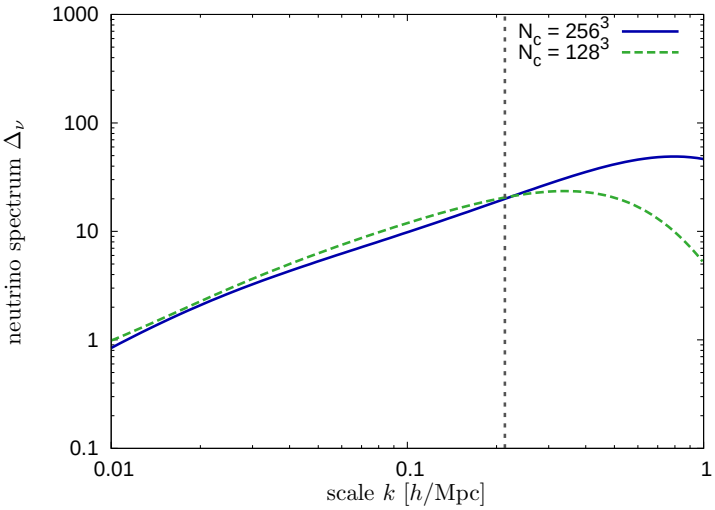

Figure 5.3: The neutrino spectrum $\Delta_\nu(k)$ at $z = 1$ for two different resolutions. $N_c = 256^3$ corresponds to our standard choice. The vertical dashed line marks the scale $1/\Delta x^{(\mathrm{low})}$.

However, in the model under consideration, nonlinear structure formation is not a purely small–scale phenomenon. In contrast, our primary interest is in neutrino clustering which is expected to be dominant on large scales (Mota et al., 2008). We study the influence of our limited resolution on neutrino clustering by running a simulation with a lower resolution, $N_c^{(\mathrm{low})} = 128^3$. The size of a grid cell is twice as big as for the standard resolution, $\Delta x^{(\mathrm{low})} = 2\Delta x$. Apart from N_c, we choose all other parameters as in Tab. 5.1 and start the simulation from the same realization of the initial random fields. In Fig. 5.3, we show for both resolutions the dimensionless neutrino power spectrum $\Delta_\nu(k)$, defined via

$$\Delta_\nu^2(k) = \frac{k^3}{2\pi^2} P_\nu(k), \tag{5.54}$$

at redshift $z = 1$ (P_ν is the usual spectrum of the neutrino density contrast δ_ν). As expected, the reduction of N_c leads to a loss of power on small scales. On the other hand, we find satisfying agreement on large scales, $k \lesssim 1/\Delta x^{(\mathrm{low})}$. Later, we will also study individual neutrino structures (Sec. 6.2), where the resolution of length scales below the size of a lump is more important. On a quantitative level, these results will be more affected by the limited resolution; we will again use the low–resolution run in order to quantify the effect (qualitatively, we obtain a robust picture). Of course, our method is not accurate enough for a precision study of matter clustering. When we investigate the growth of matter fluctuations in GNQ, we will compare the results to a pure CDM simulation with the same accuracy in order to single out the effect of neutrino clustering (Sec. 6.3).

As an option, our implementation also allows to use the so–called "cloud–in–a–cell" (CIC) interpolation scheme which is an attempt to slightly improve the

small–scale resolution by distributing particles over the nearest 8 grid cells instead of assigning each particle to the closest grid point only (see, e. g., Dolag et al., 2008; Bagla and Padmanabhan, 1997). The scheme also interpolates forces to sub–grid scales. While this method clearly increases the computation time, we have, however, not found striking improvements. In the long run, significant refinements in the resolution, e. g. by using an adaptive mesh, are certainly possible. At the current stage, this does not seem to be urgent and we thus keep the method as simple as possible.

6 Simulation Results

In the previous chapter, we have presented a comprehensive simulation method for studying nonlinear neutrino clustering and its cosmological implications in the framework of GNQ. In the following we will show and discuss the results of a simulation run from redshift $z_i = 4$ to $z_f = 1$ (for the numerical specifications, see Tab. 5.1). The quantitative outcome of course depends on the chosen model parameters. We use the values listed in Tab. 6.1. This set of parameters has been motivated by investigating the background evolution and requiring a viable expansion history similar to ΛCDM (Amendola et al., 2008); this choice also corresponds to the studies of Mota et al. (2008) and Baldi et al. (2011). As we have already pointed out in Chapter 5, we expect nonlinear neutrino perturbations to give rise to strong backreaction effects on the evolution of the cosmological background (cf., e. g., Fig. 5.2). Taking into account these effects will probably require some adjustments of the parameters. Although it goes beyond the scope of this work to explore the full parameter space of GNQ, we will obtain an insightful picture of the phenomenology of the model at the nonlinear level and will show up effects that might become decisive for scrutinizing the model. In Sec. 6.1, we will follow the formation of neutrino structures. Parallel to the evolution of the density field, we study the growth of neutrino velocities and investigate the properties of the gravitational potentials Ψ and Φ. A closer look at individual neutrino structures will be taken in Sec. 6.2. The subsequent section is dedicated to the impact on matter perturbations (Sec. 6.3). Most of the results we are going to present are part of the publication Ayaita et al. (2012b).

Specification	*Parameter value*
Coupling constant	$\beta = -52$
Present averaged neutrino mass	$m_\nu^0 = 2.3$ eV
Parameter of the cosmon potential	$\alpha = 10$
Present neutrino density parameter	$\Omega_\nu^0 = 0.15$
Present dark energy density parameter	$\Omega_\varphi^0 = 0.60$
Present Hubble parameter	$H_0 = 70$ km/s Mpc^{-1}
Scalar amplitude ($k_{\mathrm{pivot}} = 0.05$ Mpc^{-1})	$A_s = 2.3 \times 10^{-9}$
Spectral index	$n_s = 0.96$

Table 6.1: Exemplary model parameters used in the simulations. The values m_ν^0, Ω_ν^0, and Ω_φ^0 do not take into account backreaction effects (the model parameters are specified by the properties of the homogeneous background solution). The present matter density Ω_m^0 follows from the flatness condition (neglecting radiation at late times).

6.1 Neutrino clustering

The formation of stable nonlinear neutrino lumps has been predicted by several studies (e. g., Brouzakis et al., 2008; Wintergerst et al., 2010; Baldi et al., 2011). Our method allows us to follow the growth of neutrino density perturbations over time, starting from linear initial fluctuations (Sec. 6.1.1). During this process, neutrino velocities grow under the influence of the cosmon–mediated fifth force. As we will see in Sec. 6.1.2, this implies a considerable increase of the averaged neutrino equation of state w_ν. The gravitational potentials are covered in Sec. 6.1.3.

6.1.1 Formation of nonlinear structures

Figure 6.1 shows snapshots of the evolution of neutrino inhomogeneities in our simulation box. In the beginning of the evolution, perturbations are still small and the large–scale neutrino distribution is close to homogeneous. For this reason, the first two figures (for $a = 0.25$ and 0.3) show a spherical section through the simulation volume visualizing small fluctuations in the number density $n_\nu(\boldsymbol{x})$ on its surface. On closer inspection, the growth of perturbations is already visible. It can still be described by linear perturbation theory at this stage. Shortly thereafter, however, neutrino perturbations enter the nonlinear regime (in agreement with Mota et al., 2008).

In the subsequent figures, the blue color marks regions where the local neutrino number density $n_\nu(\boldsymbol{x})$ exceeds the threshold $5\,\bar{n}_\nu$. At $a = 0.35$, we can identify overdense regions that have emerged from the initial seed of perturbations. In the course of the evolution, they start to collapse and form large filament–like nonlinear structures ($a = 0.4$). The concentration of neutrinos in structures is accompanied by the formation of large voids in the simulation box. Eventually, we can identify separated lumps at $a = 0.45$. Until $a = 0.5$, most of these lumps have evolved almost spherical shapes. The number density $n_\nu(\boldsymbol{x})$ locally reaches values of the order 10^5 times the averaged number density $\bar{n}_\nu$; the neutrinos have formed highly nonlinear structures.

At $a = 0.5$ ($z = 1$), we need to stop our simulation (cf. Sec. 5.3.2). Thus, the further evolution is subject to speculation. The observed spherical shapes can be interpreted as a sign of virialization, as predicted by the hydrodynamic study of single idealized overdensities (Wintergerst et al., 2010). Consequently, one may hope that, after a period of rapid neutrino clustering between $a = 0.35$ and $a = 0.5$, the overall picture remains stable: a collection of virialized, highly concentrated neutrino structures. This opens the possibility that the further evolution of the model can be understood from studying an effective "fluid" consisting of neutrino lumps (we will address the issue of stability and investigate the intrinsic equation of state of such lumps in Chapter 7). In Fig. 6.2, we give an impression of the distribution of lumps expected in a comoving volume of size H_0^{-3}. For this purpose, we have run a series of 20 simulations starting from different realizations of the initial random fields; the resolution was reduced in order to shorten the runtime (the large–scale results are expected to be robust, see Sec. 5.5). The figure shows the estimated abundance $N(f_\nu \geq f)$ of lumps for which the number of bound neutrinos f_ν (relative to the total number of neutrinos in the Hubble volume) exceeds some

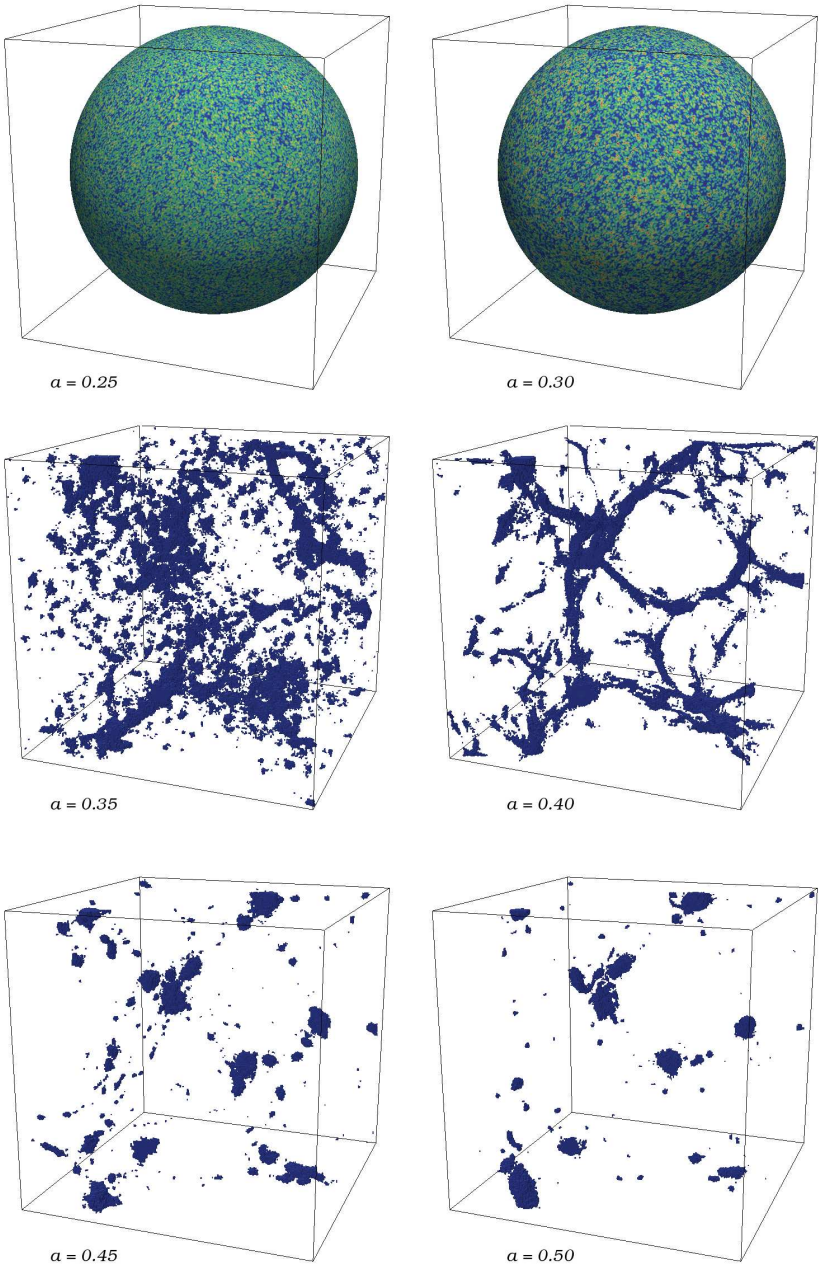

Figure 6.1: Neutrino clustering in the simulation box of size $L = 600\,h^{-1}$Mpc. The lower four figures show regions where the number density of neutrinos $n_\nu(\boldsymbol{x})$ is at least a factor of 5 higher than the background value $\bar{n}_\nu$. We observe the growth of perturbations from linear fluctuations to nonlinear, separate structures of almost spherical shapes. The upper figures show a two–dimensional section of the number density field (the color range goes from 0 (blue) to 5 (red) times the background value).

threshold f (the results have been scaled by the ratio of the simulation volume to the Hubble volume). The total number of lumps is of order 10^3 and the abundances rapidly decrease for $f > 10^{-3}$. Our results suggest that almost all neutrinos in the Hubble volume are bound to some lump. We will now continue with our discussion of the evolution for $z \leq 1$.

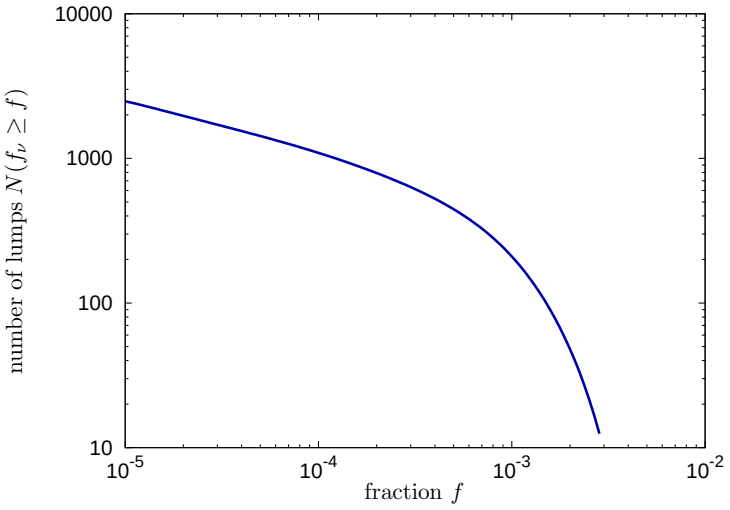

Figure 6.2: Estimated distribution of neutrino lumps in a comoving volume equal to the present Hubble volume H_0^{-3}. A lump is characterized by the quantity f_ν expressing the number of neutrinos bound to the structure relative to the total number of neutrinos in the Hubble volume. The abundance $N(f_\nu \geq f)$ is the expected number of lumps with $f_\nu \geq f$. The lumps have been counted at redshift $z = 1$ and we have used a combination of 20 independent simulation runs for this application.

6.1.2 Relativistic velocities

In this section, we concentrate on the evolution of neutrino velocities. We have chosen a relativistic treatment of the neutrino dynamics (cf. Sec. 5.2.1) which remains valid even for velocities close to the speed of light. This was motivated by the breakdown of the Newtonian approximation in previous attempts. The relevance of relativistic dynamics can be highlighted by counting the number of particles with velocities v above a considerable fraction of the speed of light (Baldi et al., 2011). As illustrated in Fig. 6.3, the major part of neutrinos in our simulation reaches relativistic velocities above $0.5\,c$ at $z = 1$. The acceleration is particularly strong during the phase of nonlinear clustering, $z < 2$ ($a > 0.33$).

In order to give a more detailed description, we estimate the velocity distribution function $F_\nu(v)$ at different instants of time by grouping the effective N–body particles into bins according to the magnitude of their velocities. The normalized distribution functions ($\int_0^1 \mathrm{d}v\, F_\nu(v) = 1$) are shown in Fig. 6.4. At $a = 0.25$ and $a = 0.30$, neutrino velocities are typically below 10% of the speed of light. At this stage of the evolution, perturbations are still small and the distribution of velocities

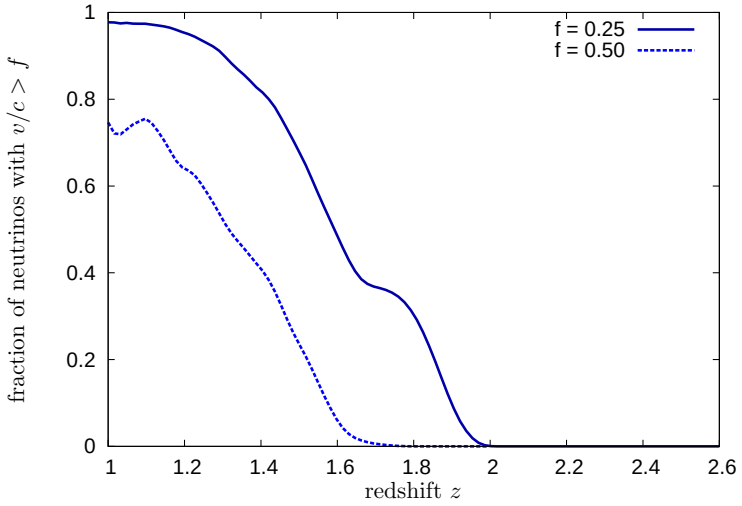

Figure 6.3: The fraction of neutrinos with velocities $v/c > 0.25$ and $v/c > 0.5$, respectively.

is governed by thermal velocities. The growth of the background neutrino mass explains the decrease of the mean neutrino velocity from $a = 0.25$ to $a = 0.30$. As already anticipated above, the velocities start to grow once nonlinear clustering sets in. Between $a = 0.3$ and $a = 0.45$, neutrino particles are considerably accelerated by the strong fifth force; the mean velocity at $a = 0.45$ is around $0.5\,c$. Some few particles have even entered the highly relativistic regime, $v > 0.9\,c$. The acceleration continues until $a = 0.5$.

Large neutrino velocities are also expected to become visible in the averaged equation of state $w_\nu = \bar{P}_\nu/\bar{\rho}_\nu$. This parameter is of great cosmological relevance. The necessary averages are calculated from the distribution of N–body particles according to Eqs. (5.37) and (5.38). We show the evolution of w_ν in Fig. 6.5 together with the result obtained from a standard background calculation neglecting backreaction. While the simulation perfectly agrees with the background calculation at early times $z > 2.5$, we observe a striking discrepancy at more recent redshifts. The steep increase of w_ν over several orders of magnitude between $z = 2.5$ ($a \approx 0.29$) and $z = 1$ ($a = 0.5$) reflects the rapid growth of neutrino velocities during this phase (cf. Figs. 6.3 and 6.4). At $z = 1$, the averaged neutrino equation of state exceeds 0.1. This is in stark contrast to the non–relativistic value $w_\nu \lesssim 10^{-5}$ expected within the homogeneous approximation.

In order to understand the discrepancy, one has to bear in mind that the homogeneous calculation does not involve the accelerating fifth force mediated by fluctuations in the cosmon field $\delta\varphi(\boldsymbol{x})$. Instead, the neutrino temperature T_ν continuously cools down due to the cosmic expansion, while the neutrino mass $m_\nu = m_\nu(\bar{\varphi})$ follows oscillations of the background cosmon field $\bar{\varphi}$ around the minimum of its effective potential (Wetterich, 2008). Hence, apart from oscillatory features, the quotient T_ν/m_ν inevitably decreases in time.

The actual evolution of w_ν reveals a strong backreaction effect on the background

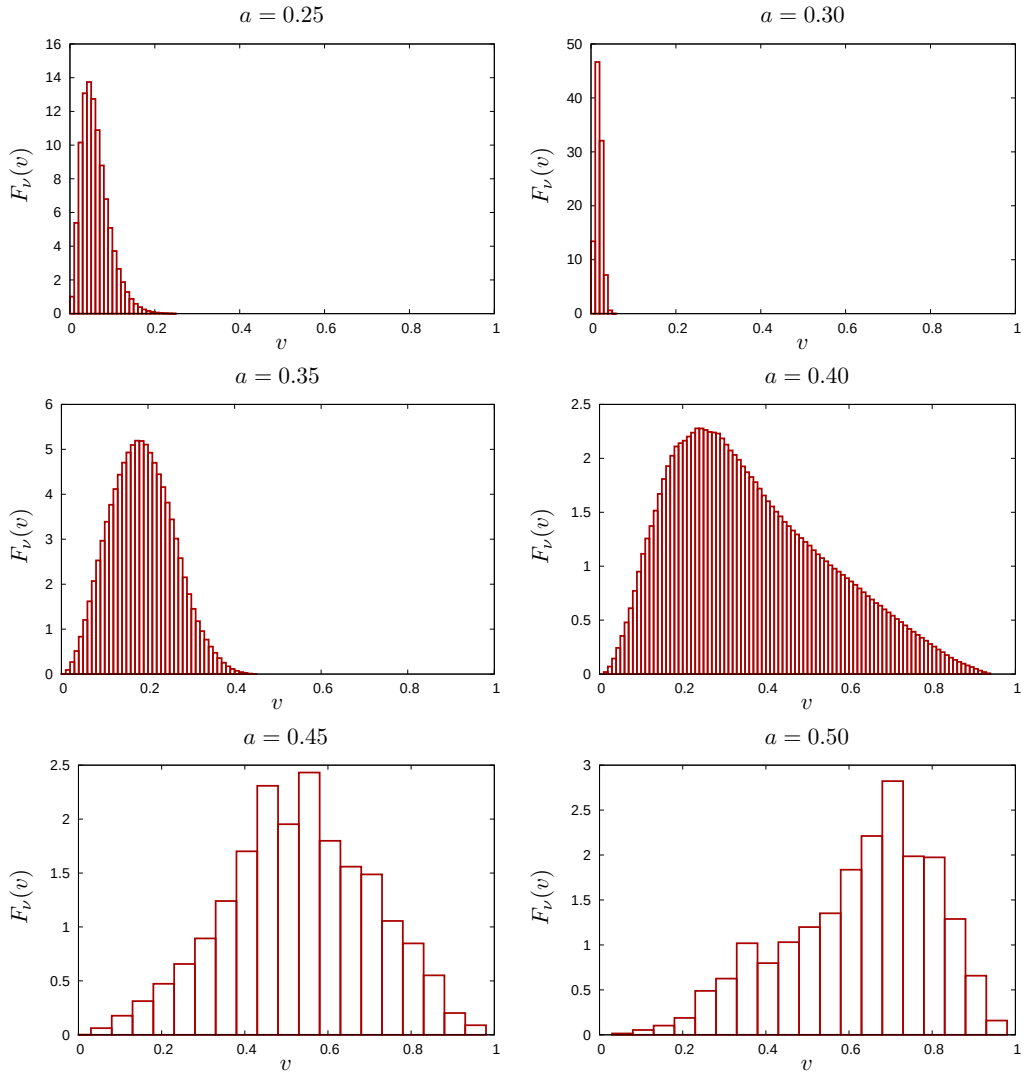

Figure 6.4: The distribution of neutrino velocities in our simulation for different stages of the evolution. Between $a = 0.25$ and $a = 0.3$, neutrino velocities are small, typically $v < 0.1\,c$. During the course of the evolution, the velocities grow and reach relativistic values. The bin width is $0.01\,c$ in the upper figures and $0.05\,c$ in the two lowermost figures.

evolution of neutrinos. As a direct consequence of energy–momentum conservation (applied to the coupled cosmon–neutrino fluid), the effect carries over to the evolution of the background cosmon field $\bar{\varphi}$. We emphasize that the neutrino's capability of stopping the evolution of the cosmon is essentially expressed by the quantity $\bar{T}$ (cf. Eq. 5.41). As we have already anticipated in Sec. 5.2.4, nonlinear neutrino clustering can considerably reduce the value of $\bar{T}$ due to local mass suppressions and relativistic Lorentz factors $\gamma > 1$. Indeed, both effects are significant in our simulations (see Sec. 6.2 for local mass variations). A more detailed investigation of the backreaction effect on the evolution of $\bar{\varphi}$ (see Ayaita et al., 2012b) reveals

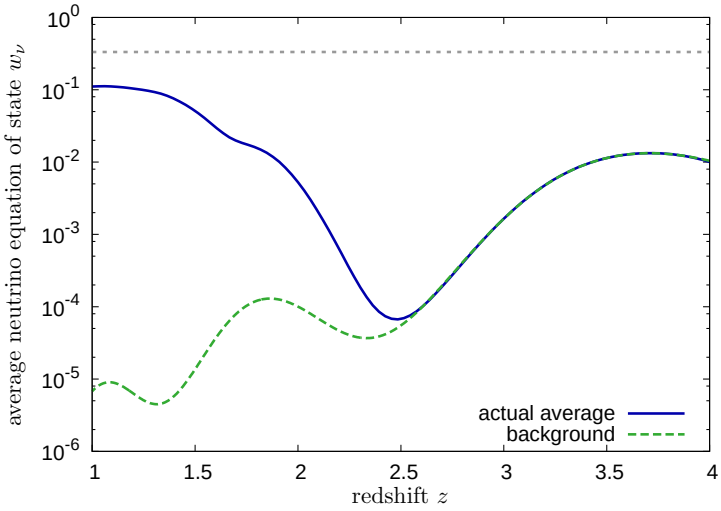

Figure 6.5: The increase of the equation of state w_ν due to relativistic velocities. The dashed horizontal line marks the limit $w = 1/3$ for ultra–relativistic particles.

that the dark energy equation of state w_φ at redshifts $z < 1.5$ is further away from $w_\Lambda = -1$ as would be expected from a homogeneous background calculation; this suggests that the onset of accelerated expansion will at least shift to later times.

Relativistic velocities also play an important role in connection with anisotropic stress $\Sigma^i{}_j$, which determines the difference between the gravitational potentials Ψ and Φ. This will be interesting in the next section.

6.1.3 The gravitational potentials Ψ and Φ

With the tools presented in Sec. 5.4.2, we are in the position to calculate the gravitational potentials $\Psi(\boldsymbol{x})$ and $\Phi(\boldsymbol{x})$. They are not only needed to accelerate particles in our simulation (Secs. 5.2 and 5.4), but are also of particular interest in their own right (cf. Chapter 4). For instance, the ISW and WL both arise from perturbations to the propagation of photons through (time varying) gravitational potentials, which leaves observable traces in the CMB spectra or galaxy shear surveys. Concerning the large–scale regime, particularly the 3D version of WL is promising to provide valuable constraints (cf. Secs. 4.2 – 4.4). Previously, we have identified a phase of rapid neutrino clustering between $z \lesssim 2.5$ and $z = 1$. During this time, both, neutrino density contrasts and neutrino velocities, significantly grow with intriguing implications for the gravitational potentials.

Let us first focus on the presence of relativistic neutrino velocities. A peculiar effect associated with relativistic motion concerns the difference between the two potentials Ψ and Φ. It is determined by the anisotropic stress tensor $\Sigma^i{}_j$, which is of order $\boldsymbol{v}^2$ (cf. Sec. 5.4.2). Comparing the fields $\Psi(\boldsymbol{x})$ and $\Phi(\boldsymbol{x})$ in our simulation volume at a given time, we detect a non–vanishing difference $(\Phi - \Psi)$ in the vicinity of neutrino lumps; it however becomes negligible on large scales. For illustration, we show the neutrino number density field $n_\nu(\boldsymbol{x})$ and the field $(\Phi - \Psi)(\boldsymbol{x})$ on

an exemplary two–dimensional slice through our simulation volume at $z = 1$ in Fig. 6.6. The number density field allows one to identify the position of neutrino structures; a rather pronounced one is located in the upper left corner of the slice. At the same position, we observe an anisotropic pattern in the field $(\Phi - \Psi)$ with an amplitude of the order 10^{-5} (roughly 1 – 10% of the local potentials Φ and Ψ themselves). Similar anisotropic patterns are visible in the regions of smaller overdensities. The figure also shows that the magnitude of the difference $(\Phi - \Psi)$ is substantially smaller in the space between separated structures. The anisotropic patterns of $\Phi - \Psi$ represent a characteristic feature of neutrino lumps with intrinsic relativistic motion. Regarding large scales (compared to the typical size of neutrino structures), we conclude that the assumption $\Psi = \Phi$ is still a good approximation.

We will now analyze the quantitative evolution of $\Psi(k)$ on large scales. This is especially relevant for the evolution of matter perturbations and also for the ISW. The latter is sensitive to the sum $(\Phi + \Psi)'$ (cf. Eq. 4.4) which specializes to approximately $2\Psi'$ on large scales. Note that $\Psi(k)$ denotes the square root of the dimensionless spectrum,

$$\Psi^2(z,k) = \frac{k^3}{2\pi^2} P_\Psi(z,k), \tag{6.1}$$

assuming the usual definition of the power spectrum $P_\Psi(z,k)$ (see Eq. 3.36). The quantity $\Psi(z,k)$ is a measure for the expected fluctuation of the gravitational potential in volumes of size $\approx (\pi/k)^3$.

The main difference to ΛCDM occurs due to the presence of nonlinear neutrino perturbations on large scales. Indirectly, they also amplify the growth of matter perturbations (cf. Sec. 6.3). In order to quantify the total effect of neutrino clustering on the gravitational potential, we compare our results to the case where matter grows only due to its own gravitational potential. For this purpose, we run a modified simulation that evolves only matter (and gravity) on an unperturbed GNQ background. For the chosen set of parameters (Tab. 6.1), the expansion history is very similar to the ΛCDM concordance model. Accordingly, we use the label $\Psi^{\Lambda\mathrm{CDM}}$ for the gravitational potential obtained from this run. We make sure that the matter evolution in the "ΛCDM" simulation starts from the same initial random field as in the original GNQ simulation. For two exemplary scales, we plot the evolution of the quotient $\Psi(k)/\Psi^{\Lambda\mathrm{CDM}}(k)$ in Fig. 6.7. The impact of neutrino clustering is clearly visible at redshifts $z \lesssim 2$. For $k = 0.02\,h/\mathrm{Mpc}$, the gravitational potential is almost an order of magnitude larger than the matter induced gravitational potential in the ΛCDM simulation. The effect is somewhat weaker but still pronounced for the smaller scale, $k = 0.05\,h/\mathrm{Mpc}$. The absolute amplitude of the large–scale potential at $z = 1$ lies between 10^{-5} and 10^{-4} in our simulation.

Large magnitudes of the gravitational potentials may have an important impact on weak shear spectra. Moreover, the steep increase of the gravitational potentials contributes to the ISW. In the standard ΛCDM model, the large–scale gravitational potentials are constant during matter domination and slowly start to decay when accelerated expansion sets in. In GNQ, in contrast, we have found a growing magnitude of the large–scale gravitational potentials during the phase of neutrino clustering. If neutrino lumps indeed virialize shortly thereafter, the growth of the gravitational potentials is expected to stop again. Indeed, Fig. 6.7 suggests that

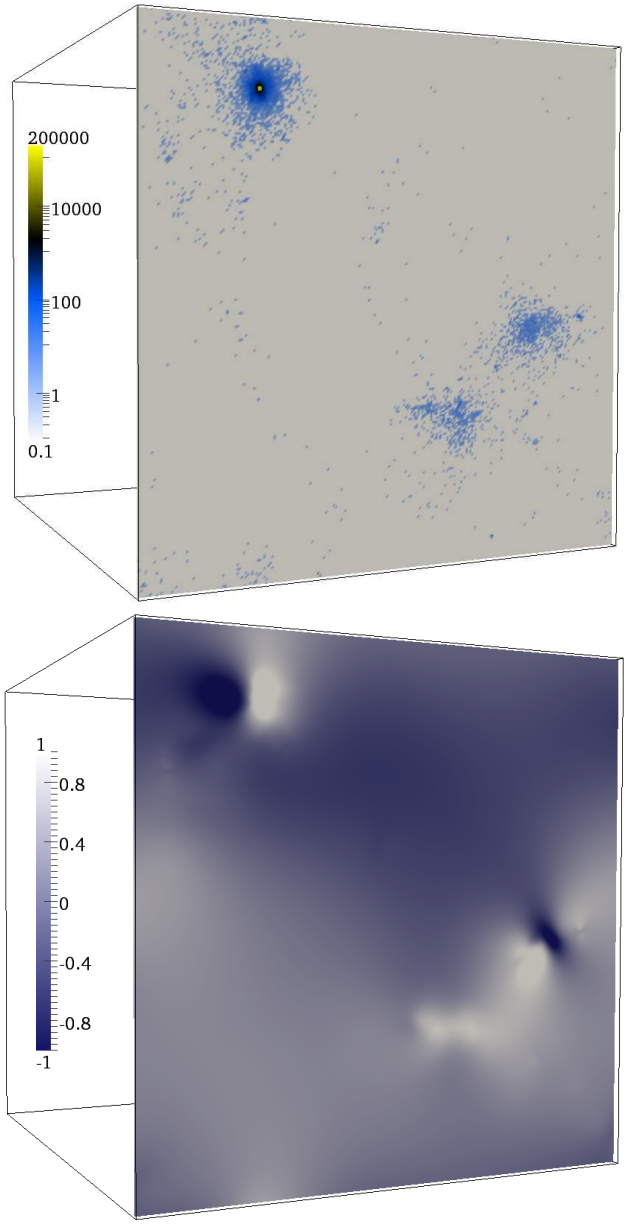

Figure 6.6: The upper figure shows a slice through the neutrino number density field $n_\nu(\boldsymbol{x})$ (in multiples of the average $\bar{n}_\nu$) at $z = 1$. The lower figure visualizes the difference $(\Phi - \Psi)$ of the two gravitational potentials (scaled by a factor of 10^5) on the same slice. Differences between the gravitational potentials are most pronounced in the vicinity of the deep neutrino structure in the upper left corner.

the increase in Ψ slows down around $z = 1$. The onset of accelerated expansion may still lead to decaying gravitational potentials in the subsequent evolution.

The details certainly depend on the choice of model parameters. Generally, the time evolution of the large–scale gravitational potentials in GNQ is more complex

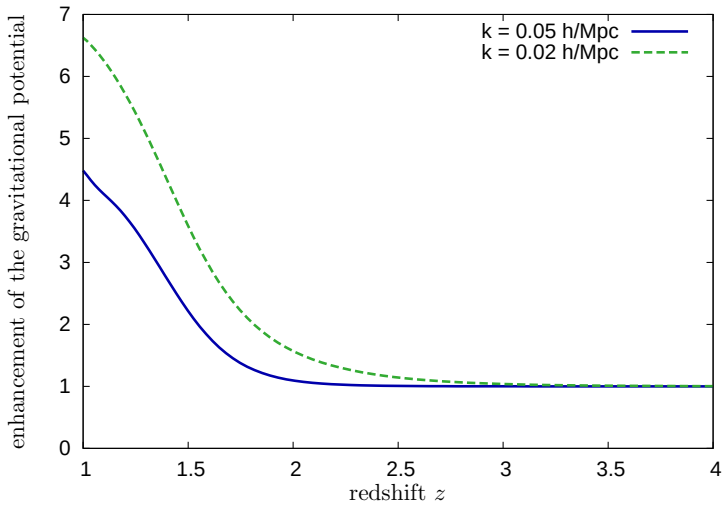

Figure 6.7: The evolution of the quotient $\Psi(z,k)/\Psi^{\Lambda\mathrm{CDM}}(z,k)$ for two different modes $k = 0.05\,h/\mathrm{Mpc}$ and $k = 0.02\,h/\mathrm{Mpc}$. For both scales, a considerable enhancement of the gravitational potential $\Psi(z,k)$ at times $z < 2$ is visible.

than in the standard ΛCDM model. Observables that are sensitive to Ψ and Φ on large scales, like the ISW and WL (especially tomography or 3D weak shear, see Chapter 4), are promising to put stringent constraints on the model parameters once the quantitative analysis can be continued until $z = 0$. Concerning the ISW, measurements of the signal's redshift dependence and the overall effect on the CMB spectrum (see also Pettorino et al., 2010) will complement one another.

6.2 A look inside neutrino lumps

In Sec. 6.1, we have presented the overall evolution of the neutrino density and velocity fields and their impact on the large–scale gravitational potentials. This section, on the contrary, studies the properties of individual neutrino lumps. We are particularly interested in the phenomenon of local neutrino mass variations inside nonlinear structures. For these applications, the resolution of scales inside the lumps is of greater importance. As discussed in Sec. 5.5, the accuracy of our method on these scales is reduced. In particular, we do not resolve the neutrino dynamics below the size of a grid cell, $\Delta x \approx 2\,h^{-1}$ Mpc in comoving units. In order to take this issue into account, we will employ the results of a low–resolution run ($N_c^{(\mathrm{low})} = 128$) to estimate the uncertainties.

6.2.1 Density and mass profiles

In Fig. 6.6, we have shown a slice through the simulation volume at $z = 1$ which was located at the center of a concentrated structure. In order to give a more quantitative impression of this structure, we have measured the neutrino number density in spherical shells around its center. As the lump is almost spherically symmetric,

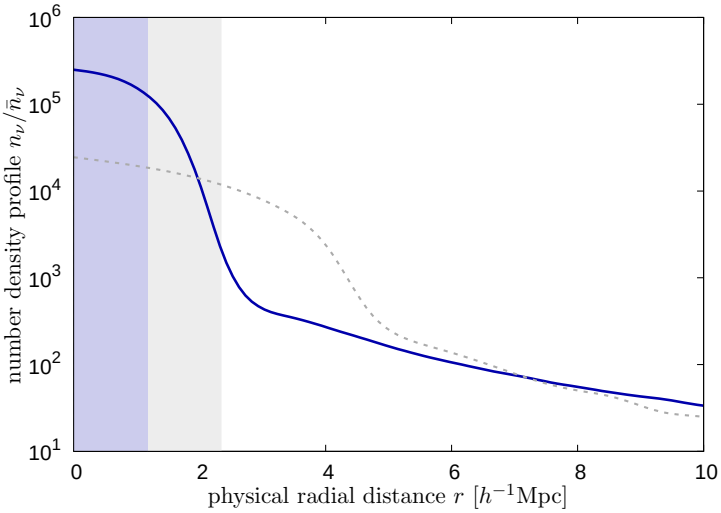

Figure 6.8: The number density profile $n_\nu(r)$ (measured in multiples of the average $\bar{n}_\nu$) of a pronounced neutrino structure. We also show the results from a low–resolution run (dashed line). The shaded regions indicate the size of a grid cell for both resolutions ($\Delta x^{(\mathrm{low})} = 2\Delta x$).

the resulting radial density profile $n_\nu(r)$ (Fig. 6.8) is a useful characteristic of the structure. The distance r is measured in physical units. We identify a concentrated core with a central neutrino number density $n_\nu^{(\mathrm{max})} = 2 \times 10^5\, \bar{n}_\nu$. The innermost core extends to a physical distance of roughly $2\,h^{-1}$Mpc. The number density then quickly drops below $10^3\, \bar{n}_\nu$ but is still considerably above the average value for distances above $10\,h^{-1}$Mpc. The low–resolution run provides a similar shape of the profile, but the quantitative description of the innermost core is strongly affected by the reduced resolution. This is due to the fact that neutrino clustering below the scale of a grid cell (shaded regions in the figure) is suppressed. From this perspective, our estimate of the central neutrino density should be regarded as a lower bound.

Next, we turn to the exciting phenomenon of local neutrino mass variations. In a spherically symmetric neutrino structure, the solution of the perturbed Klein–Gordon equation (5.42) is given by cosmon fluctuations $\delta\varphi(r)$ determining the neutrino mass $m_\nu(r) \propto \exp(-\beta(\bar{\varphi} + \delta\varphi(r))$. We have seen in Sec. 5.3 that the perturbation $\delta\varphi$, in a first approximation, behaves similar to the neutrino induced gravitational potential, $\delta\varphi(r) \approx 2|\beta|\Psi_\nu(r)$. This typically implies $\delta\varphi < 0$, $\exp(-\beta\delta\varphi(r)) < 1$, in overdense regions; the local neutrino mass consequently is suppressed. The full calculation takes into account relativistic corrections and solves Eq. (5.42) by virtue of the strategies discussed in Sec. 5.3.2. We consider the same neutrino structure as above and average the mass of neutrinos in spherical shells around its center. The resulting mass profile $m_\nu(r)$ is presented in Fig. 6.9. We find a considerable neutrino mass suppression inside the lump; the neutrino mass in the center of the structure is roughly one order of magnitude smaller than the neutrino mass at larger distances. This is in concordance with previous esti-

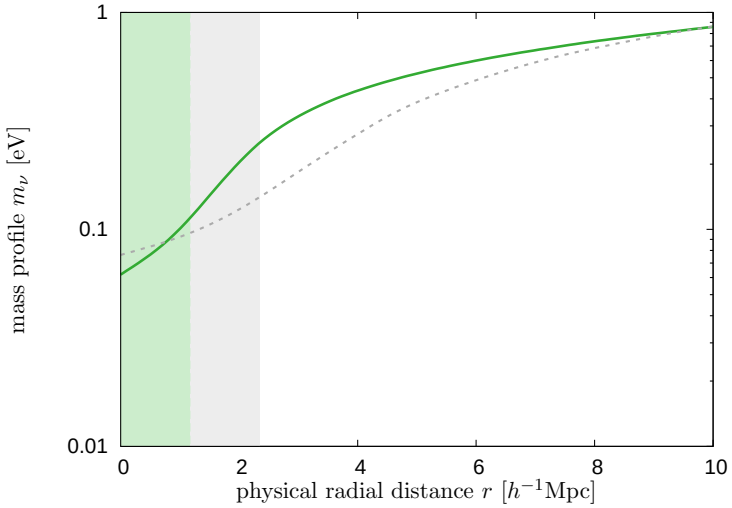

Figure 6.9: The mass profile $m_\nu(r)$ of the structure. As in Fig. 6.8, the dashed line shows the result of the low–resolution simulation and the shaded regions indicate the size of a grid cell. At the center of the structure, the neutrino mass is suppressed by an order of magnitude.

mates (Nunes et al., 2011). Interestingly, the low–resolution run does not deviate significantly. The presented results are typical for concentrated structures in our simulation; with decreasing neutrino concentration, the mass suppression is less pronounced. According to these findings, measurements of the neutrino mass in the Universe can lead to very different results depending on whether they are performed in the region of a neutrino lump or not.

The results of Fig. 6.9 underline the relevance of local cosmon fluctuations. Neglecting these variations, the neutrino mass would be dictated by the background field $\bar{\varphi}$. Oscillations in the background then imply coherent mass oscillations of all neutrinos in the simulation and even carry over to the process of structure formation (cf. Baldi et al., 2011). These pronounced effects do not occur in our simulations. While we still observe oscillations in $\bar{\varphi}$ (with modifications due to backreaction, see Ayaita et al., 2012b), their impact on the local neutrino dynamics is much weaker.

6.2.2 Evolution of an isolated lump

The time evolution of the neutrino density field, as illustrated in Fig. 6.1, shows that distinct neutrino structures are present from $a \approx 0.45$ on. We have followed the evolution of a single isolated lump in the simulation box during the final stage of our simulation. Changes in the number density profile of the structure are shown in Fig. 6.10. We observe a moderate transfer of neutrinos from the outer shells of the structure to the inner core between $a = 0.45$ and $a = 0.5$. Apart from that, the profile appears stable. This can be regarded as another hint towards virialization. We have chosen an isolated lump, since other structures still undergo merging processes. For virialized lumps it is expected that the mass profile freezes

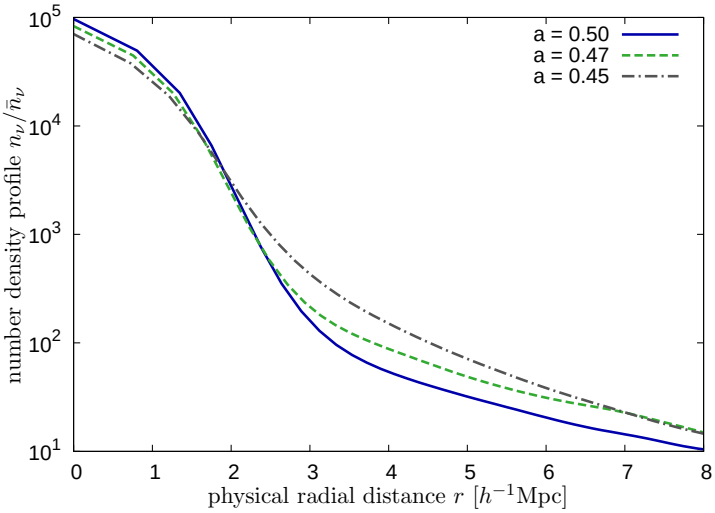

Figure 6.10: The figure visualizes changes in the number density profile $n_\nu(r)$ of an isolated neutrino structure between $a = 0.45$ and $a = 0.5$.

and becomes independent of the evolution of the background field $\bar{\varphi}$ (Nunes et al., 2011). Thus, if virialization indeed occurs around $z = 1$, our simulation results may already give a viable description of the final state of single neutrino lumps.

6.3 Impact on matter perturbations

Understanding the impact of neutrino clustering on matter perturbations is of great relevance with regard to observations. Constraints on the matter power spectrum $P_m(k)$ can for instance be inferred from vast galaxy surveys (e. g. Reid et al., 2010; Percival et al., 2001); fluctuations in the galaxy number density are related to the matter density fluctuations by a suitable *bias* model. The evolution of matter perturbations in our scenario is sensitive to modifications of the gravitational potential Ψ. We have found a strong enhancement of the large–scale gravitational potential in Sec. 6.1.3. Accordingly, an amplification of the growth of matter fluctuations is expected.

A complementary probe of the matter dynamics is given by measurements of the peculiar velocity field. By virtue of the continuity equation, the growth of the fluctuation amplitude on a given scale k is related to the average peculiar velocity in a volume of size $L \approx \pi/k$. The net velocity of a specific volume is also called the *bulk flow*. Recent measurements of large–scale matter bulk flows on scales beyond $100\,h^{-1}$ Mpc have led to some excitement. Several studies suggest values larger (at least at the 2σ level) than the ΛCDM expectation (Kashlinsky et al., 2009; Watkins et al., 2009; Lavaux et al., 2010; Feldman et al., 2010). In an earlier study (Ayaita et al., 2009), we have roughly estimated the enhancement of matter bulk flows due to the gravitational potential induced by a collection of neutrino lumps. Now, we are in the position to directly measure large–scale flows in our simulation volume.

6.3.1 Enhancement of the power spectrum

The matter power spectrum is defined in Fourier space according to the general expression (see Eq. 3.36),

$$\left\langle \delta_m(\boldsymbol{k})\, \delta_m^*(\boldsymbol{k}') \right\rangle = (2\pi)^3\, P_m(k)\, \delta_D^3(\boldsymbol{k} - \boldsymbol{k}'). \tag{6.2}$$

In our numerical implementation, we apply a DFT to the density field $\delta_m(\boldsymbol{x})$ and estimate the amplitude $P_m(k)$ by averaging $|\delta_m(k)|^2$ (cf. Sec. 5.2.3 for details concerning discrete Fourier coefficients and their relationship to the continuous quantities). Below, we will follow the evolution of the dimensionless spectrum $\Delta_m(k)$, defined as

$$\Delta_m^2(k) = \frac{k^3}{2\pi^2}\, P_m(k). \tag{6.3}$$

Again, we employ the ΛCDM simulation described in Sec. 6.1.3 in order to achieve a fair comparison with standard dynamics. The reference results are labelled by $\Delta_m^{\Lambda\mathrm{CDM}}$. In Fig. 6.11, we plot the quotient $\Delta_m(k)/\Delta_m^{\Lambda\mathrm{CDM}}(k)$ at different redshifts z. As long as neutrino perturbations are small, the matter growth function does not deviate from the ΛCDM case (matter grows only due to its own gravitational potential; the influence of dark energy is restricted to the expansion rate). Hence, the fluctuation amplitudes at first coincide in both simulation runs. At times $z < 2$, neutrino clustering significantly contributes to the large–scale gravitational potential (cf. Fig. 6.7). As a consequence, we observe a mild amplification (of the order 1%) of $\Delta_m(k)$ at $z = 1.5$; only large scales, $k < 0.05\,h/\mathrm{Mpc}$, are affected. The effect becomes more pronounced in the subsequent evolution. At $z = 1$, the enhancement amounts to about 10% for small k. Still, compared to the amplification

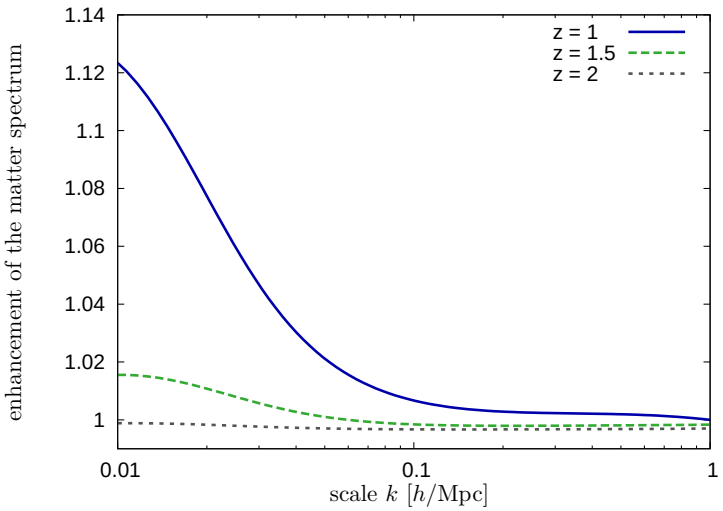

Figure 6.11: The evolution of the relative matter spectrum $\Delta_m(k)/\Delta_m^{\Lambda\mathrm{CDM}}(k)$. As a consequence of the neutrino–induced gravitational potential, we observe an enhancement of the matter power spectrum at large scales. The effect occurs at redshifts $z < 1.5$.

of the gravitational potential Ψ itself, the signature in the matter power spectrum is much weaker.

Let us briefly review the dynamics of matter perturbations in consideration of a raised amplitude of the gravitational potential. Combining the continuity (3.31) and Euler equation (3.32) within linear perturbation theory (neglecting Φ') yields the following evolution equation for $\delta_m(k)$:

$$\delta_m''(k) + \mathcal{H}\delta_m'(k) = -k^2\,\Psi(k). \tag{6.4}$$

Raising $\Psi(k)$, first of all, causes an increase of the second derivative $\delta_m(k)''$, while the effect on $\delta_m(k)$ needs to arise dynamically in the subsequent evolution. Peculiar velocities, on the other hand, represent a possibility to probe the first derivative $\delta_m'(k)$; even if the amplitude $\delta_m(k)$ has grown only marginally over a period of time, the peculiar velocity field might already reveal the dynamics at work.

6.3.2 Large–scale bulk flows

Let us consider a subvolume V_i of our simulation box. The matter bulk flow associated with this specific volume is given by the averaged peculiar velocity,

$$\bar{\boldsymbol{v}}_{m,i}^{\mathrm{pec}} = \frac{\int_{V_i} \mathrm{d}^3x\,\sqrt{\bar{g}}\,\boldsymbol{v}_m^{\mathrm{pec}}}{\int_{V_i} \mathrm{d}^3x\,\sqrt{\bar{g}}}. \tag{6.5}$$

The Cosmological Principle predicts a vanishing mean for large–scale bulk flows. A useful quantity for comparison with observations is the non–vanishing variance of the bulk flow. In order to measure it, we divide our simulation box into n subvolumes V_i of equal size, $V_i = V/n$; cubical shapes correspond to $V_i = l^3$ with $l^3 = L^3/n$. An estimate of the bulk flow variance on the comoving scale l is then obtained as

$$U_l^2 = \frac{1}{n}\sum_{i=1}^{n}\left(\bar{\boldsymbol{v}}_{m,i}^{\mathrm{pec}}\right)^2. \tag{6.6}$$

The specific value of the bulk flow variance can depend on the chosen shape of the subvolumes. A more common choice refers to a Gaussian window function (e. g. Watkins et al., 2009). Since we are not primarily interested in the absolute magnitude of the matter bulk flow but in the relative amplification due to neutrino clustering, the proposed "top–hat" windows (with the advantage of clear boundaries) are a suitable choice.

As in previous applications, we employ our reference ΛCDM simulation. Deviations from standard dynamics are expressed by the quotient $U_l/U_l^{\Lambda\mathrm{CDM}}$, whose evolution for two large scales is presented in Fig. 6.12. The figure shows a steep increase of the large–scale velocity flows at redshifts $z < 2$. The amplification is much more pronounced than for the matter density fluctuations; at $z = 1$, it reaches factors of about 1.5 to 2. As already anticipated at the end of the previous section, the bulk flow at a given redshift z is a direct measure of the current growth rate (cf. Eq. 3.31). Consequently, at $z = 1$, matter density fluctuations on the corresponding scales are still growing at an increased rate compared to ΛCDM.

Recent measurements of large–scale matter bulk flows challenge the ΛCDM con-

cordance model at the $\gtrsim 2\sigma$ level. In a Gaussian window of diameter $100\,h^{-1}$Mpc, Feldman et al. (2010) infer a bulk flow magnitude of 416±78 km/s, whereas the variance calculated within the ΛCDM concordance model only amounts to $U \approx 200$ km/s. The latter can be obtained within linear perturbation theory (see, e. g., Ayaita et al., 2009) according to

$$U^2 = \frac{1}{2\pi^2} \int_0^\infty \mathrm{d}k\, k^2\, P_v(k)\, |\tilde{W}(k)|^2, \tag{6.7}$$

where $\tilde{W}(k)$ is the Fourier transform of the Gaussian window function and the velocity power spectrum $P_v(k)$ is related to the matter power spectrum according to

$$P_v(k) = \frac{f_k^2 \mathcal{H}^2}{k^2} P_m(k), \text{ with } f_k = \frac{\mathrm{d}\ln\delta_k}{\mathrm{d}\ln a}. \tag{6.8}$$

Growing Neutrino Quintessence clearly has the potential to produce large matter bulk flows without significantly distorting the shape of the matter power spectrum at the same time. A more quantitative comparison with peculiar velocity data becomes possible, once the evolution of the model can be followed until $z = 0$. For the current choice of parameters, the effect on the velocities is rather strong. Peculiar velocity surveys are likely to provide useful constraints on the model parameters such as the coupling strength β. If anomalous bulk flows will indeed be confirmed by future observations, this might be an important hint towards large–scale dynamics beyond ΛCDM (see also Ayaita et al., 2009).

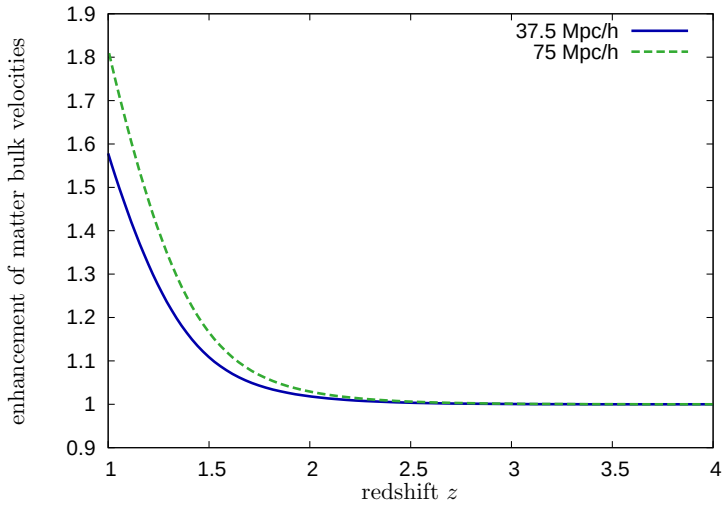

Figure 6.12: The enhancement of large–scale matter bulk flows, $U_l/U_l^{\Lambda\mathrm{CDM}}$, in subboxes of (comoving) volume l^3 for $l = 37.5\,h^{-1}$Mpc and $l = 75\,h^{-1}$Mpc. A significant amplification sets in at redshifts $z < 2$.

7 Aspects of Spherically Symmetric Neutrino Lumps

In the previous chapter, we have studied the evolution of GNQ until $z = 1$. After a phase of rapid structure formation, the overall picture was dominated by a collection of almost spherically symmetric neutrino lumps (cf., e. g., Fig. 6.1). Effectively, the neutrino component has undergone a transition from an unclustered fluid to a "fluid" of neutrino lumps. An effective description of this state may help to understand the further cosmological evolution.[1] In this section, we concern ourselves with the question of stability. We provide arguments for stable neutrino lumps from two different perspectives: First, by looking at the motion of a test particle (Sec. 7.1) and afterwards by studying the conditions for hydrodynamic equilibrium (Sec. 7.2). We propose a class of stable configurations with locally isotropic velocity distributions. As we will see in Sec. 7.3, the pressure contributions from neutrinos and the (inhomogeneous) cosmon field approximately cancel for such lumps, i. e., their intrinsic equation of state approximately vanishes.

In the framework of this chapter, we assume that the neutrino dynamics inside nonlinear structures are dominated by the cosmon–mediated fifth force and hence neglect the gravitational potentials. Spherical symmetry allows us to express all quantities as functions of the radial distance r from the center of the lump. We further split up the neutrino source term in the perturbed Klein–Gordon equation (5.42) according to $T(r) = \mathcal{T}(r) \exp\big(-\beta\,\delta\varphi(r)\big)$. By this means, the field $\mathcal{T}(r)$ is independent of local mass variations. For instance, assuming non–relativistic neutrinos, we have $\mathcal{T}(r) = -n_\nu(r) m_\nu(\bar{\varphi})$ with $n_\nu(r)$ denoting the neutrino number density and $m_\nu(\bar{\varphi})$ the neutrino mass for $\delta\varphi \equiv 0$. In the general case, the field $\mathcal{T}(r)$ also accounts for relativistic corrections (cf., e. g., Eq. 5.39). The cosmon perturbation $\delta\varphi(r)$ solves the radial Klein–Gordon equation,

$$\delta\varphi'' + 2\frac{\delta\varphi'}{r} - V_{,\varphi\varphi}(\bar{\varphi})\delta\varphi = \beta\left(\mathcal{T}\,\mathrm{e}^{-\beta\delta\varphi} - \bar{T}\right), \tag{7.1}$$

with a prime denoting differentiation with respect to r in this chapter (time derivatives will be indicated by a dot and refer to the cosmic time t). Without linearization of the mass function, Equation (7.1) is a nonlinear ordinary differential equation for $\delta\varphi(r)$. We generally impose the regularity condition $\delta\varphi'(r = 0) = 0$; for a unique solution, one may specify a boundary value $\delta\varphi(R)$ at some large distance R from the center.

[1] The effective description of neutrino lumps and their dynamics is work in progress in collaboration with Y. Ayaita and C. Wetterich.

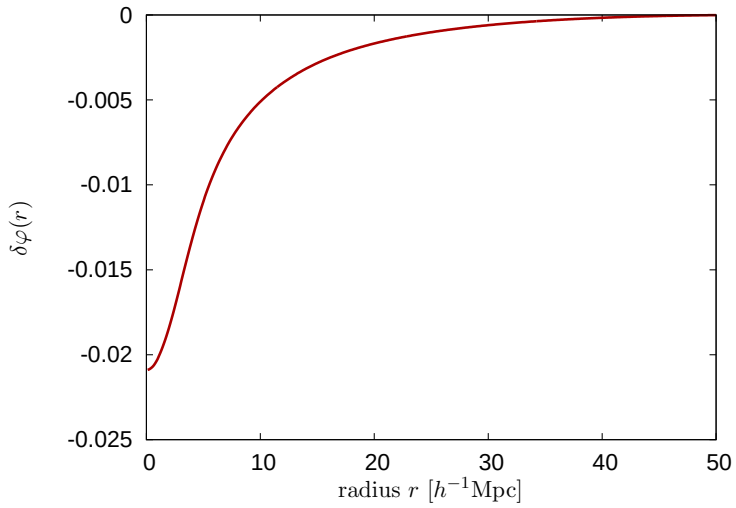

Figure 7.1: Exemplary profile $\delta\varphi(r)$ obtained as the solution to Eq. (7.1) with vanishing boundary value at large distances. The shape of the underlying neutrino profile $\mathcal{T}(r)$ was adopted from our simulation results, cf. Fig. 6.8; the (relative) amplitude of the overdensity amounts to 5×10^4, leading to a central mass suppression of $\exp(-\beta\,\delta\varphi(0)) \approx 1/3$ for $\beta = -52$.

7.1 Motion of a test particle

In this section, we study the motion of a neutrino particle in a static, spherically symmetric neutrino lump. Assuming a central overdensity of neutrinos, $-\mathcal{T}(r) > 0$, and $\delta\varphi \to 0$ for large distances, the solution to Eq. (7.1) is typically of the type illustrated in Fig. 7.1; the particular form of $\delta\varphi(r)$ is however not crucial for our purposes. Due to the fifth force, $\propto \beta\boldsymbol{\nabla}\delta\varphi = \beta\,\delta\varphi'(r)\boldsymbol{e}_r$, the particle is accelerated towards the center of the structure. In a sense, the situation is comparable to the dynamics of a test mass in a spherically symmetric gravitational potential. The main differences arise from mass variations $m_\nu = m_\nu(r)$, which are also responsible for a velocity dependent acceleration, cf. Sec. 5.2. We also need to account for possibly relativistic velocities.

The dynamics of our test particle are described by the action

$$S = -\int \mathrm{d}\tau\, m_\nu(\varphi) = -\int \mathrm{d}t\, \frac{m_\nu(\varphi)}{\gamma}, \tag{7.2}$$

with $\gamma = (1 - \boldsymbol{v}^2)^{-1/2}$ within our approximation. We consider the motion of the particle in a plane with polar coordinates (r, ϑ). The Lagrangian associated with the action, Eq. (7.2), is given by

$$L = -m_\nu(\varphi(r))\,\sqrt{1 - \dot{r}^2 - r^2\dot{\vartheta}^2}. \tag{7.3}$$

Since L does not explicitly depend on ϑ, we obtain angular momentum conserva-

tion:

$$\frac{\mathrm{d}p_\vartheta}{\mathrm{d}t} = 0, \text{ with } p_\vartheta = \frac{\partial L}{\partial \dot{\vartheta}} = \gamma m_\nu r^2 \dot{\vartheta}. \tag{7.4}$$

As in the standard case, angular momentum conservation supports stable orbits. The equation of motion for the radial coordinate is given by the Euler–Lagrange equation:

$$\frac{\mathrm{d}p_r}{\mathrm{d}t} = \frac{p_\vartheta^2}{\gamma m_\nu r^3} + \frac{m_\nu}{\gamma}\beta\,\delta\varphi', \text{ with } p_r = \frac{\partial L}{\partial \dot{r}} = \gamma m_\nu \dot{r}. \tag{7.5}$$

We have used the definition of the coupling parameter $\beta = -\mathrm{d}\ln m_\nu/\mathrm{d}\varphi$ above. The importance of angular momentum conservation now becomes apparent: Similar to the standard case of gravity, it introduces an effective outwards–directed force. Due to Lorentz factors and the varying neutrino mass, the usual $1/r^3$ behavior is modified (for the case of gravity with special relativistic corrections, see, e. g., Lemmon and Mondragon, 2010). In order to see that this equation generally implies stable orbits, we use Eq. (7.4) to replace the time variable by ϑ,

$$\frac{\mathrm{d}}{\mathrm{d}t} = \frac{p_\vartheta}{\gamma m_\nu r^2}\frac{\mathrm{d}}{\mathrm{d}\vartheta}, \tag{7.6}$$

and further define $u = 1/r$. The radial equation of motion can then be written as

$$\frac{\mathrm{d}^2 u}{\mathrm{d}\vartheta^2} = -u - \frac{\beta\,\delta\varphi'}{p_\vartheta^2 u^2} m_\nu^2. \tag{7.7}$$

For $\delta\varphi' < 0$ (and $\beta < 0$), the second term on the right–hand side expresses attraction towards the center. Assuming $\delta\varphi'(r) \to 0$ for $r \to 0$, it becomes negligible for small values of r (large u). The first term, on the contrary, is repulsive and becomes arbitrarily large for $r \to 0$, preventing the particle from falling into the center. This is also true under more general conditions; assuming for instance $\delta\varphi(r) = \varphi_0(r/r_0)^{-\alpha}$ with $\alpha, r_0 > 0$ and $\varphi_0 < 0$, the attractive term behaves like $(r/r_0)^{1-\alpha}\exp\big(-2\,\beta\,\varphi_0(r/r_0)^{-\alpha}\big) \to 0$ for $r \to 0$.

This brief study of particle motion in a spherically symmetric cosmon field $\varphi(r)$ supports the assumption of stability. Although the situation is different to standard Newtonian dynamics in a spherically symmetric gravitational potential, the principle of angular momentum conservation plays the major role in both cases.

7.2 Hydrodynamic equilibrium

We now ask for the conditions of hydrodynamic equilibrium for a spherically symmetric neutrino lump. The hydrodynamic description employs moments of the phase–space distribution function $f_\nu(t, x^i, p_j)$, where $p_j = m_\nu u_j$ is the momentum. The four velocity u_j is related to the peculiar velocity $\boldsymbol{v}$ via $u_j = \gamma v^j/a$ (as in previous sections, $v_j = \delta_{ij}v^i$). A derivation of the moment equations for standard gravitational dynamics is presented by Bernardeau et al. (2002).

As a starting point, we propose particle conservation in phase space, expressed

by the continuity equation

$$\dot{f} + \dot{x}^i \frac{\partial f}{\partial x^i} + \dot{p}_j \frac{\partial f}{\partial p_j} = 0. \tag{7.8}$$

Before we start with the actual calculation, we quote the equation of motion for a neutrino particle in terms of the momentum p_j. Therefor, we note that $\mathrm{d}p_j/\mathrm{d}\tau = (\mathrm{d}m_\nu/\mathrm{d}\tau)u_j + m_\nu(\mathrm{d}u_j/\mathrm{d}\tau)$ with $\mathrm{d}m_\nu/\mathrm{d}\tau = -\beta m_\nu\, u^\alpha \partial_\alpha \varphi$ and $\mathrm{d}u_j/\mathrm{d}\tau$ given by Eq. (5.11). Replacing the proper time τ by the cosmic time t yields

$$\dot{p}_j = \gamma^{-1} m_\nu\, \beta\, \partial_j \varphi. \tag{7.9}$$

We simplify the whole calculation by restricting ourselves to first–order relativistic corrections. This means we will use the following equations:

$$\dot{x}^i = \frac{p^i}{a m_\nu}, \tag{7.10}$$

$$\dot{p}_j = \left(1 - \frac{\boldsymbol{p}^2}{2a^2 m_\nu^2}\right) m_\nu \beta \partial_j \varphi, \tag{7.11}$$

with $\boldsymbol{p}^2 = \sum_{j=1}^3 p_j^2$. Let us now define the relevant moments of the distribution function f:

$$n = \int \mathrm{d}^3 p\, f(t, \boldsymbol{x}, \boldsymbol{p}) \tag{7.12}$$

$$n U_i = \int \mathrm{d}^3 p\, \frac{p_i}{a m_\nu} f(t, \boldsymbol{x}, \boldsymbol{p}), \tag{7.13}$$

$$\sigma_{ij} + n U_i U_j = \int \mathrm{d}^3 p\, \frac{p_i}{a m_\nu} \frac{p_j}{a m_\nu} f(t, \boldsymbol{x}, \boldsymbol{p}). \tag{7.14}$$

The moments defined above have clear intuitive meanings: $n(t, \boldsymbol{x})$ is the number density, $U_i(t, \boldsymbol{x})$ is the average peculiar velocity, and $\sigma_{ij}(t, \boldsymbol{x})$ describes the velocity dispersion at position $\boldsymbol{x}$ and time t. Technically, we may generally define the averaging

$$\langle A \rangle_f = \frac{\int \mathrm{d}^3 p\, A\, f}{\int \mathrm{d}^3 p\, f}, \tag{7.15}$$

for an arbitrary field $A(t, x^i, p_j)$ and identify $U_i = \langle v_i \rangle_f$ and $\sigma_{ij} = n \left\langle (v_i - U_i)(v_j - U_j) \right\rangle_f$.

We will now derive the moment equations (analogously to the standard case, cf., Bernardeau et al., 2002). First, we integrate out the momentum in Eq. (7.8), yielding

$$\dot{n} + \frac{\partial}{a \partial x^i} (n U_i) = 0. \tag{7.16}$$

This is the standard continuity equation describing the change in $n(t, \boldsymbol{x})$ due to peculiar motion. The factor of a transforms the derivative $\partial/\partial x^i$ into a derivative with respect to physical coordinates $r^i = a x^i$. For convenience, we will use the abbreviation $\partial_{r_i} = a^{-1}\partial/\partial x^i$ in the following. Taking the first moment of Eq. (7.8),

and using the continuity equation (7.16), we find

$$\dot{U}_i + (U_j\,\partial_{r_j})U_i + (H - \beta\dot{\varphi})U_i + \frac{1}{n}\partial_{r_j}\sigma_{ij} = \beta\partial_{r_i}\varphi\left(1 - \frac{1}{2}U^2 + \frac{3\sigma}{2n}\right) + \beta(U_j\,\partial_{r_j}\varphi)U_i + \frac{\beta}{n}\sigma_{ij}\partial_{r_j}\varphi, \qquad (7.17)$$

with $\sigma \equiv \sigma^i{}_i/3$. Again, we identify the fifth force $\propto \beta\boldsymbol{\nabla}\delta\varphi$ and the velocity dependent force $\propto (\boldsymbol{U}\cdot\boldsymbol{\nabla})\boldsymbol{U}$, as well as the modification to the Hubble damping due to the time variation of φ. In addition, the "microphysical" motion expressed by the dispersion tensor σ_{ij} gives rise to an effective pressure force $\propto \partial_{r_j}\sigma_{ij}$ and introduces further extra terms due to the coupling to the cosmon field.

For a stable lump, we demand $\dot{n} = 0$ and $\dot{U} = 0$. According to Eq. (7.16), the first condition is fulfilled for locally isotropic velocity distributions with $U_i = 0$ for all $\boldsymbol{x}$. Under this assumption, Eq. (7.17) considerably simplifies. Projecting out the radial component,[2] we obtain

$$\frac{\sigma'}{n} = \beta\varphi'\left(1 - \frac{\sigma}{2n}\right), \qquad (7.18)$$

with $\sigma_{ij} = \delta_{ij}\sigma$ (due to local isotropy). Essentially, the effective pressure generated by the microphysical velocity dispersion needs to balance the inwards directed fifth force; corrections appear due to the coupling terms in Eq. (7.17). Within our approximation, the one–dimensional velocity dispersion reads

$$\sigma = \frac{1}{3}n\langle\boldsymbol{v}^2\rangle_f. \qquad (7.19)$$

Equation (7.18) has to be solved together with the radial Klein–Gordon equation (7.1) for $\delta\varphi(r)$. The source $\mathcal{T}(r)$ on the right–hand side is related to the number density and the velocity dispersion: The contribution of a single particle to $\mathcal{T}$ is given by $-m_\nu(\bar{\varphi})/\gamma \approx -m_\nu(\bar{\varphi})(1-\boldsymbol{v}^2/2)$ at the position of the particle. Integration over phase space thus yields

$$\frac{\mathcal{T}(r)}{m_\nu(\bar{\varphi})} = -n(r)\left(1 - \frac{1}{2}\langle\boldsymbol{v}^2\rangle_f\right) = -n(r) + \frac{3}{2}\sigma(r) \qquad (7.20)$$

according to the definitions given above and to first order in $\boldsymbol{v}^2$.

7.3 Pressure cancellation

In the previous section, we have derived the conditions for hydrodynamic stability of spherically symmetric neutrino lumps. For a given neutrino number density profile $n(r)$, we can solve Eqs. (7.1) and (7.18) with the identification made in Eq. (7.20). The simulation results presented in Chapter 6 provide us with templates for the neutrino profile $n(r)$. In this section, we adopt the profile shown in Fig. 6.8 with a rescaled central amplitude in order to avoid too large velocities; the corresponding

[2] For $\boldsymbol{U} = 0$, one simply has $\dot{U}_r = \dot{\boldsymbol{U}}\cdot\boldsymbol{e}_r$.

cosmon field $\delta\varphi(r)$ has already been shown in Fig. 7.1. Stable configurations can be placed in the center of a smaller simulation box with considerably increased spatial resolution. This allows to numerically investigate their characteristic properties. Here, we study the intrinsic equation of state of a cosmon–neutrino lump,

$$w_l = \frac{\bar{P}_{l,\nu} + \bar{P}_{l,\varphi}}{\bar{\rho}_{l,\nu} + \bar{\rho}_{l,\varphi}}, \tag{7.21}$$

with $\bar{P}_{l,\nu}$, $\bar{P}_{l,\varphi}$ and $\bar{\rho}_{l,\nu}$, $\bar{\rho}_{l,\varphi}$ denoting the averaged pressure and energy density contributions from neutrinos and the cosmon field associated with the lump. Let us focus on the pressure first.

From the general definition, $P = T^i{}_i/3$ (cf. Eq. 3.27), we obtain for the neutrino component

$$\bar{P}_{l,\nu} = \frac{1}{V_l}\int_{V_l} \mathrm{d}^3 r\, T^i{}_i(r)/3 \tag{7.22}$$

$$= \frac{1}{V_l}\sum_{r_p \le R_l}\left(\frac{1}{3}\gamma_p m_\nu(r_p)\boldsymbol{v}_p^2\right) \equiv \frac{1}{V_l} I_\nu(R_l), \tag{7.23}$$

where $T^\alpha{}_\beta$ denotes the neutrino energy–momentum tensor (see Eq. 5.13 for the one–particle contributions), and the subscript p labels particles inside the lump. We assume that the lump is surrounded by a void region, such that contributions to the integral in the first line are restricted to $r < R_l$ for some radius R_l. In the last line, we have defined the integrated pressure contribution $I_\nu(R_l)$, which will be used below. Note that we have used physical coordinates above; V_l is the volume of the structure in physical units. Turning to the cosmon contribution, we need to pay attention to the fact, that the total cosmon pressure P_φ also includes contributions from the background field $\bar{\varphi}$. In order to obtain a well defined quantity, we subtract this contribution from $P(\varphi)$; this guarantees that the pressure $\bar{P}_{l,\varphi}$ vanishes for large distances from the center. The cosmon energy–momentum tensor, Eq. (2.43), then gives

$$\bar{P}_{l,\varphi} = \frac{1}{V_l}\int \mathrm{d}^3 r\, \left(-\frac{1}{6}|\boldsymbol{\nabla}_r \delta\varphi|^2 - V(\bar{\varphi}+\delta\varphi) + V(\bar{\varphi})\right) \tag{7.24}$$

$$= \frac{1}{V_l}\int_0^{R_l} 4\pi r^2 \mathrm{d}r\, \left(-\frac{1}{6}|\delta\varphi'(r)|^2 - V(\bar{\varphi}+\delta\varphi(r)) + V(\bar{\varphi})\right) \tag{7.25}$$

$$\equiv \frac{1}{V_l} I_\varphi(R_l), \tag{7.26}$$

where we have defined $I_\varphi(R_l)$ analogously to $I_\nu(R_l)$ above.

An appropriate choice of R_l cannot be motivated by considering the neutrino distribution only. In general, the cosmon perturbations $\delta\varphi(r)$ extend to larger distances than the neutrino overdensity $n(r)$. This is demonstrated by the example shown in Fig. 7.1, where $\delta\varphi(r)$ extends to more than $30\,h^{-1}$Mpc although the underlying neutrino density profile is restricted to less than $20\,h^{-1}$Mpc. For this reason, we have kept R_l as a free parameter. In Fig. 7.2, we plot the functions I_ν and I_φ for varying R_l. The neutrino pressure shows a steep increase at small

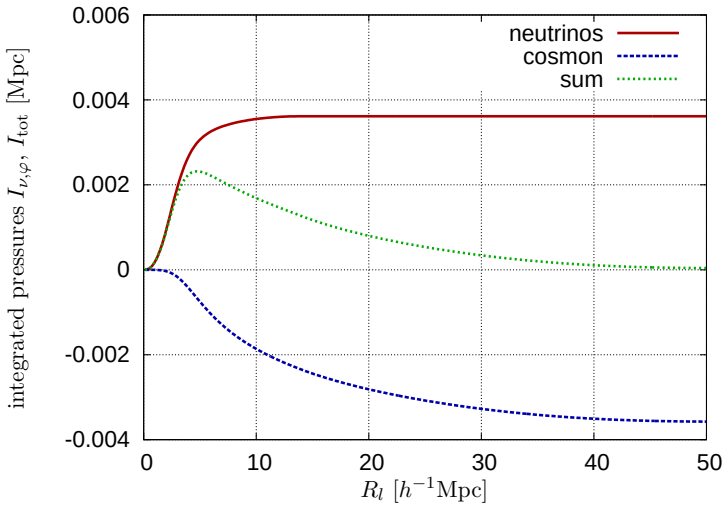

Figure 7.2: The integrated pressure contributions I_ν, I_φ from neutrinos and the inhomogeneous cosmon field as a function of R_l. We also plot the sum $I_{\rm tot} = I_\nu + I_\varphi$. Close to the center, the neutrino pressure dominates. At larger distances, the two contributions approximately cancel each other.

distances from the center but saturates at $R_l \gtrsim 10\,h^{-1}$ Mpc. As expected, the cosmon pressure still receives contributions from larger distances. While it only slowly saturates, it more and more cancels the contribution from the neutrino component. The total integrated pressure $I_{\rm tot} = I_\nu + I_\varphi$ tends to zero for large R_l.

This result speaks for a vanishing total pressure of the lump. The equation of state parameter w_l sets the residual pressure in relation to the total energy density associated with the lump. Straightforward computations yield

$$\bar{\rho}_{l,\nu} = \frac{1}{V_l} \sum_{r_p \leq R_l} \gamma_p m_\nu(r_p), \tag{7.27}$$

$$\bar{\rho}_{l,\varphi} = \frac{1}{V_l} \int_0^{R_l} 4\pi r^2 {\rm d}r \left(\frac{1}{2} |\delta\varphi'|^2 + V(\bar{\varphi} + \delta\varphi(r)) - V(\bar{\varphi}) \right). \tag{7.28}$$

In Fig. 7.3, we plot w_l as a function of R_l. For comparison, we also show the neutrino equation of state $w_{l,\nu} = \bar{P}_{l,\nu}/\bar{\rho}_{l,\nu}$. The cancellation of pressure is significant for w_l. Although neutrino motion gives rise to $w_{l,\nu} \gtrsim 0.1$, the combination of cosmon and neutrino contributions leads to $w_l \lesssim 10^{-3}$. This is in the regime of non–relativistic matter. Hence, in its rest–frame, the energy–momentum tensor of the lump will essentially be described by the total mass energy (with contributions from neutrinos and the cosmon). This is expected to simplify an effective description of neutrino lumps. As a crucial step in this direction, it however remains to find an appropriate modelling of the mutual interactions between separated lumps.

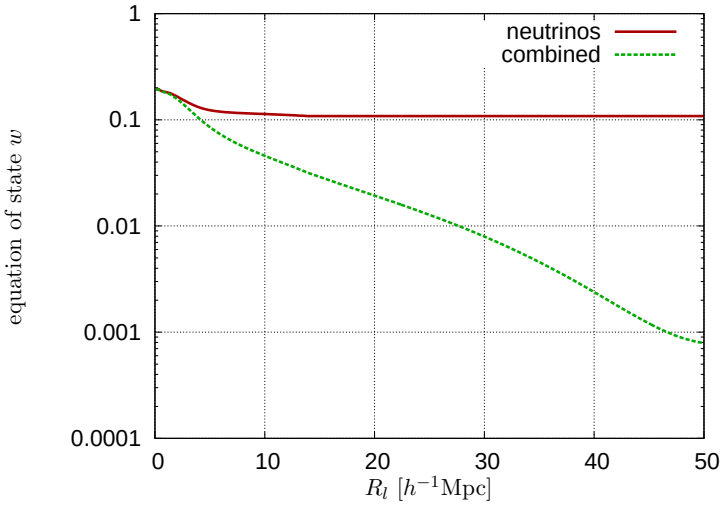

Figure 7.3: The intrinsic equation of state w_l of a stable lump as a function of R_l compared to the neutrino equation of state $w_{l,\nu}$. The cancellation of neutrino and cosmon pressure contributions significantly suppresses the total equation of state. For $R_l = 50h^{-1}$ Mpc, w_l is two orders of magnitude smaller than $w_{l,\nu}$.

8 Conclusions and Outlook

In this thesis, we have investigated the cosmological implications of Growing Neutrino Quintessence, a model that has been proposed to provide possible answers to pressing questions concerning the phenomenon of dark energy: Why is the present dark energy density in the Universe so small? And why has dark energy become important just today? These fundamental puzzles are indeed the main motivation to seek for alternatives to the cosmological constant scenario, which is so far surprisingly consistent with observational data. The idea of solving these problems by a growing neutrino mass is intriguing; beyond that, the prospects are also promising that it will be testable. This work has identified a rich cosmological phenomenology with features very distinct from the standard ΛCDM model. Essentially all of them are rooted in the strong coupling between neutrinos and the quintessence field. This interaction provides the key mechanism for solving the "why now" problem of dark energy. On the other hand, it renders the treatment of perturbations extremely challenging due to a strong attractive force acting between neutrinos; linear perturbation theory as well as standard N–body methods fail.

For this reason, we have developed a relativistic N–body treatment of growing neutrinos in Chapter 5. In order to incorporate local neutrino mass variations, inhomogeneities in the quintessence field are modelled on a grid. The presented method is also compatible with backreaction effects due to nonlinear neutrino clustering. At its current stage, the simulation method is kept as simple as possible. In particular, it focuses on large–scale dynamics (mostly relevant for neutrino clustering) and solves the perturbed Klein–Gordon equation by virtue of a simple iterative scheme that is successful until redshift $z = 1$. Matter and gravity are evolved as in ordinary particle–mesh algorithms.

With this method, we were able to follow the formation of nonlinear neutrino structures from tiny fluctuations to compact, almost spherically symmetric lumps in Chapter 6. During the phase of nonlinear clustering, we observed a significant increase in neutrino velocities. Until $z = 1$, the major part of neutrinos in our simulation has been accelerated to relativistic velocities $\gtrsim 50\%$ of the speed of light. As a consequence, the averaged neutrino equation of state grew from small values of the order 10^{-4} to $w_\nu \approx 0.1$ between redshifts $z = 2.5$ and $z = 1$. Due to relativistic motion inside neutrino structures, we found local differences between the two gravitational potentials Ψ and Φ (a 1% to 10% effect). On large scales, we obtained a significant enhancement of the potentials' amplitudes. As a direct consequence, a steep increase in the large–scale matter bulk velocities was observed, while the effect on the matter power spectrum was much less pronounced (amounting to about 10% at small k).

Furthermore, we have studied the properties of individual neutrino lumps in our simulation box. As a major result, we found a strong suppression of the local

neutrino mass inside concentrated structures. In consideration of our method's limited small–scale resolution, we can only provide approximate upper bounds. At $z = 1$, the mass of particles at the center of concentrated lumps was typically one order of magnitude smaller than outside the structure. This effect has already been suggested by analytical studies (Nunes et al., 2011).

Over the last decades, cosmology has developed a variety of complementary observational probes to explore the constituents and the expansion of the Universe. Many of these probes are sensitive to the aforementioned phenomena and are likely to provide tight constraints on the model parameters once the evolution can be followed until redshift $z = 0$. On the one hand, the ISW probes the time evolution of the gravitational potentials. Detailed measurements of the signal's redshift dependence together with the overall effect on the CMB spectrum (see also Pettorino et al., 2010) can be powerful for scrutinizing the model. Furthermore, the three–dimensional version of WL is promising to constrain the absolute amplitude of the large–scale gravitational potentials. We have provided numerical tools for the necessary computations in Chapter 4; as an exemplary application, we have studied the prospects for constraining the dark energy speed of sound.

Moreover, observations of the large–scale matter bulk flows are of great relevance since they are sensitive to the neutrino–induced gravitational potential. Interestingly, it is an open debate whether matter bulk flows on scales beyond $100h^{-1}$Mpc are consistent with ΛCDM (e. g. Feldman et al., 2010). If an anomaly exists, this will be an important hint towards large–scale dynamics distinct from the concordance model.

On the particle physics side, it is important to accurately measure the present neutrino mass. In the model under consideration, a definite prediction of the local neutrino mass at our position in the Universe is complicated by the effect of local neutrino mass variations. If terrestrial experiments, however, detect significant deviations from the cosmological bounds on the neutrino masses in the early Universe, this will strongly support the idea of a varying neutrino mass. Hopefully, the results from the KATRIN experiment will reveal new insights. After all, it may turn out that the exemplary set of parameters chosen in Chapter 6 is not compatible with observations. Eventually, the full parameter space of the model needs to be explored.

The simulation method as presented in this work has already helped deepen our understanding of the cosmological dynamics in the framework of Growing Neutrino Quintessence. The results have highlighted that relativistic neutrino dynamics, local mass variations, and backreaction effects are indeed decisive for any quantitative analysis of the model. In future, one may, on the one hand, seek improvements on the numerical side. In particular, more sophisticated methods for the solution of the perturbed Klein–Gordon equation are in order to extend the range of applicability. Further, an increased resolution at small scales (important for studying the intrinsic structure of neutrino lumps, but also for matter clustering) can be achieved by adopting methods from modern N–body codes like GADGET. Alternatively, one may pursue a different direction. The simulation results at $z = 1$ suggest that after a phase of complex structure formation, almost all neutrinos are bound to approximately spherically symmetric lumps. This raises the ques-

tion whether the overall cosmological evolution can be understood by studying the effective dynamics of separated neutrino lumps without paying regard to their detailed intrinsic structures. As a first step in this direction, we have had a look at spherically symmetric neutrino lumps in Chapter 7. There, we found the conditions for hydrodynamic equilibrium and studied a simple class of stable configurations. Numerically, we investigated the intrinsic equation of state and found a remarkable cancellation of the total pressure. This result suggests that static cosmon–neutrino lumps can approximately be modelled as effective "particles" characterized by their total mass energy. With a suitable description of the mutual interactions between such lumps, the cosmological evolution until $z = 0$ can possibly be understood within a considerably simplified approach.

Ingenious developments in the fields of theory, observation, and simulation have helped to establish the standard framework of modern cosmology. We shall remain confident that this success continues and the mystery of dark energy can eventually be unraveled. This may have exciting implications for fundamental physics.

List of Tables

List of Figures

List of Abbreviations

BAO	baryon acoustic oscillations
BBN	Big Bang nucleosynthesis
CDM	cold dark matter
CMB	Cosmic Microwave Background
DFT	discrete Fourier transform
FFT	fast Fourier transform
FLRW	Friedmann–Lemaître–Robertson–Walker
GNQ	Growing Neutrino Quintessence
GR	General Relativity
ISW	integrated Sachs–Wolfe effect
SN Ia	supernovae of Type Ia
WL	weak lensing
WMAP	Wilkinson Microwave Anisotropy Probe

Bibliography

Adamson, P. et al. (2012). An improved measurement of muon antineutrino disappearance in MINOS. *Phys.Rev.Lett.*, 108:191801, 1202.2772.

Ade, P. et al. (2011). Planck Early Results. I. The Planck mission. *Astron.Astrophys.*, 536:16464, 1101.2022.

Ahn, M. et al. (2006). Measurement of Neutrino Oscillation by the K2K Experiment. *Phys.Rev.*, D74:072003, hep-ex/0606032.

Alpher, R. A., Bethe, H., and Gamow, G. (1948). The origin of chemical elements. *Phys. Rev.*, 73:803–804.

Amara, A. and Réfrégier, A. (2007). Optimal surveys for weak-lensing tomography. *MNRAS*, 381:1018–1026, astro-ph/0610127.

Amendola, L. (2000). Coupled quintessence. *Phys.Rev.*, D62:043511, astro-ph/9908023.

Amendola, L., Baldi, M., and Wetterich, C. (2008). Quintessence cosmologies with a growing matter component. *Phys.Rev.*, D78:023015, 0706.3064.

Amendola, L. et al. (2012). Cosmology and fundamental physics with the Euclid satellite. *ArXiv eprints 1206.1225*.

Amendola, L., Kunz, M., and Sapone, D. (2008). Measuring the dark side (with weak lensing). *JCAP*, 4:13, 0704.2421.

Amendola, L. and Quercellini, C. (2003). Tracking and coupled dark energy as seen by WMAP. *Phys.Rev.*, D68:023514, astro-ph/0303228.

Amendola, L. and Tsujikawa, S. (2010). *Dark Energy. Theory and Observations*. Cambridge University Press.

Ansari, R. U. H. and Unnikrishnan, S. (2011). Perturbations in dark energy models with evolving speed of sound. *ArXiv e-prints 1104.4609*.

Armendariz-Picon, C., Mukhanov, V. F., and Steinhardt, P. J. (2000). A Dynamical solution to the problem of a small cosmological constant and late time cosmic acceleration. *Phys.Rev.Lett.*, 85:4438–4441, astro-ph/0004134.

Armendariz-Picon, C., Mukhanov, V. F., and Steinhardt, P. J. (2001). Essentials of k essence. *Phys.Rev.*, D63:103510, astro-ph/0006373.

Ayaita, Y., Schäfer, B. M., and Weber, M. (2012a). Investigating clustering dark energy with 3d weak cosmic shear. *MNRAS*, 422:3056–3066, 1110.1985.

Ayaita, Y., Weber, M., and Wetterich, C. (2009). Peculiar Velocity Anomaly from Forces Beyond Gravity? *ArXiv e-prints 0908.2903*.

Ayaita, Y., Weber, M., and Wetterich, C. (2012b). Structure Formation and Backreaction in Growing Neutrino Quintessence. *Phys.Rev.*, D85:123010, 1112.4762.

Babichev, E., Mukhanov, V., and Vikman, A. (2008). k-Essence, superluminal propagation, causality and emergent geometry. *JHEP*, 0802:101, 0708.0561.

Bagla, J. S. and Padmanabhan, T. (1997). Cosmological N-body simulations. *Pramana*, 49:161–192, astro-ph/0411730.

Baldi, M., Pettorino, V., Amendola, L., and Wetterich, C. (2011). Oscillating nonlinear large scale structure in growing neutrino quintessence. *MNRAS*, 418:214–229, 1106.2161.

Baldi, M., Pettorino, V., Robbers, G., and Springel, V. (2010). Hydrodynamical N-body simulations of coupled dark energy cosmologies. *MNRAS*, 403:1684–1702, 0812.3901.

Ballesteros, G. and Lesgourgues, J. (2010). Dark energy with non-adiabatic sound speed: initial conditions and detectability. *JCAP*, 1010:014, 1004.5509.

Bartelmann, M. (2010). Gravitational Lensing. *Class.Quant.Grav.*, 27:233001, 1010.3829.

Bartelmann, M. (2010). The dark Universe. *Reviews of Modern Physics*, 82:331–382, 0906.5036.

Bartelmann, M. and Schneider, P. (2001). Weak gravitational lensing. *Physics Reports*, 340:291–472.

Bean, R. and Dore, O. (2004). Probing dark energy perturbations: The Dark energy equation of state and speed of sound as measured by WMAP. *Phys.Rev.*, D69:083503, astro-ph/0307100.

Behrend, J., Brown, I. A., and Robbers, G. (2008). Cosmological Backreaction from Perturbations. *JCAP*, 0801:013, 0710.4964.

Bennett, C. et al. (2003). First year Wilkinson Microwave Anisotropy Probe (WMAP) observations: Preliminary maps and basic results. *Astrophys.J.Suppl.*, 148:1, astro-ph/0302207.

Bergstrom, L. (2012). Dark Matter Evidence, Particle Physics Candidates and Detection Methods. *ArXiv eprints 1205.4882*.

Bernardeau, F., Colombi, S., Gaztanaga, E., and Scoccimarro, R. (2002). Large scale structure of the universe and cosmological perturbation theory. *Phys.Rept.*, 367:1–248, astro-ph/0112551.

Bernstein, G. and Jain, B. (2004). Dark Energy Constraints from Weak-Lensing Cross-Correlation Cosmography. *ApJ*, 600:17–25, astro-ph/0309332.

Bolte, M. and Hogan, J. (1995). Conflict over the age of the Universe. *Nature*, 376:399–402.

Brax, P., Martin, J., and Riazuelo, A. (2000). Exhaustive study of cosmic microwave background anisotropies in quintessential scenarios. *Phys.Rev.*, D62:103505, astro-ph/0005428.

Brill, D. R. and Wheeler, J. A. (1957). Interaction of neutrinos and gravitational fields. *Rev.Mod.Phys.*, 29:465–479.

Brouzakis, N., Pettorino, V., Tetradis, N., and Wetterich, C. (2011). Nonlinear matter spectra in growing neutrino quintessence. *JCAP*, 1103:049, 1012.5255.

Brouzakis, N., Tetradis, N., and Wetterich, C. (2008). Neutrino Lumps in Quintessence Cosmology. *Phys.Lett.*, B665:131–134, 0711.2226.

Brown, I. A., Behrend, J., and Malik, K. A. (2009). Gauges and Cosmological Backreaction. *JCAP*, 0911:027, 0903.3264.

Buchert, T. and Ehlers, J. (1997). Averaging inhomogeneous Newtonian cosmologies. *Astron.Astrophys.*, 320:1–7, astro-ph/9510056.

Caldera-Cabral, G., Maartens, R., and Schäfer, B. M. (2009). The Growth of Structure in Interacting Dark Energy Models. *JCAP*, 0907:027, 0905.0492.

Camera, S., Kitching, T. D., Heavens, A. F., Bertacca, D., and Diaferio, A. (2010). Measuring Unified Dark Matter with 3D cosmic shear. *ArXiv e-prints 1002.4740*.

Carroll, S. M. (2004). *Spacetime and Geometry*. Addison Wesley.

Carroll, S. M., De Felice, A., Duvvuri, V., Easson, D. A., Trodden, M., et al. (2005). The Cosmology of generalized modified gravity models. *Phys.Rev.*, D71:063513, astro-ph/0410031.

Castro, P. G., Heavens, A., and Kitching, T. (2005). Weak lensing analysis in three dimensions. *Phys.Rev.*, D72:023516, astro-ph/0503479.

Clifton, T., Ferreira, P. G., Padilla, A., and Skordis, C. (2012). Modified Gravity and Cosmology. *Phys.Rept.*, 513:1–189, 1106.2476.

Clowe, D., Bradac, M., Gonzalez, A. H., Markevitch, M., Randall, S. W., et al. (2006). A direct empirical proof of the existence of dark matter. *Astrophys.J.*, 648:L109–L113, astro-ph/0608407.

Davis, M., Efstathiou, G., Frenk, C. S., and White, S. D. (1985). The Evolution of Large Scale Structure in a Universe Dominated by Cold Dark Matter. *Astrophys.J.*, 292:371–394.

De Bernardis, F., Martinelli, M., Melchiorri, A., Mena, O., and Cooray, A. (2011). Future weak lensing constraints in a dark coupled universe. *Phys. Rev.*, D84:023504, 1104.0652.

de Bernardis, P. et al. (2000). A Flat Universe from High-Resolution Maps of the Cosmic Microwave Background Radiation. *Nature*, 404:955–959.

de Putter, R., Huterer, D., and Linder, E. V. (2010). Measuring the Speed of Dark: Detecting Dark Energy Perturbations. *Phys.Rev.*, D81:103513, 1002.1311.

DeDeo, S., Caldwell, R., and Steinhardt, P. J. (2003). Effects of the sound speed of quintessence on the microwave background and large scale structure. *Phys.Rev.*, D67:103509, astro-ph/0301284.

Dehnen, W. and Read, J. (2011). N-body simulations of gravitational dynamics. *Eur.Phys.J.Plus*, 126:55, 1105.1082.

Dolag, K., Borgani, S., Schindler, S., Diaferio, A., and Bykov, A. (2008). Simulation techniques for cosmological simulations. *ArXiv eprints 0801.1023*.

Dolgov, A. (2002). Neutrinos in cosmology. *Phys.Rept.*, 370:333–535, hep-ph/0202122.

Doran, M. (2005). CMBEASY:: an Object Oriented Code for the Cosmic Microwave Background. *JCAP*, 0510:011, astro-ph/0302138.

Doran, M. (2008). A primer on cosmology and the cosmic microwave background. *Lecture at the University of Heidelberg in the winterterm 2008/09*, www.cmbeasy.org.

Doran, M., Muller, C. M., Schafer, G., and Wetterich, C. (2003). Gauge-invariant initial conditions and early time perturbations in quintessence universes. *Phys.Rev.*, D68:063505, astro-ph/0304212.

Doran, M., Robbers, G., and Wetterich, C. (2007). Impact of three years of data from the Wilkinson Microwave Anisotropy Probe on cosmological models with dynamical dark energy. *Phys.Rev.*, D75:023003, astro-ph/0609814.

Doran, M. and Wetterich, C. (2003). Quintessence and the cosmological constant. *Nucl.Phys.Proc.Suppl.*, 124:57–62, astro-ph/0205267.

Eisenstein, D. J. et al. (2005). Detection of the baryon acoustic peak in the large-scale correlation function of SDSS luminous red galaxies. *Astrophys.J.*, 633:560–574, astro-ph/0501171.

Erickson, J. K., Caldwell, R., Steinhardt, P. J., Armendariz-Picon, C., and Mukhanov, V. F. (2002). Measuring the speed of sound of quintessence. *Phys.Rev.Lett.*, 88:121301, astro-ph/0112438.

Fardon, R., Nelson, A. E., and Weiner, N. (2004). Dark energy from mass varying neutrinos. *JCAP*, 0410:005, astro-ph/0309800.

Feldman, H. A., Watkins, R., and Hudson, M. J. (2010). Cosmic Flows on 100 Mpc/h Scales: Standardized Minimum Variance Bulk Flow, Shear and Octupole Moments. *MNRAS*, 407:2328–2338, 0911.5516.

Friedman, A. (1922). Über die Krümmung des Raumes. *Zeitschrift für Physik A*, 10:377–386.

Frigo, M. and Johnson, S. G. (2005). The design and implementation of FFTW3. *Proceedings of the IEEE*, 93(2):216–231. Special issue on "Program Generation, Optimization, and Platform Adaptation".

Fukuda, Y. et al. (1998). Evidence for oscillation of atmospheric neutrinos. *Phys.Rev.Lett.*, 81:1562–1567, hep-ex/9807003.

Galassi, M. et al. (2009). GNU Scientific Library Reference Manual (3rd Ed.). http://www.gnu.org/software/gsl/.

Gamow, G. (1946). Expanding universe and the origin of elements. *Phys.Rev.*, 70:572–573.

Giannantonio, T., Scranton, R., Crittenden, R. G., Nichol, R. C., Boughn, S. P., et al. (2008). Combined analysis of the integrated Sachs-Wolfe effect and cosmological implications. *Phys.Rev.*, D77:123520, 0801.4380.

Gordon, C. and Hu, W. (2004). A Low CMB quadrupole from dark energy isocurvature perturbations. *Phys.Rev.*, D70:083003, astro-ph/0406496.

Granett, B. R., Neyrinck, M. C., and Szapudi, I. (2008a). An Imprint of Super-Structures on the Microwave Background due to the Integrated Sachs-Wolfe Effect. *Astrophys.J.*, 683:L99–L102, 0805.3695.

Granett, B. R., Neyrinck, M. C., and Szapudi, I. (2008b). Dark Energy Detected with Supervoids and Superclusters. *ArXiv eprints 0805.2974*.

Gu, P., Wang, X., and Zhang, X. (2003). Dark energy and neutrino mass limits from baryogenesis. *Phys.Rev.*, D68:087301, hep-ph/0307148.

Guth, A. H. (1981). The Inflationary Universe: A Possible Solution to the Horizon and Flatness Problems. *Phys. Rev.*, D23:347–356.

Hannestad, S., Tu, H., and Wong, Y. Y. (2006). Measuring neutrino masses and dark energy with weak lensing tomography. *JCAP*, 6:25, astro-ph/0603019.

Heavens, A. (2003). 3d weak lensing. *MNRAS*, 343:1327, astro-ph/0304151.

Heavens, A., Refregier, A., and Heymans, C. (2000). Intrinsic Correlation of Galaxy Shapes: Implications for Weak Lensing Measurements. *MNRAS*, 319:649, astro-ph/0005269.

Heavens, A. F., Kitching, T. D., and Taylor, A. N. (2006). Measuring dark energy properties with 3D cosmic shear. *MNRAS*, 373:105–120, astro-ph/0606568.

Ho, S., Hirata, C., Padmanabhan, N., Seljak, U., and Bahcall, N. (2008). Correlation of CMB with large-scale structure: I. ISW Tomography and Cosmological Implications. *Phys.Rev.*, D78:043519, 0801.0642.

Hogg, D. W., Eisenstein, D. J., Blanton, M. R., Bahcall, N. A., Brinkmann, J., et al. (2005). Cosmic homogeneity demonstrated with luminous red galaxies. *Astrophys.J.*, 624:54–58, astro-ph/0411197.

Hollenstein, L., Sapone, D., Crittenden, R., and Schäfer, B. M. (2009). Constraints on early dark energy from CMB lensing and weak lensing tomography. *JCAP*, 4:12, 0902.1494.

Hu, W. (2002a). Dark energy and matter evolution from lensing tomography. *Phys. Rev. D*, 66(8):083515, astro-ph/0208093.

Hu, W. (2002b). Dark synergy: Gravitational lensing and the CMB. *Phys. Rev. D*, 65(2):023003, astro-ph/0108090.

Hu, W. and Scranton, R. (2004). Measuring dark energy clustering with CMB-galaxy correlations. *Phys.Rev.*, D70:123002, astro-ph/0408456.

Hu, W. and White, M. (2001). Power Spectra Estimation for Weak Lensing. *ApJ*, 554:67–73, astro-ph/0010352.

Hubble, E. (1929). A relation between distance and radial velocity among extra-galactic nebulae. *Proc.Nat.Acad.Sci.*, 15:168–173.

Huterer, D. (2002). Weak lensing and dark energy. *Phys. Rev. D*, 65(6):063001, astro-ph/0106399.

Huterer, D. (2010). Weak lensing, dark matter and dark energy. *General Relativity and Gravitation*, 42:2177–2195, 1001.1758.

Huterer, D., Takada, M., Bernstein, G., and Jain, B. (2006). Systematic errors in future weak-lensing surveys: requirements and prospects for self-calibration. *MNRAS*, 366:101–114, astro-ph/0506030.

Ichiki, K. and Keum, Y.-Y. (2008). Primordial Neutrinos, Cosmological Perturbations in Interacting Dark-Energy Model: CMB and LSS. *JCAP*, 0806:005, 0705.2134.

Jain, B. and Seljak, U. (1997). Cosmological Model Predictions for Weak Lensing: Linear and Nonlinear Regimes. *ApJ*, 484:560, astro-ph/9611077.

Jain, B. and Taylor, A. (2003). Cross-Correlation Tomography: Measuring Dark Energy Evolution with Weak Lensing. *Physical Review Letters*, 91(14):141302, astro-ph/0306046.

Kashlinsky, A., Atrio-Barandela, F., Kocevski, D., and Ebeling, H. (2009). A measurement of large-scale peculiar velocities of clusters of galaxies: results and cosmological implications. *Astrophys.J.*, 686:L49–L52, 0809.3734.

Kayser, B. (2003). Neutrino mass, mixing, and flavor change. In Altarelli, S. and Winter, K., editors, *Neutrino Mass*. Springer.

Khoury, J. and Wyman, M. (2009). N-Body Simulations of DGP and Degravitation Theories. *Phys.Rev.*, D80:064023, 0903.1292.

Kilbinger, M. et al. (2009). Dark-energy constraints and correlations with systematics from CFHTLS weak lensing, SNLS supernovae Ia and WMAP5. *A&A*, 497:677–688, 0810.5129.

Kitching, T. D., Heavens, A. F., and Miller, L. (2011). 3D photometric cosmic shear. *MNRAS*, 413:2923–2934, 1007.2953.

Kitching, T. D., Taylor, A. N., and Heavens, A. F. (2008). Systematic effects on dark energy from 3D weak shear. *MNRAS*, 389:173–190, 0801.3270.

Klypin, A., Holtzman, J., Primack, J., and Regos, E. (1993). Structure formation with cold plus hot dark matter. *Astrophys.J.*, 416:1–16, astro-ph/9305011.

Knox, L. (1995). Determination of inflationary observables by cosmic microwave background anisotropy experiments. *Phys. Rev.*, D52:4307–4318, astro-ph/9504054.

Komatsu, E. et al. (2011). Seven-Year Wilkinson Microwave Anisotropy Probe (WMAP) Observations: Cosmological Interpretation. *Astrophys.J.Suppl.*, 192:18, 1001.4538.

Kowalski, M. et al. (2008). Improved Cosmological Constraints from New, Old and Combined Supernova Datasets. *Astrophys. J.*, 686:749–778.

Kraus, C., Bornschein, B., Bornschein, L., Bonn, J., Flatt, B., et al. (2005). Final results from phase II of the Mainz neutrino mass search in tritium beta decay. *Eur.Phys.J.*, C40:447–468, hep-ex/0412056.

La Vacca, G. and Colombo, L. P. L. (2008). Gravitational Lensing Constraints on Dynamical and Coupled Dark Energy. *JCAP*, 0804:007, 0803.1640.

Lavaux, G., Tully, R. B., Mohayaee, R., and Colombi, S. (2010). Cosmic flow from 2MASS redshift survey: The origin of CMB dipole and implications for LCDM cosmology. *Astrophys.J.*, 709:483–498, 0810.3658.

Lemmon, T. J. and Mondragon, A. R. (2010). First-Order Special Relativistic Corrections to Kepler's Orbits. *ArXiv eprints 1012.5438*.

Lesgourgues, J. and Pastor, S. (2006). Massive neutrinos and cosmology. *Phys.Rept.*, 429:307–379, astro-ph/0603494.

Lewis, A., Challinor, A., and Lasenby, A. (2000). Efficient computation of CMB anisotropies in closed FRW models. *Astrophys. J.*, 538:473–476, astro-ph/9911177.

Li, B., Mota, D. F., and Barrow, J. D. (2011). N-body Simulations for Extended Quintessence Models. *Astrophys.J.*, 728:109, 1009.1400.

Li, H. and Xia, J.-Q. (2010). Constraints on Dark Energy Parameters from Correlations of CMB with LSS. *JCAP*, 1004:026, 1004.2774.

Linde, A. D. (1982). A New Inflationary Universe Scenario: A Possible Solution of the Horizon, Flatness, Homogeneity, Isotropy and Primordial Monopole Problems. *Phys.Lett.*, B108:389–393.

Linder, E. V. and Cahn, R. N. (2007). Parameterized Beyond-Einstein Growth. *Astropart.Phys.*, 28:481–488, astro-ph/0701317.

Lyth, D. H. and Liddle, A. R. (2009). *The Primordial Density Perturbation*. Cambridge University Press.

Ma, C.-P. and Bertschinger, E. (1995). Cosmological perturbation theory in the synchronous and conformal Newtonian gauges. *Astrophys. J.*, 455:7–25.

March, M. C., Trotta, R., Amendola, L., and Huterer, D. (2011). Robustness to systematics for future dark energy probes. *MNRAS*, page 612, 1101.1521.

Martin, J. (2012). Everything You Always Wanted To Know About The Cosmological Constant Problem (But Were Afraid To Ask). *Comptes Rendus Physique*, 13:566–665, 1205.3365.

Mather, J. C. et al. (1994). Measurement of the Cosmic Microwave Background spectrum by the COBE FIRAS instrument. *Astrophys. J.*, 420:439–444.

Mota, D. F., Pettorino, V., Robbers, G., and Wetterich, C. (2008). Neutrino clustering in growing neutrino quintessence. *Phys. Lett.*, B663:160–164.

Mukhanov, V. F., Feldman, H., and Brandenberger, R. H. (1992). Theory of cosmological perturbations. Part 1. Classical perturbations. Part 2. Quantum theory of perturbations. Part 3. Extensions. *Phys.Rept.*, 215:203–333.

Navarro, J. F., Frenk, C. S., and White, S. D. (1996). The Structure of cold dark matter halos. *Astrophys.J.*, 462:563–575, astro-ph/9508025.

Nojiri, S. and Odintsov, S. D. (2006). Introduction to modified gravity and gravitational alternative for dark energy. *eConf*, C0602061:06, hep-th/0601213.

Nunes, N. J., Schrempp, L., and Wetterich, C. (2011). Mass freezing in growing neutrino quintessence. *Phys.Rev.*, D83:083523, 1102.1664.

Osipowicz, A. et al. (2001). KATRIN: A Next generation tritium beta decay experiment with sub-eV sensitivity for the electron neutrino mass. Letter of intent. hep-ex/0109033.

Penzias, A. A. and Wilson, R. W. (1965). A Measurement of excess antenna temperature at 4080- Mc/s. *Astrophys. J.*, 142:419–421.

Percival, W. J. et al. (2001). The 2dF Galaxy Redshift Survey: The Power spectrum and the matter content of the Universe. *MNRAS*, 327:1297, astro-ph/0105252.

Perlmutter, S. et al. (1999). Measurements of Omega and Lambda from 42 High-Redshift Supernovae. *Astrophys. J.*, 517:565–586.

Perotto, L., Lesgourgues, J., Hannestad, S., Tu, H., and Wong, Y. Y. Y. (2006). Probing cosmological parameters with the CMB: Forecasts from full Monte Carlo simulations. *JCAP*, 0610:013, astro-ph/0606227.

Pettorino, V., Wintergerst, N., Amendola, L., and Wetterich, C. (2010). Neutrino lumps and the Cosmic Microwave Background. *Phys.Rev.*, D82:123001, 1009.2461.

Quinn, T. R., Katz, N., Stadel, J., and Lake, G. (1997). Time stepping N body simulations. *Astrophys.J.*, astro-ph/9710043.

Rasanen, S. (2004). Dark energy from backreaction. *JCAP*, 0402:003, astro-ph/0311257.

Ratra, B. and Peebles, P. J. E. (1988). Cosmological Consequences of a Rolling Homogeneous Scalar Field. *Phys. Rev.*, D37:3406.

Reid, B. A., Percival, W. J., Eisenstein, D. J., Verde, L., Spergel, D. N., et al. (2010). Cosmological Constraints from the Clustering of the Sloan Digital Sky Survey DR7 Luminous Red Galaxies. *MNRAS*, 404:60–85, 0907.1659.

Riess, A. G. et al. (1998). Observational Evidence from Supernovae for an Accelerating Universe and a Cosmological Constant. *Astron. J.*, 116:1009–1038.

Riess, A. G., Macri, L., Casertano, S., Sosey, M., Lampeitl, H., et al. (2009). A Redetermination of the Hubble Constant with the Hubble Space Telescope from a Differential Distance Ladder. *Astrophys.J.*, 699:539–563, 0905.0695.

Rodejohann, W. (2011). Neutrino-less Double Beta Decay and Particle Physics. *Int.J.Mod.Phys.*, E20:1833–1930, 1106.1334.

Sachs, R. K. and Wolfe, A. M. (1967). Perturbations of a cosmological model and angular variations of the microwave background. *Astrophys. J.*, 147:73–90.

Sapone, D. and Kunz, M. (2009). Fingerprinting dark energy. *Phys. Rev. D*, 80(8):083519, 0909.0007.

Sapone, D., Kunz, M., and Amendola, L. (2010). Fingerprinting dark energy. II. Weak lensing and galaxy clustering tests. *Phys. Rev. D*, 82(10):103535, 1007.2188.

Schäfer, B. M. (2009). Galactic Angular Momenta and Angular Momentum Correlations in the Cosmological Large-Scale Structure. *International Journal of Modern Physics D*, 18:173–222, 0808.0203.

Schäfer, B. M., Caldera-Cabral, G. A., and Maartens, R. (2008). Constraints on the decay of dark matter to dark energy from weak lensing bispectrum tomography. *ArXiv e-prints 0803.2154*.

Schrempp, L. and Brown, I. (2010). Do Bound Structures Brake Cosmic Acceleration? *JCAP*, 1005:023, 0912.3157.

Silk, J. (1968). Cosmic Black-Body Radiation and Galaxy Formation. *ApJ*, 151:459.

Skordis, C. and Albrecht, A. (2002). Planck scale quintessence and the physics of structure formation. *Phys.Rev.*, D66:043523, astro-ph/0012195.

Springel, V. (2005). The Cosmological simulation code GADGET-2. *MNRAS*, 364:1105–1134, astro-ph/0505010.

Springel, V., White, S. D., Jenkins, A., Frenk, C. S., Yoshida, N., et al. (2005). Simulating the joint evolution of quasars, galaxies and their large-scale distribution. *Nature*, 435:629–636, astro-ph/0504097.

Stabenau, H. F. and Jain, B. (2006). N-Body Simulations of Alternate Gravity Models. *Phys.Rev.*, D74:084007, astro-ph/0604038.

Steinhardt, P. J., Wang, L.-M., and Zlatev, I. (1999). Cosmological tracking solutions. *Phys.Rev.*, D59:123504, astro-ph/9812313.

Sullivan, M., Guy, J., Conley, A., Regnault, N., Astier, P., et al. (2011). SNLS3: Constraints on Dark Energy Combining the Supernova Legacy Survey Three Year Data with Other Probes. *Astrophys.J.*, 737:102, 1104.1444.

Takada, M. and Jain, B. (2004). Cosmological parameters from lensing power spectrum and bispectrum tomography. *MNRAS*, 348:897–915, astro-ph/0310125.

Takada, M. and Jain, B. (2009). The impact of non-Gaussian errors on weak lensing surveys. *MNRAS*, 395:2065–2086, 0810.4170.

Tegmark, M., Taylor, A. N., and Heavens, A. F. (1997). Karhunen-Loeve Eigenvalue Problems in Cosmology: How Should We Tackle Large Data Sets? *ApJ*, 480:22, astro-ph/9603021.

Tsujikawa, S. (2003). Introductory review of cosmic inflation. hep-ph/0304257.

Turner, M. S. and White, M. (1997). CDM models with a smooth component. *Phys. Rev. D*, 56:4439, astro-ph/9701138.

Vesely, F. J. (1994). *Computational Physics*. Plenum.

Watkins, R., Feldman, H. A., and Hudson, M. J. (2009). Consistently Large Cosmic Flows on Scales of 100 Mpc/h: a Challenge for the Standard LCDM Cosmology. *MNRAS*, 392:743–756, 0809.4041.

Weinberg, S. (2008). *Cosmology*. Oxford University Press.

Wetterich, C. (1988). Cosmology and the Fate of Dilatation Symmetry. *Nucl. Phys.*, B302:668.

Wetterich, C. (1995). The Cosmon model for an asymptotically vanishing time dependent cosmological 'constant'. *Astron.Astrophys.*, 301:321–328, hep-th/9408025.

Wetterich, C. (2003). Can structure formation influence the cosmological evolution? *Phys.Rev.*, D67:043513, astro-ph/0111166.

Wetterich, C. (2007). Growing neutrinos and cosmological selection. *Phys.Lett.*, B655:201–208, 0706.4427.

Wetterich, C. (2008). Naturalness of exponential cosmon potentials and the cosmological constant problem. *Phys.Rev.*, D77:103505, 0801.3208.

Wintergerst, N., Pettorino, V., Mota, D., and Wetterich, C. (2010). Very large scale structures in growing neutrino quintessence. *Phys.Rev.*, D81:063525, 0910.4985.

Zhao, G.-B., Li, B., and Koyama, K. (2011). N-body Simulations for f(R) Gravity using a Self-adaptive Particle-Mesh Code. *Phys.Rev.*, D83:044007, 1011.1257.

Zlatev, I., Wang, L.-M., and Steinhardt, P. J. (1999). Quintessence, cosmic coincidence, and the cosmological constant. *Phys.Rev.Lett.*, 82:896–899, astro-ph/9807002.